

ESTIMATION OF COSEISMIC DISPLACEMENT FROM
ACCELEROMETER AND GNSS RECORDS

by

MOYA HUALLPA, Luis Angel

A dissertation submitted in partial fulfillment of the
requirements for the degree of
Doctor of Philosophy

Chiba University

July 2016

(千葉大学審査学位論文)

ESTIMATION OF COSEISMIC DISPLACEMENT FROM
ACCELEROMETER AND GNSS RECORDS

by

MOYA HUALLPA, Luis Angel

A dissertation submitted in partial fulfillment of the
requirements for the degree of
Doctor of Philosophy

Chiba University

July 2016

Table of Contents

ACKNOWLEDGEMENTS	i
VITA	ii
PUBLICATIONS	iii
ABSTRACT OF THE DISSERTATION	iv
1 Introduction	1
1.1 Overview	1
1.2 Scope and objectives	2
1.3 Outline of this research	2
2 State of the art and theoretical concepts	5
2.1 Digital strong motion accelerometers in Japan	5
2.1.1 K-NET (Kyoshin NETwork)	5
2.1.3 Shift of the baseline and its effects	5
2.1.4 Baseline correction methods	7
2.2 Continuous GNSS monitoring	8
2.2.1 GEONET	8
2.2.2 Real Time Kinematic Relative positioning	9
2.2.3 Kinematic Precise Point Positioning	11
3 Fukushima nuclear power plant's strong motion network	12
3.1 Effects of the baseline shift in the ground velocity and ground displacement	14
3.1.1 Velocity trend estimation using polynomials	16
3.1.2 Velocity trend estimation using linear segments	17
3.1.3 Effect of the baseline correction on the displacement time history	18
3.2 Effects of the permanent displacement in the response spectra	22
3.3 Concluding remarks	25
4 Comparison of coseismic displacement from GNSS and accelerometers	26
4.1 Spatial distribution of coseismic displacement from GEONET	26
4.1.1 Kriging method	26
4.1.2 Coseismic displacement from GEONET	29
4.2 Coseismic displacement from strong ground motion	29
4.2.1 Comparison of coseismic displacement from strong ground motion and GEONET	32
4.3 Concluding remarks	34
5 Proposed method of baseline correction for KiK-net	35
5.1 Hypothesis	35

5.2 Previous definitions.....	35
5.3 Validation and analysis	37
5.4 Concluding remarks	44
6 Assessment of GNSS Kinematic relative positioning for long baseline distance	45
6.1 Problem statement.....	45
6.2 Case study: Nagano earthquake	45
6.3 Evaluation of accuracy of permanent ground displacement	46
6.4 Concluding remarks	52
7 Coseismic displacement in the 2016 Kumamoto earthquake from LIDAR data	53
7.1 Introduction.....	53
7.2 Study area and data description.....	53
7.3 Methodology	56
7.4 Results.....	57
7.5 Validation of results	60
7.6 Conclusions.....	61
7.7 Data and Resources	61
8 General conclusions	62
References	64
APPENDICES	68

ACKNOWLEDGEMENTS

I would like to thank my advisor, Professor Fumio Yamazaki, for supporting me and sharing his great knowledge in Earthquake engineering, Engineering seismology, and Remote Sensing, which has broadened my vision about the different disciplines related to earthquakes. Under his guiding, these three years have been my best experience in the research community. I also thank Dr. Wen Liu for her comments on various drafts and her help when it was necessary.

It is appropriate to say a word of thanks to all members of Yamazaki Laboratory. Mariko Naruke, for all her help and assistant in all my stay in Japan. Homa Zakeri deserves an extra credit for encouraging me every day and make me feel like I was at home. Pisut Nakmuenwai, special thanks for guiding me through the jungle of computation and programming. Omid Hashemiparast for his friendship in these years. My sincere gratitude to Ms. Konomi for being a good friend and having patient when teaching me Japanese.

Thanks to the Japan Science and Technology (JST) and the Japanese government program Science and Technology Research Partnership for Sustainable Development (SATREPS) for the support by the Monbukagakusho scholarship.

Last but not least, I would like to thank my family, Juan, Eulalia, Juanjo, Pamela, and Roy for all their support and encouragement in every day. They are the inspiration for everything in my life.

VITA

April 26, 1985 Born, Province of Lima, Lima City, Peru

Education Period

2003-2009 Undergraduate student, Faculty of Civil Engineering, National University of Engineering, Lima, Peru

2011-2013 Master of Science, Faculty of Civil Engineering, National University of Engineering, Lima, Peru

2013-2016 Doctoral student, Department of Urban Environmental Systems, Graduate School of Engineering, Chiba University, Chiba, Japan

Employment

2009-2013 Research Assistant, Japan-Peru Center for Earthquake Engineering Research and Disaster Mitigation, National University of Engineering, Lima, Peru

2012-2013 Assistant Professor, Faculty of Civil Engineering, National University of Engineering, Lima, Peru

PUBLICATIONS

- Moya, L., Yamazaki, F., and Liu, W. (2016) Comparison of coseismic displacement obtained from GEONET and seismic networks. *Journal of Earthquake and Tsunami*. Vol. 10, No 2, 18 pages.
- Moya, L., Yamazaki, F., and Liu, W. (2016) Baseline effect on the estimation of crustal displacement using GPS kinematic differential correction. *16th World Conference of Earthquake Engineering*. (In review).
- Moya, L., Yamazaki, F., and Liu, W. (2014) Comparison of coseismic displacement obtained from GEONET and seismic networks. *The 14th Japan Earthquake Engineering Symposium*, 624-632.
- Moya, L., Yamazaki, F., and Liu, W. (2014) Estimation of geodetic displacement in the 2011 Tohoku Earthquake from accelerograms and GPS data. *The 5th Asia conference on earthquake engineering*, 8 pages.
- Yamazaki, F., Moya, L., Anekoji, K., and Liu, W. (2014) Comparison of coseismic displacements obtained from strong motion accelerograms and GPS data in Japan. *Second European Conference on Earthquake Engineering and Seismology*, 8 pages.
- Saito, T., Moya, L., Fajardo, C., and Morita, K. (2013) Experimental study on dynamic behavior of unreinforced masonry walls. *JDR*, Vol. 8, No. 2, 305-311.

ABSTRACT OF THE DISSERTATION**ESTIMATION OF COSEISMIC DISPLACEMENT FROM
ACCELEROMETERS AND GNSS RECORDS**

by

Moya Huallpa, Luis Angel

Doctor of Engineering

Chiba University, 2016

Japan is one of the countries with the fastest growing development in ground motion sensors and GNSS networks. This thesis evaluates the accuracy of permanent ground displacement estimated from acceleration records and GNSS station. For this purpose, we use large amount of data from the public networks: K-NET, KiK-net (strong motion networks) and GEONET (GNSS network) and from the strong motion network of the Fukushima Daiichi Nuclear Power Plant. We found that the permanent ground displacement estimated from the strong motion network of Fukushima nuclear power has a large variation. Large standard deviation was also observed from accelerometers located at the surface from K-NET and KiK-net. On the other hand, accelerometers located at boreholes showed the best accuracy. Besides, a baseline correction method for KiK-net stations is proposed, which showed improvements for the accelerometers located at surface. The thesis also analyzes the performance of the kinematic relative positioning technique for long distances between the base and the rover GEONET stations. Furthermore, the coseismic displacement produced during the 2016 Kumamoto earthquake was estimated using Lidar data and compared with the result from acceleration records.

Chapter 1

Introduction

1.1 Overview

The estimation of permanent ground displacement produced by earthquakes is very important for earthquake engineering and seismology. Such an estimation is based on three main technologies: Seismometers, Global Navigation Satellite System (GNSS), and Synthetic Aperture Radar (SAR) satellite images. These technologies are available in Japan, two nationwide network of strong ground motion and one of GNSS. Besides, the Japan Aerospace Exploration Agency (JAXA) counts with earth observation satellites. The present thesis focus on the two first: strong ground motion networks and GNSS network.

Velocity and displacement records are of great importance in earthquake engineering and seismology. In a standard processing technique, the raw record is low-cut filtered in order to remove the effects of baseline shifts. However, if permanent ground displacement occurred, low-cut filtering will remove it as well. Permanent ground displacement mostly occurs in near-fault areas, which is characterized by having long period pulses in their ground velocities. Several studies have been performed to analysis the effects of near-source ground motion on long-period buildings (Hall et al., 1995; Mavroeidis and Papageorgiou, 2004; Liao et al., 2004; Ozbulut and Hurlebaus, 2012). However, the pulse generated by the permanent ground displacement was not considered.

Tsunami early warning systems is a challenging problem. There are a number of studies currently in the field of seismology that are using new approaches to estimate source models. From an inversion procedure, coseismic displacement can be used alone to approximate the fault model (Ohta et al., 2012) or combined with strong-motion and coastal and offshore wave gauges for a better estimation (Melgar and Bock, 2013, Melgar et al., 2013). Then, with the tsunami Green's functions calculated, the tsunami waveforms can be computed. For this task, coseismic displacement is mostly calculated from GNSS and Interferometric Synthetic Aperture Radar (InSAR) because of their guaranteed level of accuracy. However, traditional GNSS processing and InSAR cannot be used for early warning purpose because the long time required in the data acquisition. But, it is worth to mention that efforts to use high-rate continuous GPS for real and/or near-real time processing is currently doing (Ohta et al., 2012; Branzanti et al., 2013; Colosimo et al., 2011; Liu et al., 2014; Niu and Xu, 2014). Another big issue is that GNSS stations are sparse around the world, being Japan the only country that have a very dense GNSS network; whereas, strong-motion is almost ubiquitous in earthquake prone areas, mostly because this technology was developed several years before, being the first strong-motion recorded on March 10, 1933 during the Long Beach, California earthquake.

From GNSS, two methods to calculate displacement with high precision: Kinematic Precise Point Positioning (KPPP) and Real-Time Kinematic (RTK) positioning are commonly used to estimate coseismic displacement. The KPPP has become more popular in recent years because it requires only one GNSS

station; however, additional information, such as precise ephemerides and clock correction, provided by the International GNSS Service (IGS), is required. On the other hand, RTK requires two GNSS stations, but achieves the best accuracy level under certain conditions.

1.2 Scope and objectives

Based on the facts depicted in the previous section, it is important to evaluate how much accuracy is the ground displacement obtained either from the acceleration record or GNSS data. Japan is a country that has two advantages to our research purpose: is a region with high seismic activity and is a country with the biggest accelerometers and GNSS networks with stations spread all around the country. Giving therefore, a great opportunity to have a closer look on the ground displacement estimation from different sources.

The main scope of this research is to analyze the accuracy of the ground displacement obtained from accelerometers and GNSS stations. The specific objectives are outlined as follows:

- Evaluate the two vertical arrays from the Fukushima nuclear power plant to calculate the precision and accuracy of the ground displacement from acceleration records.
- Compare the displacement obtained from a large amount of acceleration record that belongs to K-NET and KiK-net during the M_w 9.0 Tohoku earthquake with a more accurate estimation obtained from GEONET.
- Develop a method to obtain a good estimation of ground displacement from KiK-net stations.
- Evaluate the effect of the permanent ground displacement on long-period structures.
- Analyze the performance of the kinematic relative positioning technique for long distance between the station where the displacement is desired and the base station, which have to be stationary with a well-known position.
- Calculate the coseismic displacement during the mainshock of the 2016 Kumamoto earthquake and compare it with the coseismic displacement from acceleration records.

1.3 Outline of this research

The purpose of this thesis is to analyze the strength and weakness of the ground displacement estimated from strong motion acceleration and GNSS stations. This is done in the subsequent chapters by first providing an introduction to the problems we are about to face. The book is split into four distinct parts: the first part, chapter 2, deals with the basic concepts and the state of the art needed to follow up next chapters; while the second part, chapters 3, 4 and 5, present the studies on ground displacement obtained from accelerometers. The third part, chapter 6, covers a study on the accuracy of the estimation of permanent ground displacement from the kinematic relative positioning technique. The fourth part deals with the use of Lidar data set to calculate the coseismic displacement and contrast its results with the coseismic displacement from acceleration records. The thesis contents are outlined in more detail as follows:

Chapter 2: This chapter presents and describe details of the three nationwide networks in Japan: K-NET, KiK-net and GEONET. K-NET and KiK-net are consist of strong ground motion accelerometers. The chapter also outlines the difficulties presented when a estimation of the ground displacement is intended from acceleration records. GEONET consists of GNSS stations and here we show the two methods to calculate ground displacement: relative positioning and precise point positioning.

Chapter 3: This chapter analyzes strong ground motion stations located in the same area and arranged in two vertical arrays. It gives the opportunity to obtain different estimations of the permanent ground displacement and observe the precision and accuracy. Besides, in order to observe if the permanent ground displacement affects the dynamic behavior of long-period structures we calculate the response spectra.

Chapter 4: In this chapter, in order to evaluate the accuracy of the permanent displacement obtained from a large amount of accelerometers, we interpolated the displacements calculated from GNSS records to estimate the permanent ground displacement at 508 strong ground motion stations. This chapter evaluates the uncertainties in the permanent ground displacement obtained using two different baseline correction methods.

Chapter 5: A new method to estimate permanent ground displacement from the KiK-net stations are presented in this chapter. Each KiK-net station has two accelerometers that can be used together to obtain a better estimation of the ground displacement. We compare the method with previous method and with displacement obtained from GNSS.

Chapter 6: This chapter analyzes the accuracy of the permanent ground displacement obtained from GNSS when the kinematic relative positioning is used. Kinematic relative positioning is useful for a fast estimation of displacement, which is important for early warning systems. However, it requires two GNSS stations: a station where an estimation of displacement is to be determined and a station that remains stationary with a well-known position. The performance of relative positioning depends on the distance between the receiver and the base stations, often referred to as the baseline. In this study, we evaluate this tradeoff by calculating the permanent displacement in the Geonet station 0266 during the November 22, 2014 M_w 6.2 Nagano earthquake several times with different base station each time. Then, variations in the permanent displacement are evaluated in terms of the baseline. With several available GEONET stations to set as the base station, we study the relationship between the performance of displacement and the baseline.

Chapter 7: A very unusual pair of Lidar data obtained before and after the 2016 Kumamoto earthquake is used to calculate the spatial distribution of coseismic displacement. For this purpose, a window matching search approach based on the correlation coefficient between the pair Lidar data was employed. The results shows good agreement with the coseismic displacement obtained from acceleration records. Besides, the results delineates the Futugawa fault line which are consistent with the one published by the Geological Survey Institute of Japan.

The general conclusions are drawn in the final chapter, which provides discussions obtained in this research.

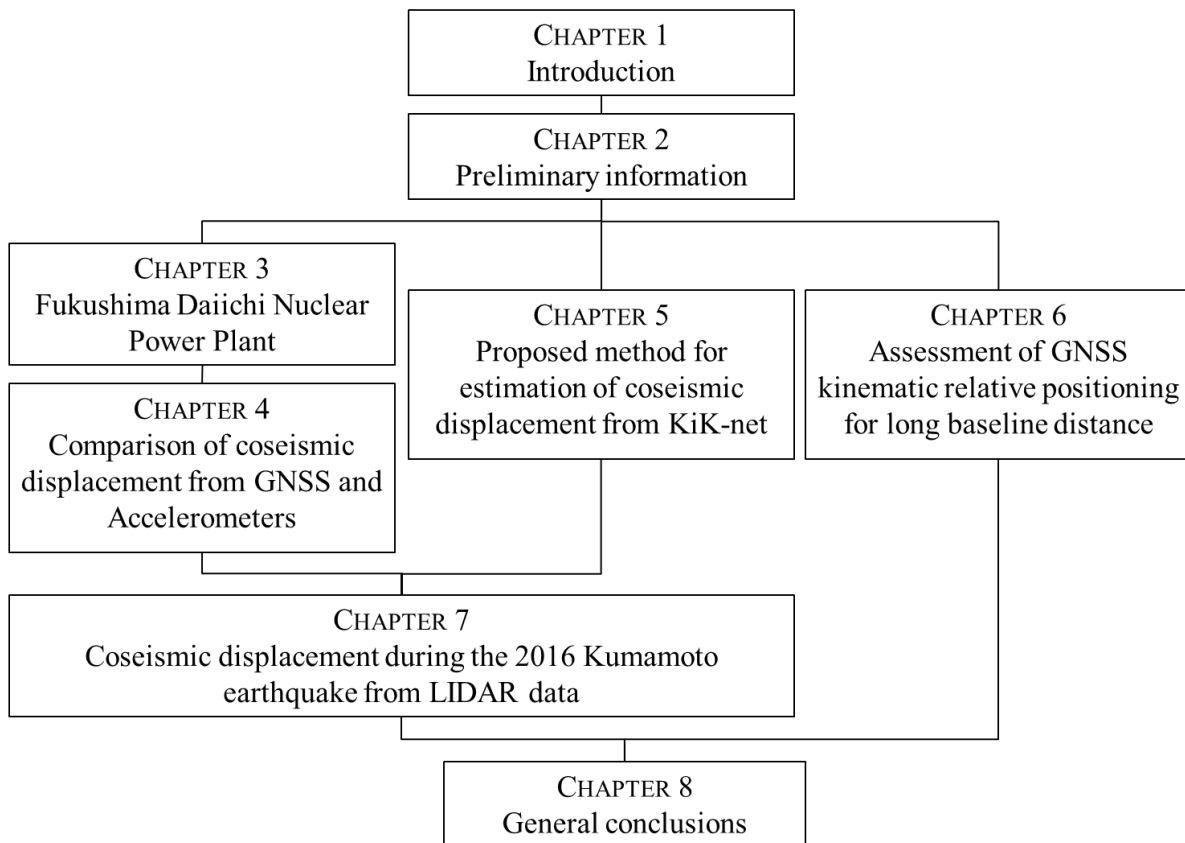


Figure 1.1 Flowchart of the thesis

Chapter 2

State of the art and theoretical concepts

2.1 Digital strong motion accelerometers in Japan

The construction of national strong motion networks was encouraged after the 1995 Hyogoken-Nanbu earthquake. Since 1996, The National Research Institute for Earth Science and Disaster Prevention (NIED) is in charge of the two nationwide strong motion network, K-NET and KiK-net (see Figure 2.1). Up to now, thousands of events have been recorded and provided to the public by its web-site (<http://www.kyoshin.bosai.go.jp/>).

2.1.1 K-NET (Kyoshin NETWORK)

The construction started one year after the Hyogoken-Nanbu earthquake. The K-NET consists of more than 1,000 stations installed on the ground surface which covers Japan's territory uniformly, and the stations are located mostly in public offices, schools, and parks.

The specifications of the accelerometers are depicted in detail in the publication of Aoi et al. (2004), which are as follow: The sensor used is a tri-axial force-balance accelerometer with a natural frequency of 450 Hz and a damping factor of 0.707. The sensor gain is 3 V/g. The model of the data logger is SMAC-MDK, which have a 24-bit A/D converter and maximum measurable acceleration of 2000 gals. The sampling rate is 100 Hz.

2.1.2 KiK-net (Kiban Kyoshin network)

This network was established under the plan “Fundamental Survey for Earthquake Research Promotion” which was directed by “The Headquarters for Earthquake Research Promotion”. This plan also executed the construction of other networks such as the high sensitivity seismic network “Hi-net” and the broadband seismic observation network “F-net”. The KiK-net consists of approximately 700 stations, each of which is equipped with two accelerometers: one on the ground surface, and the other in the borehole at the bedrock level. K-NET stations are located in habited (urban to suburban) areas, whereas KiK-net stations are laid on stiff-soil or rock sites, which are generally less populated.

The sensor used is a tri-axial force-balance accelerometer with a natural frequency of 450 Hz and a damping factor of 0.707. The sensor gain is 3 V/g. The model of the data logger is K-NET95, which have a 24-bit A/D converter and maximum measurable acceleration of 2000 gals. The sampling rate is 100 Hz (Aoi et al. 2004).

2.1.3 Shift of the baseline and its effects

A direct single and double integration of the acceleration records by a numerical procedure, such as the linear acceleration method:

$$\dot{x}_{i+1} = \dot{x}_i + \frac{\Delta t}{2}(\ddot{x}_i + \ddot{x}_{i+1}) \quad (2.1a)$$

$$x_{i+1} = x_i + \dot{x}_i \Delta t + \frac{\Delta t^2}{6}(2\ddot{x}_i + \ddot{x}_{i+1}) \quad (2.1b)$$

where x_i , \dot{x}_i , \ddot{x}_i denote the displacement, velocity, acceleration at a time instant i , respectively, and Δt is the time interval. In most cases, the application of Equation (2.1) produces an overestimated displacement (Figure 2.2c). The main reason of this effect is due to a slight shift of the baseline in the acceleration record, whose amplitude varies with time. Although this baseline shift cannot be appreciated in the acceleration record (Figure 2.2a), it affects the velocity and displacement waveforms (Figure 2.2b and 2.2c).

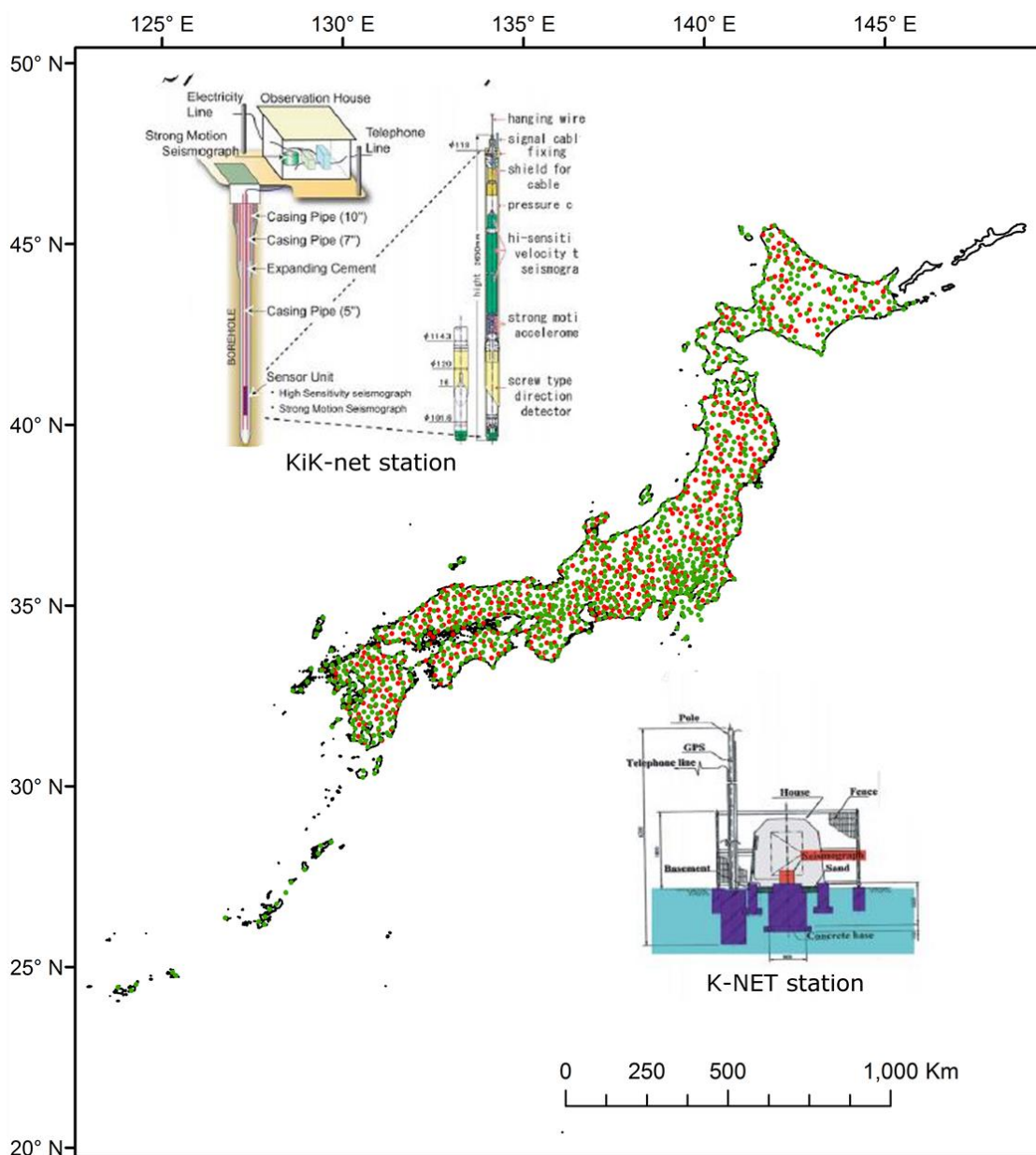


Figure 2.1 Location of KiK-net (red dots) and K-NET stations (green dots). The insets show a scheme of the facilities for both networks modified from Aoi et al. (2004).

2.1.4 Baseline correction methods

Basically, there are two procedures to reduce the effect of the baseline shift. One of them is a low-cut filter method, in which the low frequency components are reduced or eliminated from the record. This is a robust method because the baseline shift has mainly low frequency components. Thus, low-cut filter is used as a standard method in the field of earthquake engineering. However, low-cut filter cannot be used to calculate the permanent ground displacement. The other procedure relies on estimating the trend observed in the ground velocity record using polynomials or linear segments (Figure 2.2b). Then, after removing the trend from the ground velocity (Figure 2.2d) the ground displacement can be calculated (Figure 2.2e). More detail related to these baseline correction method is provided in chapter 4.

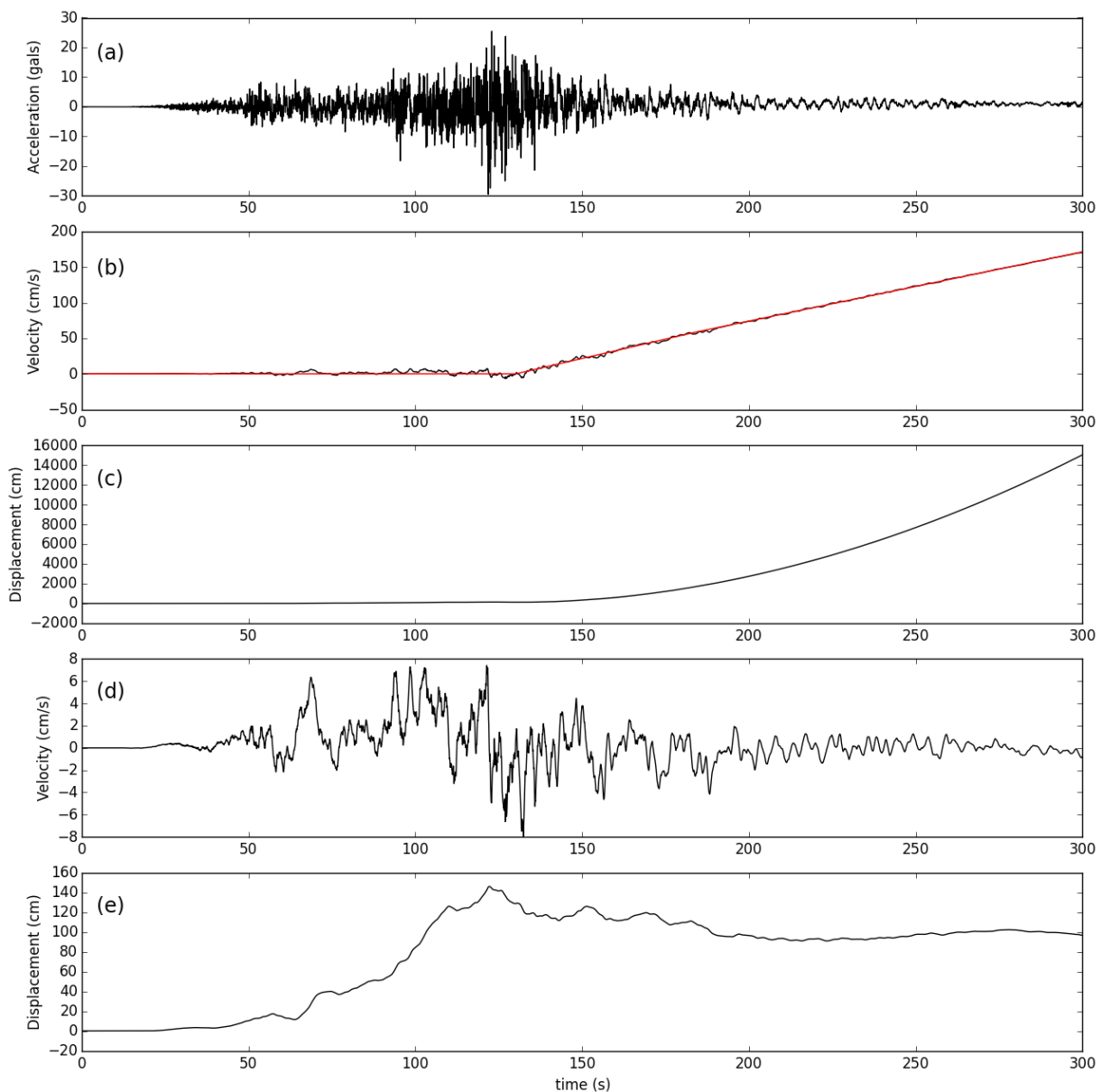


Figure 2.2 Baseline correction. (a) acceleration record; (b) uncorrected velocity; (c) uncorrected displacement; (d) linear trend ; (e) corrected velocity; (f) corrected displacement.

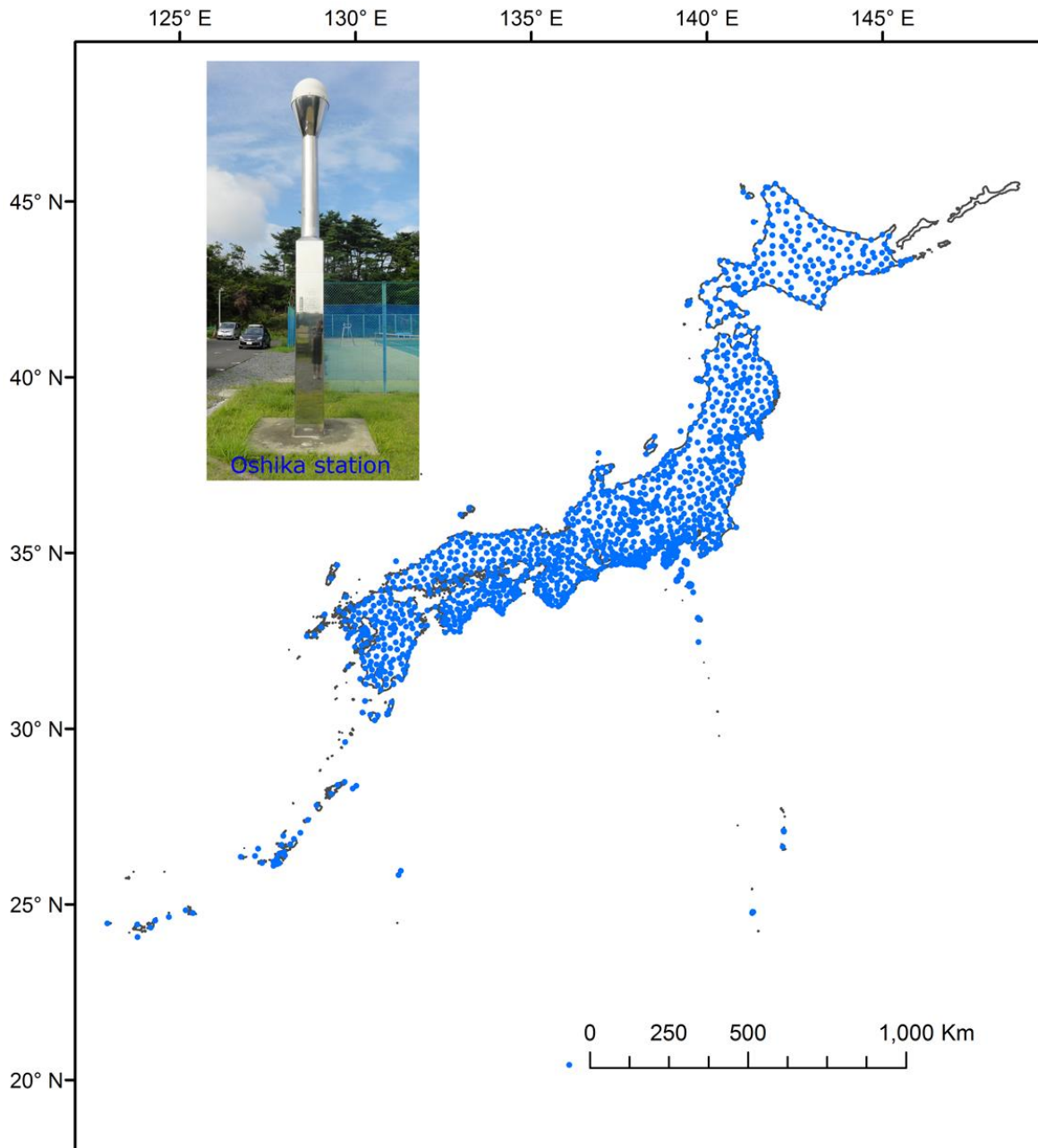


Figure 2.3 Location of GEONET stations (inset shows a picture of oshika GEONET station)

2.2 Continuous GNSS monitoring

2.2.1 GEONET

The GNSS Earth Observation Network System (GEONET) of Japan began in 1996 with the join of the two GPS network systems: the Continuous Strain Monitoring System with GPS (COSMOS-G2) and the GPS Regional Array for Precise Surveying/Physical Earth Science (GRAPES) and an additional 400 station. Later on, in 2002 GEONET stations became usable for public surveys and later in 2003 the Geospatial Information Authority of Japan (GSI), the institution in charge of GEONET, upgraded the GEONET system and added real-time capability.

Currently, GEONET consists of 1,300 stations located at intervals of approximately 20 km (Sagiya, 2004; Yamagiwa et al. 2006) as depicted in Figure 2.3. Only one antenna type, the choke ring antenna of Dorne Margolin T-type, is used in order to avoid multipath and different antenna phase center variations. Besides, the receivers are capable of 1-Hz sampling and real-time data transfer in a uniform format (RINEX - Receiver Independent Exchange Format). All the stations operate 24 hours a day and record the signal of the USA GPS, the Russian GLONASS and the Japanese QZSS. GEONET provides RINEX data with 30 second intervals through the internet and high-sampling rate data with 1 Hz sampling through a private distributor.

GEONET uses the data with 30-second sampling to perform three kinds of routine analysis: Quick, rapid and final analysis. Quick analysis is carried out every 3 hours using 6-hour data window and ultra-rapid products from the IGS, Rapid analysis is carried out every day with 24 hours of data and using ultra-rapid products as well. Final analysis is carried out every week but with two weeks of delay in order to use the IGS final products. An additional analysis is carried out in an emergency situation. Using 1 Hz real-time data, RTK analysis is performed.

The GEONET network is used to monitor long-term crustal movements, detect coseismic displacements, and detect volcanic activities. Besides, GEONET data have been used in other research areas such as geodesy, ionospheric research and so on.

2.2.2 Real Time Kinematic Relative positioning

Real Time Kinematic (RTK) aims to calculate, for each epoch, the vector between an unknown station (rover station) with respect to a station with well-known coordinates that must remain constant in time (master station). In other words, the relative position of the rover station with respect of the master station as a function of time. The vector between the two stations is known as the baseline (BL) vector. The method requires receivers that output the P code and carrier-phase observations on both frequencies L1 (1575.42 Hz) and L2 (1227.60 Hz). The P code is a sequence of approximately $2.35 \cdot 10^{14}$ chips (each chip represents a bit) with a chipping rate of 10.23 MHz, and is used to calculate the pseudorange. The carrier-phase is a measure of the carrier wave itself. The carrier phase and pseudorange equations for the master (point A) and the rover (point B) for a given satellite j with a frequency f are:

$$\begin{aligned}
 \Phi_A^j(t) + f^j \delta^j(t) &= \frac{1}{\lambda} \rho_A^j(t) - \frac{1}{\lambda} I_A^j(t) + \frac{1}{\lambda} T_A^j(t) + N_A^j + f^j \delta_A(t) + \varepsilon_\Phi \\
 \Phi_B^j(t) + f^j \delta^j(t) &= \frac{1}{\lambda} \rho_B^j(t) - \frac{1}{\lambda} I_B^j(t) + \frac{1}{\lambda} T_B^j(t) + N_B^j + f^j \delta_B(t) + \varepsilon_\Phi \\
 P_A^j(t) + c\delta^j(t) &= \rho_A^j(t) + I_A^j(t) + T_A^j(t) + c\delta_A(t) + \varepsilon_P \\
 P_B^j(t) + c\delta^j(t) &= \rho_B^j(t) + I_B^j(t) + T_B^j(t) + c\delta_B(t) + \varepsilon_P
 \end{aligned} \tag{2.2}$$

where $\Phi_i^j(t)$ is the measured carrier phase expressed in cycles (see Figure 2.4), $P_i^j(t)$ is the pseudorange, λ is the wavelength, f^j is a signal frequency of the satellite j , c is the velocity of light, $\rho_i^j(t)$ is the geometric distance between the satellite j and the observed point i , $\delta^j(t)$ is the bias of the satellite clock j , $\delta_i(t)$ is the

clock bias of the receiver at point i , $I_i^j(t)$ and $T_i^j(t)$ is the ionosphere and troposphere delay between the satellite j and the observed point i , and ε_Φ is the measurement error of carrier-phase. For shorth BL length (|BL|), the double differences of Eq. (2.2) are:

$$\begin{aligned}\Phi_{AB}^{jk}(t) &= \frac{1}{\lambda} \rho_{AB}^{jk}(t) + N_{AB}^{jk} + \varepsilon_\Phi \\ P_{AB}^{jk}(t) &= \rho_{AB}^{jk}(t) + \varepsilon_P\end{aligned}\quad (2.3)$$

Which follows the symbolic convention:

$$\begin{aligned}{}^*_{AB}{}^j &= {}^*_B{}^j - {}^*_A{}^j \\ {}^*_{AB}{}^{jk} &= {}^*_A{}^k - {}^*_A{}^j\end{aligned}\quad (2.4)$$

When the |BL| is short, the ionosphere (I_i^j) and troposphere (T_i^j) delay are canceled in equation (2.3) because they are assumed to be equal for both the master and the rover station. A centimeter accuracy level is achieved when the |BL| is less than approximately 10-20 km (Hofmann-Wellenhof et al., 2001; Borre and Strang, 2012, Takasu and Yasuda, 2010). Nevertheless, the permanent displacement required for EWS must be calculated under different conditions. A short |BL| is not useful because coseismic deformation is widely spread; therefore, permanent displacements would develop for both the master and rover stations when the |BL| is less than 20 km. Therefore, the RTK technique with a long |BL| is required. For a long |BL|, the atmospheric effects must be considered in the double-differencing equation (2.3).

$$\begin{aligned}\Phi_{AB}^{jk}(t) &= \frac{1}{\lambda} \rho_{AB}^{jk}(t) - \frac{1}{\lambda} I_{AB}^{jk}(t) + \frac{1}{\lambda} T_{AB}^{jk}(t) + N_{AB}^{jk} + \varepsilon_\Phi \\ P_{AB}^{jk}(t) &= \rho_{AB}^{jk}(t) + I_{AB}^{jk}(t) + T_{AB}^{jk}(t) + \varepsilon_P\end{aligned}\quad (2.5)$$

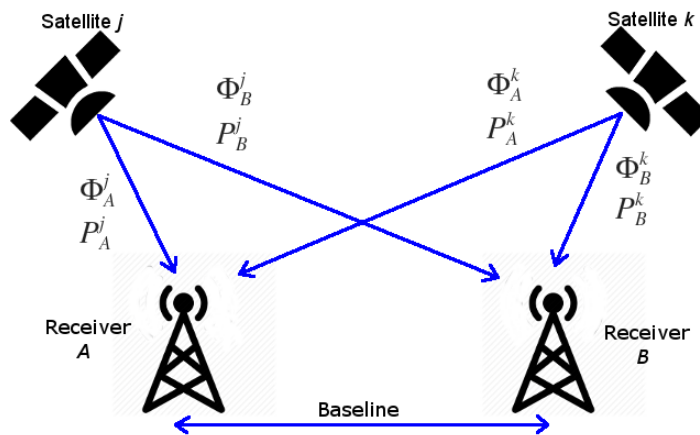


Figure 2.4 Principle of relative positioning

Because the assumption that ionosphere and troposphere delay are equal for both master and rover station is no longer acceptable, these terms must be estimated. Equations (2.3) and (2.5) represent the relation between two receivers and two satellite's signals. Furthermore, RTK method requires at least four satellites to set up an equations system necessary to calculate the coordinates of the receiver. Several models have been proposed for I_i^j and T_i^j , such as dual-frequency measurements to eliminate the ionosphere delay, and the Saastamoinen model for the tropospheric delay. Another strategy to solve equation (2.5) is to consider I_i^j and T_i^j as additional unknowns by a non-linear combination (Takasu and Yasuda, 2010).

2.2.3 Kinematic Precise Point Positioning

The Precise Point Positioning (PPP) was proposed by Zumberge et al. (1997) with the purpose of processing Networks composed of a large amount of GPS receivers. The main idea is to process one station independently with the same level of accuracy than a simultaneous processing of the network. Simultaneous analysis of R receivers associated to the least squares method is proportional to R^3 . With this purpose, Zumberge et al. (1997) pointed out that if R receivers are used to improve the global parameters such as the orbits of the GPS satellites and the satellite clocks, then others GPS stations are able to use those parameters one at a time.

Because the method proves to be efficient and robust, currently most commercial softwares provides PPP analysis. Besides, the International GNSS service (IGS) calculated those global parameters improved and provide to the public for free. However, the final products are made available with a delay up to 13 to 20 days. Applications of this method can be found in chapter 5, where we used the kinematic version (KPPP).

Chapter 3

Fukushima nuclear power plant's strong motion network

The Fukushima Daiichi Nuclear Power Plant is located at $141^{\circ}02'00''\text{E}$ and $37^{\circ}25'00''\text{N}$ and counts with ten accelerometers placed in two boreholes, GN and GS, as shown in Figure 3.1. The accelerometers of borehole GS the accelerometers are placed at levels +32.9, -5, -100, -200 and -300 meters, and the accelerometers of borehole GN are located at +12.2, -5, -100, -200 and -300 meters. Figure 3.1c depicts the soil profile of each borehole. The accelerometers have 24-bit A/D converter with a measurable range of $\pm 2g$ and sampling frequency of 100 Hz. The frequency range over which the sensor provides a linear response is from 0.05 to 30 Hz.

The GN and GS arrays recorded the strong-motion of the Mw 9.0 Tohoku earthquake, which epicenter was located at approximately 178 km northeast of the Nuclear Power Plant. This rich dataset provides an extensive information of the strong-motion at different deeps. Acceleration waveforms of GN and GS are depicted in Figure 3.2, where the average of the first 10 seconds of the pre-event was removed from the original record. Removing the average of a segment of the pre-event is a common practice (Boore, 2011) and thus the record is still considered as raw data.

Around 12 km to the north from the Fukushima Daiichi Nuclear Power Plant, the Odaka station (code 0203) of the GNSS Earth Observation Network System (GEONET) is located (See Figure 3.1a). The GEONET network, which is operated by the Geospatial Information Authority of Japan (GSI), provides raw data at 30 second and 1 Hz sampling. Unfortunately, there was a malfunction at the GEONET 0203 station during the earthquake. Thus, only the first half part of the main shock was recorded. However, soon after, the station was repaired and daily coordinates of subsequent days are available. The permanent ground displacement at Odaka station calculated from the daily coordinates are 259.2 cm eastward, 37.1 cm southward, and 53.7 cm downward.

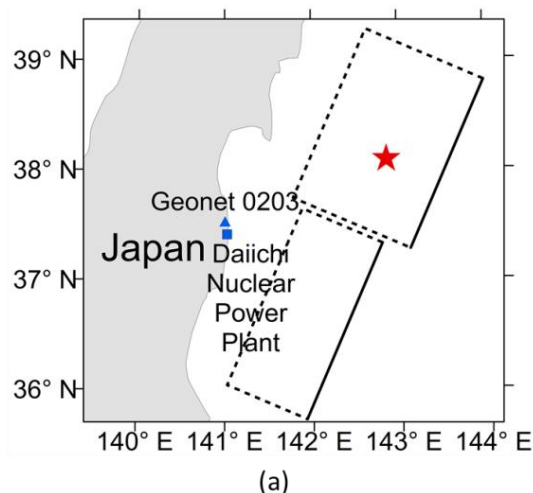


Figure 3.1 (a) Location of accelerometers, GNSS station, source model and epicenter of the march 11, 2011 M_w 9.0 Tohoku earthquake

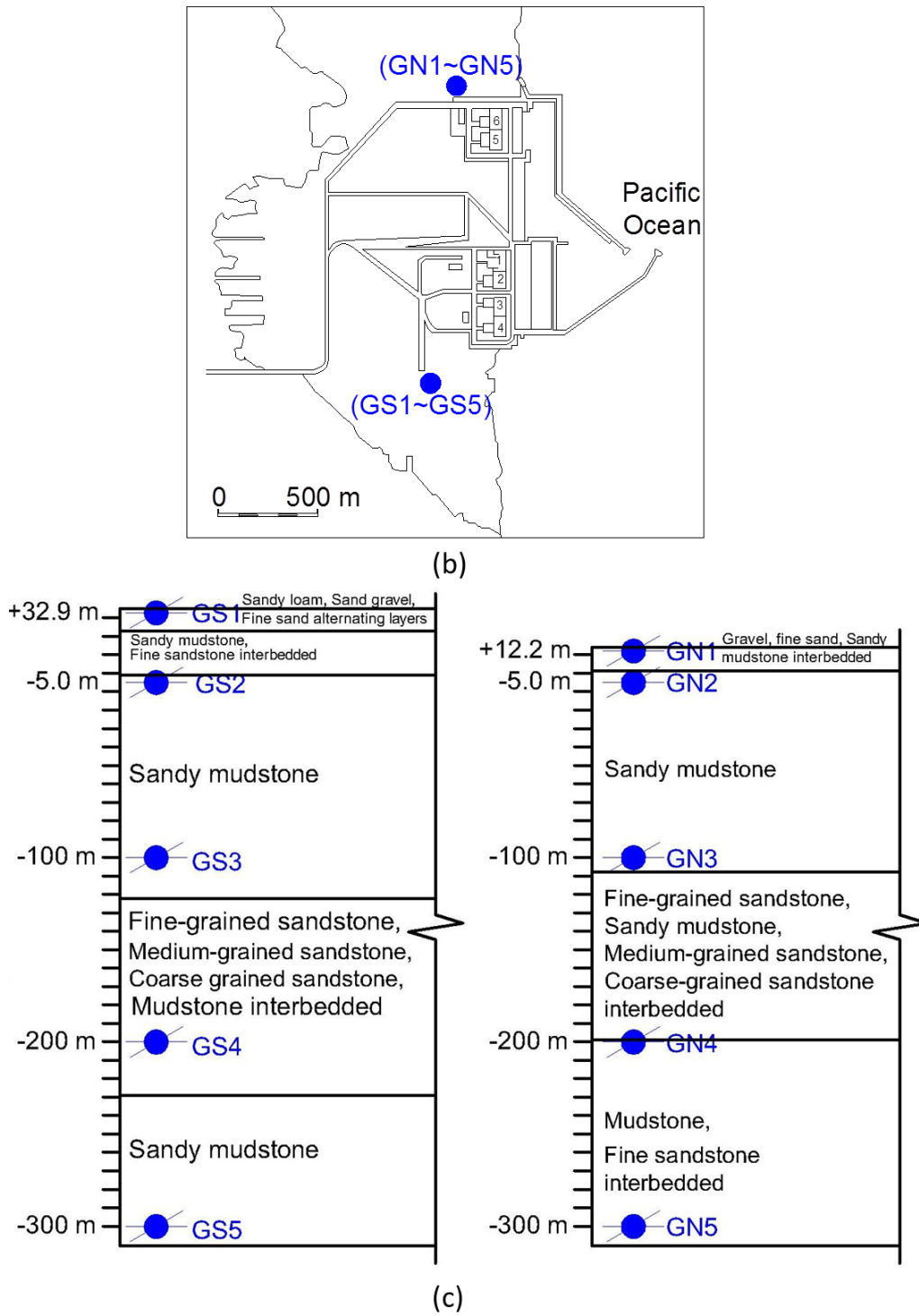


Figure 3.1 (continuation) (b) plan view of the Fukushima Daiichi nuclear power plant and; (c) ground cross section of the vertical arrays GN and GS.

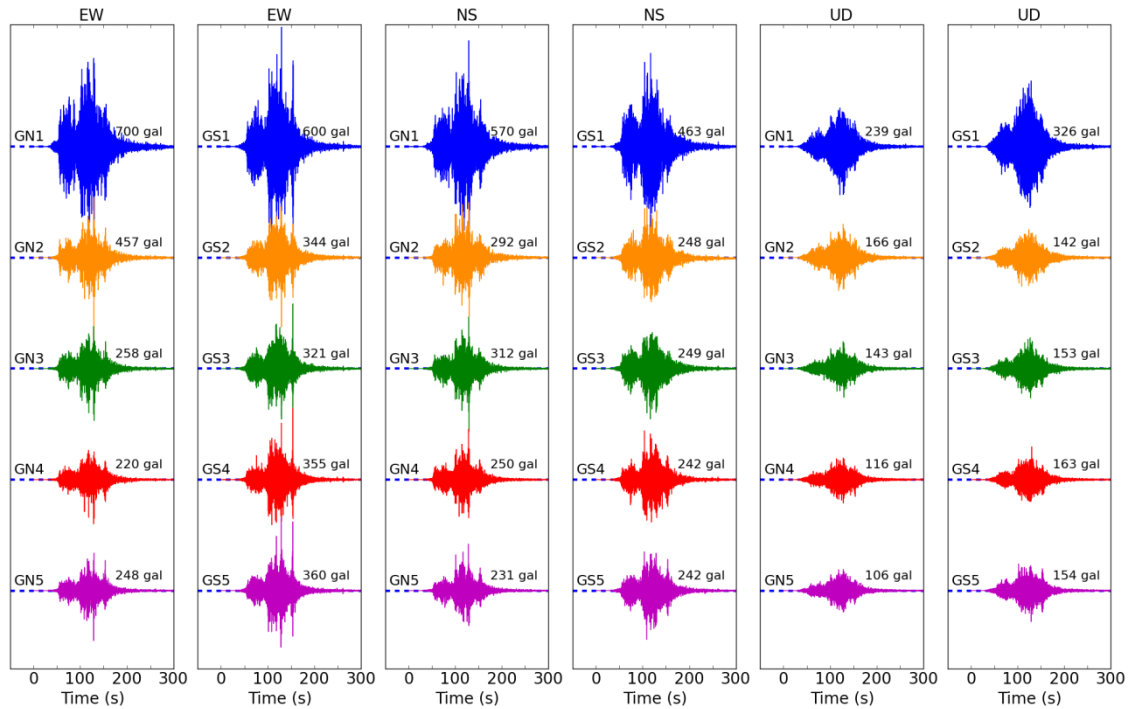


Figure 3.2 Ground acceleration records at GN and GS arrays from the Tohoku earthquake. For scale, the separation between horizontal dashed lines is 550 gals

3.1 Effects of the baseline shift in the ground velocity and ground displacement time history of the March 11, 2011 M_w 9.0 Tohoku earthquake

Figure 3.3 shows the velocity time history from a direct integration of the acceleration records. As mentioned previously, un-physical trend is observed in most of the cases and there is no record that oscillate around the zero line in the post-vent interval, which is a physical constraint (Boore, 2001). Instead, the linear trend observed in the post-event suggest that a shift in the baseline occurred. These baseline shifts is also present in the main-event interval; however, because the magnitude of the ground-motion acceleration, cannot be depicted easily. Only the vertical component of the GN1 shows a clearly linear trend at both main-event and post event intervals

It has been pointed out (Graizer, 2005; Boore, 2001) that one source of baseline offset is due to tilt of the station. Graizer (2005; 2010) analyzed the differential equation of small oscillations of horizontal pendulum motion and found that the vertical component of accelerometers is less sensitive to tilt than horizontal components. Figure 3.3 shows in general that the slope of the post-event interval of the horizontal component is greater than those obtained from the vertical component in most cases, which agrees with Graizer's statement. Boore (2001) evaluates the shift in baseline produced by a tilt of θ as:

$$\begin{aligned}\Delta a_h &= g \sin(\theta) \\ \Delta a_v &= g(1 - \cos(\theta))\end{aligned}\quad (3.1)$$

where Δa_h and Δa_v is the baseline shifts of the horizontal and vertical component, respectively. From equation (3.1) small tilt angle generates large shift in the baseline of the horizontal components and very low for the vertical component. Table 3.1 shows the tilt that would produce the baseline shift magnitude observed in the post-event interval for the horizontal and vertical component of each record. The baseline shifts was calculated from the last 100 seconds using the least squared method. The equivalent tilt angle for horizontal and vertical components shows substantial differences and suggest that another source of errors, different than tilt, contributed to the shift in the baseline.

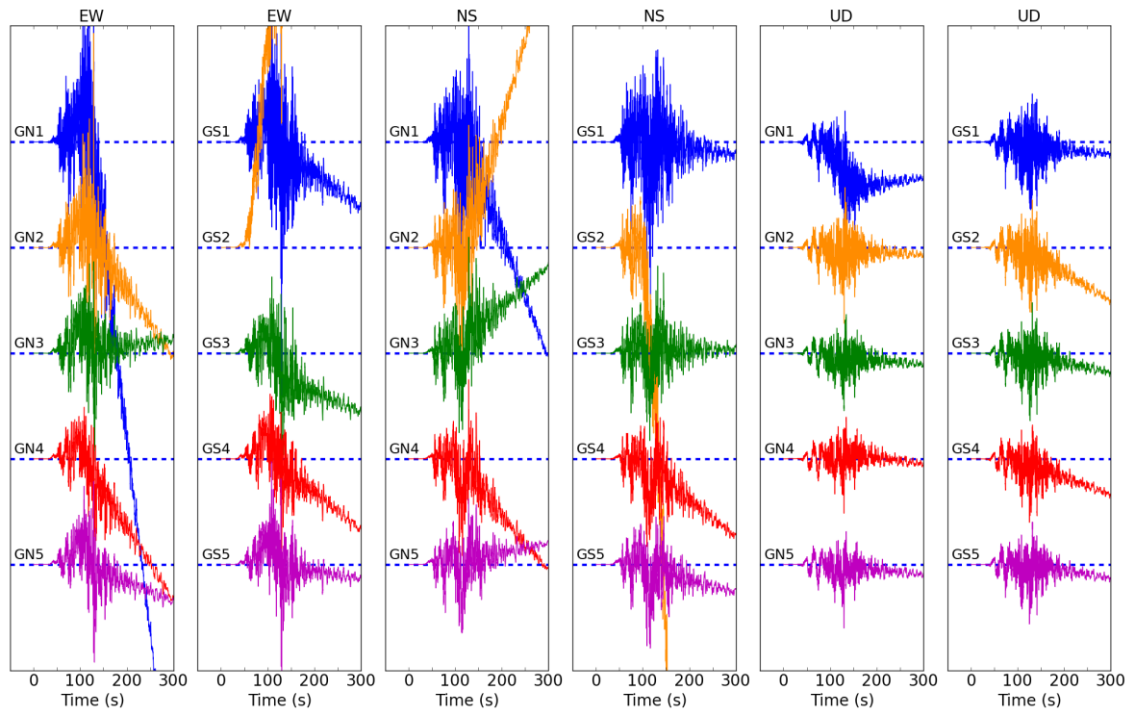


Figure 3.3 Direct integration of acceleration records. For scale, the separation between horizontal dashed lines is 30 cm/s.

Table 3.1. Equivalent tilt angle for the shift in the baseline

Accelerometer	Shift in baseline (gal)			Equivalent tilt (°)	
	EW	NS	UD	Horizontal	Vertical
GN1	-1.102	-0.350	0.019	0.068	0.361
GN2	-0.195	0.467	-0.008	0.030	0.238
GN3	0.018	0.117	-0.012	0.007	0.284
GN4	-0.211	-0.156	-0.020	0.015	0.366
GN5	-0.059	0.027	-0.013	0.004	0.301
GS1	-0.098	-0.022	-0.011	0.006	0.272
GS2	0.721	-3.424	-0.082	0.204	0.740
GS3	-0.054	0.000	-0.029	0.003	0.439
GS4	-0.106	-0.105	-0.049	0.009	0.575
GS5	-0.019	-0.036	-0.022	0.002	0.387

3.1.1 Velocity trend estimation using polynomials

In the standard literature of data analysis, the most frequent technique for trend removal is to fit a low order polynomial to the record, and is recommended not to use polynomial with order greater than three (Bendat and Piersol, 1986). The coefficients of the polynomial are calculated by minimizing the following expression:

$$Q = \sum_{n=0}^N \left[v_n - \sum_{k=0}^K p_k (n\Delta t)^k \right]^2 \quad (3.2)$$

where v_n is the uncorrected velocity data, N is the number of data, Δt is the space sampling interval, and p_k denotes the coefficients of the polynomial of degree K expressed by:

$$P_n = \sum_{k=0}^K p_k (n\Delta t)^k \quad n = 1, 2, \dots, N \quad (3.3)$$

Graizer in 1979 refers it as a common procedure at that time (Berg and Housner, 1961; Housner and Trifunac, 1967). Figure 3.4a shows the results of fitting a polynomial of 2nd (red line) and 3rd (blue line) degree to the uncorrected velocity. Although the polynomial seems to estimate reasonably well the trend, large discrepancies are observed in the pre-event interval of the record, which was not affected by the shift of the baseline. These effects are observed in most horizontal components. In order to improve the polynomial fitting, Graizer (1979) proposed to use only the pre-event $[0, T_1]$ and post-event $[T_2, T_e]$ intervals of the ground-motion when the polynomial coefficients are calculated. Then, the equation (3.2) is rewritten as:

$$Q = \sum_{n=0}^{T_1 f_s} \left[v_n - \sum_{k=0}^K p_k (n\Delta t)^k \right]^2 + \sum_{n=T_2 f_s}^N \left[v_n - \sum_{k=0}^K p_k (n\Delta t)^k \right]^2 \quad (3.4)$$

where f_s is the sampling frequency. We test this approach using polynomials of third and fifth order, as is suggested by Graizer (2004) and it was observed a good agreement between the polynomial fitted and the velocity trend; however, the displacement time history is high sensitive to the selection of the pre-event and post-event interval (T_1 and T_2). Figure 3.4b shows the Graizer's method using a polynomial of 3rd degree (red line) and 5th degree (blue line) with T_1 and T_2 as 50 and 225 seconds, respectively. A good improvement is provided in the estimation of the trend of the velocity. However, still some deficiencies are depicted in some records, such as the horizontal components of GS2. Besides, small differences in the main-event interval between the polynomial of 3rd and 5th degree is observed, but enough to produce large differences in the displacement record. It is worth to mention that we evaluate another modification of equation (3.2), where instead of discard the main-event interval, high weight factors were applied to the pre- and post-event. However, significant improvement was not achieved compared with Graizer's method.

3.1.2 Velocity trend estimation using linear segments

It is very difficult in most cases to determine the moment which the linear trend observed in the post-event ground velocity begins. Boore (2001) suggested a simple option in which the linear trend of the ground velocity is extended until it reaches the zero line. The result of this approach is shown in Figure 3.4c. It is seen that the method cannot be applied to the vertical component of GN1 because the post-event linear fit does not reach the zero line. Also, in some cases, such as the horizontal components of GS2, the velocity trend in the main event does not agree with the extension of the line derived from the post-event interval. Therefore, a more robust approach is needed for the networks GN and GS.

Two linear segments have been used to estimate the baseline shifts in previous earthquakes (Iwan, Boore, and Wu and Wu). The first line is assumed to be located in the main-event interval of the ground motion. The approach was more reasonable than only one linear segment because a bilinear segment can be interpreted as the average of the baseline shifts during the main- and post-event. However, the uncertainties is also increased. It is now necessary to estimate the beginning and the end of the first linear segment, which are known as time parameters t_1 and t_2 , respectively. Iwan (1985) proposed two approaches: (i) to select t_1 and t_2 as the times of the first and last occurrence of accelerations greater than 50 gals; and (ii) t_1 as the time of the first significant acceleration pulse and t_2 as the time that minimize the final displacement. Iwan's approach achieved a reasonable agreement in a laboratory test with a specific accelerometer. Later, Boore (2001) pointed out that the time parameters should not be constrained.

Several approaches have been proposed for the election of the time parameters. Wu and Wu (2007) pointed out that the displacement time history should be similar to a ramp function. Thus, t_1 was proposed as the time when the displacement move from the zero line, but must be greater than the time at which the acceleration first exceeds 50 gals, and t_2 is chosen from an interval between an additional time parameter, t_3 , and the end of the record. The parameter t_3 is the time when the displacement just moved to the permanent ground displacement and t_2 is the time greater or equal than t_3 that yields the maximum value of the f -parameter:

$$f = \frac{|r|}{|b| \cdot Var} \quad (3.5)$$

where r is the linear correlation coefficient, b is the slope of the least-squared regression line and Var is the variance. The f -value is calculated from the time t_3 to the end of the record. Later, Chao et al. (2010) proposed to modify t_1 and t_3 as the time when the acceleration energy reaches the 25% and 65% of the total acceleration energy. Figure 3.4d shows the linear trend estimation using both Wu and Wu (2007)'s method (red line) and Chao et al. (2010)'s method (blue line). Compared with Figure 3.4c, the improvement in the estimation of the velocity trend using a bilinear segment is clearly visible. However, in some records there is still some disagreement with the velocity trend, such as GS, East-West.

Another approach was proposed by Wang et al. (2011), where both t_1 and t_2 are located in the following intervals:

$$t_{PGD} \leq t_1 < t_2 \quad (3.6a)$$

$$\max(t_{D0}, t_{PGA}) \leq t_2 < t_f \quad (3.6b)$$

where t_{D0} is the time of the last zero crossing of the uncorrected displacement, t_{PGD} is the time of the peak ground displacement before time t_{D0} , t_{PGA} is the time of the peak ground acceleration, and t_f is an estimated end of the strong ground shaking. The time parameters are chosen through an iterative process to ensure that the corrected displacement best fits a step function. Figure 3.4e shows the bilinear segment calculated by Wang's method, where a good agreement is observed with the velocity trend for all stations.

3.1.3 Effect of the baseline correction on the displacement time history

In order to evaluate the performance of the baseline shifts correction methods, we evaluated the displacement record integrated from the velocity after removing the baseline shifts. Reasons why we use the displacement record are: (1) The availability of the displacement record from the GEONET 0203 station located approximately 12 km from the vertical arrays. The Tohoku event is a megathrust earthquake that produced permanent ground displacement in an area that extends approximately 400 km along the Japan trench (Ozawa, 2011). Therefore, the GNSS station is close enough to the vertical arrays (GN and GS) to consider it as a reference of the magnitude of the displacement recorded in the area; and (2) the accelerometers of the vertical array are located in stiff soil and rock. This implies that the magnitude of soil deformation is of several orders lower than the magnitude of crustal deformation. Hence, the magnitude of final displacement should be the same for all records.

Figure 3.5 shows the displacement record obtained from the different approaches mentioned in the previous section for each component of each ground-motion record. The displacement calculated from the GEONET 0203 station is shown as well (thick gray line); however, as mentioned before, only the first half of the displacement time history and the final displacement are available. It is observed that the final displacement obtained from acceleration records shows a wide range of variation for all results, where the records located close to the surface show large distortion. A reason of the high variability might rely on the complexity of the source rupture process due to the size of the fault. Figure 3.1a shows the fault model constructed from GNSS displacement observed by GEONET, which consists of two rectangular faults of longitude 186 km and 194 km. Such a long fault produced more than one strong-motion phase, as can be seen in the Figure 3.2. Therefore, methods that assume one simple ramp or step function would produce low accurate results.

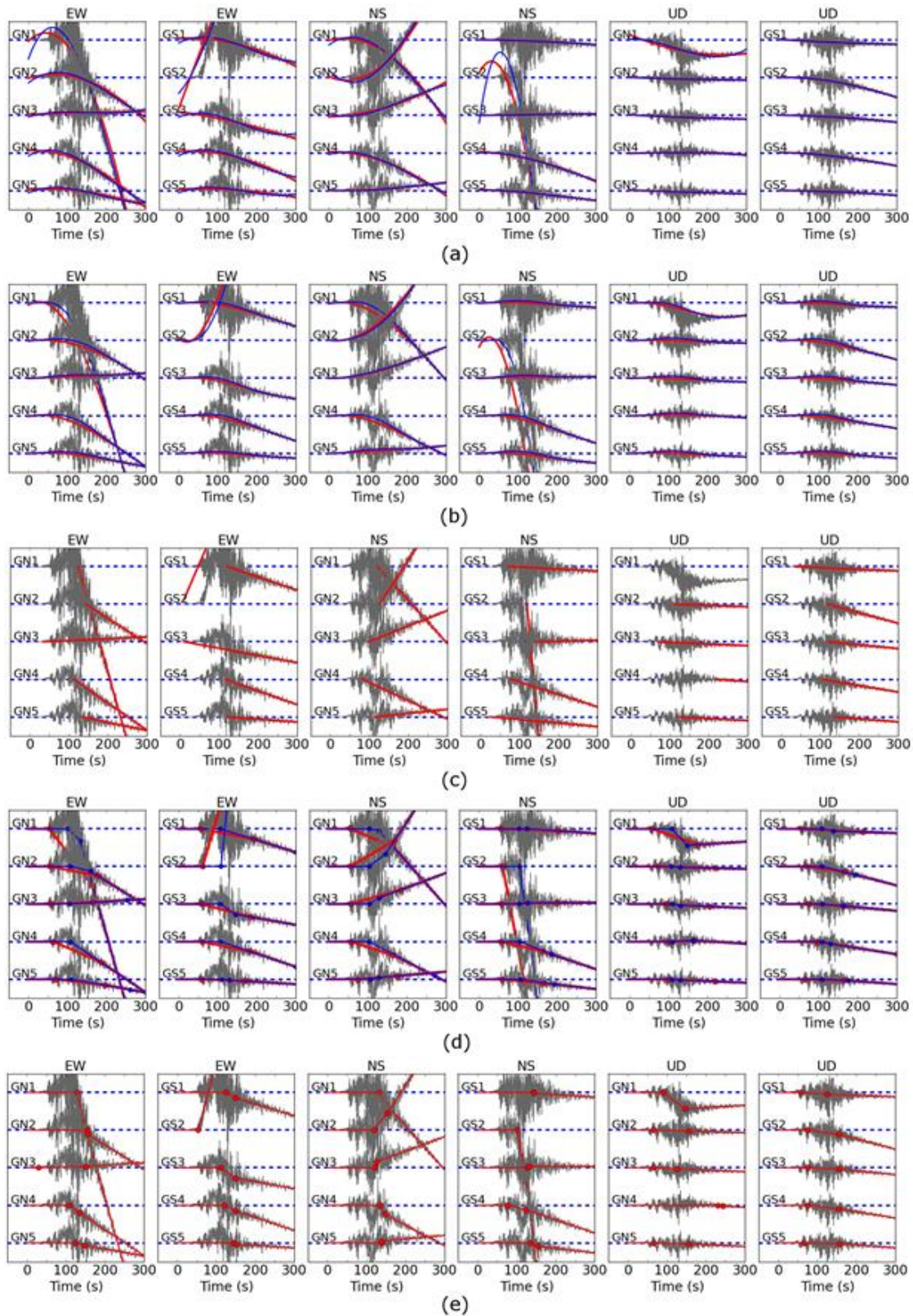


Figure 3.4 Estimation of the velocity trend. (a) polynomial of 2nd (red line) and 3rd (blue line) degree; (b) Graizer's method using 3rd (red line) and 5th (blue line) degree; (c) Boore's method; (d) Wu and Wu's method (red line) and Chao's method (blue line); (e) Wang's method (red line).

Considering that the vertical arrays (GN and GS) are separated by approximately 1.5 km. The two vertical arrays provide a total of ten acceleration records that should have the same permanent ground displacement. Therefore, it is possible to perform a basic estimation of statistical errors. Table 3.2 shows the permanent ground displacement for each component obtained from Wang's method and Table 3.3 depicts the average, bias, standard deviation, and root mean squared (rms) error. The mean and the standard deviation are calculated from the results shown in Table 3.2 for each component. It is worth to remember that the standard deviation describes the random error, the bias describes the systematic error and the rms error gives an estimation of the total error. The bias was estimated as the difference between the GNSS displacement and the mean. The calculation of bias can be questionable because the measurements of displacement must be performed under identical circumstances and although is the same earthquake event, recorded by the same accelerometer model and the true permanent ground displacement are almost equal, the accelerometers experienced different magnitude of the earthquake wave due to amplifications when the it is approaching to the surface. Even though, the authors consider that the estimation of the bias would provide some insights. In the case of the EW component, the bias and the standard deviation are of the same magnitude, whereas for the NS and UD the standard deviation is greater.

Table 3.2 Permanent ground displacement using Wang's method.

Station	EW	NS	UD
GN1	213.75	-58.00	-20.00
GN2	282.27	-65.59	-66.24
GN3	219.73	40.03	-83.01
GN4	70.51	-157.45	30.70
GN5	201.09	15.84	-69.14
GS1	164.29	-32.10	-44.32
GS2	140.80	-52.13	-32.31
GS3	125.20	25.22	-66.23
GS4	171.98	-57.82	-50.69
GS5	243.34	-86.46	-72.64

Table 3.3 Basic estimated statistical errors

Component	Mean (cm)	GNSS (cm)	Bias (cm)	Std (cm)	rms error (cm)
EW	183.30	259.20	75.90	61.79	97.87
NS	-42.85	-37.10	5.75	58.83	59.11
UD	-47.39	-53.70	6.31	33.64	34.23

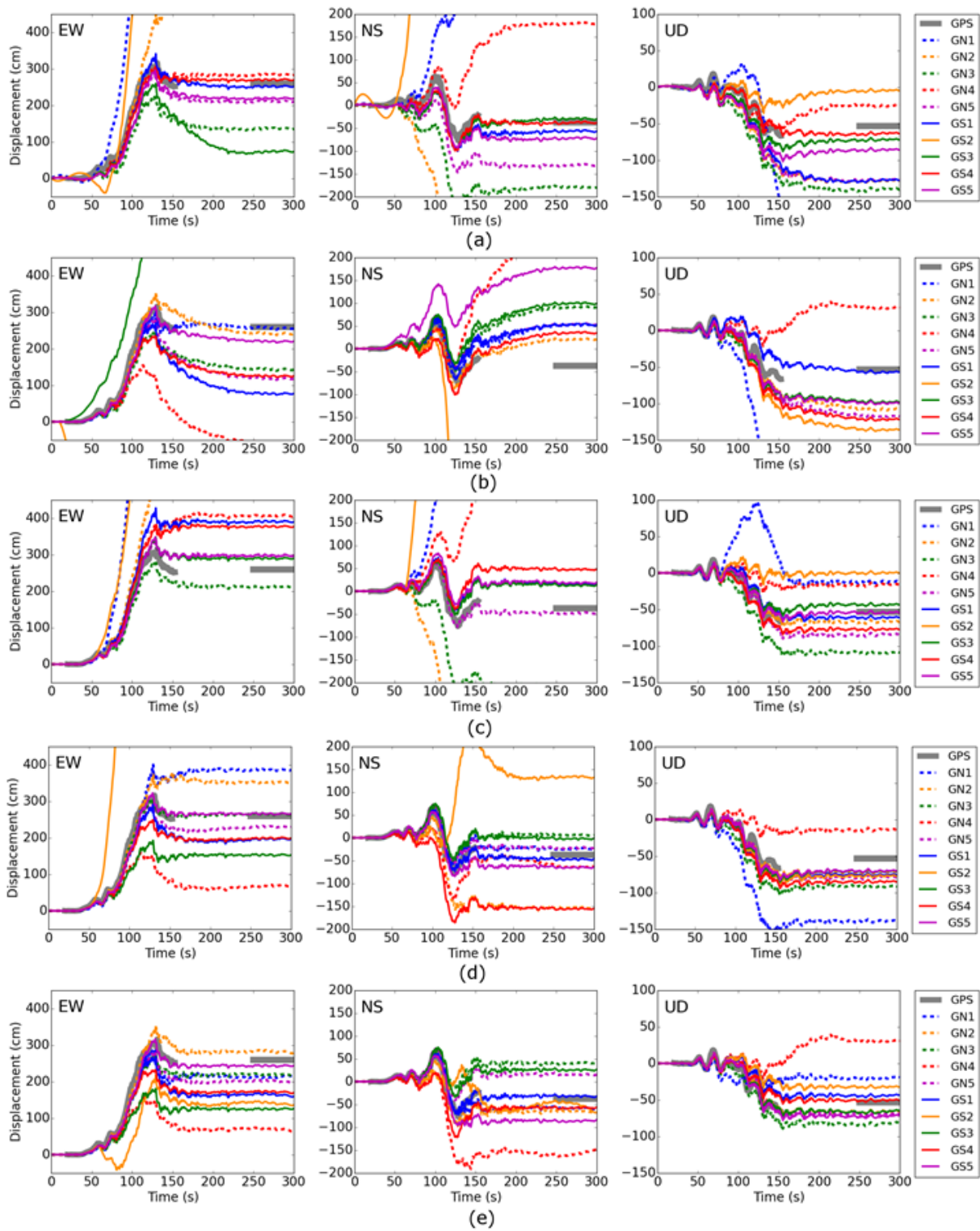


Figure 3.5 Displacement time history. (a) Graizer's method; (b) Boore's method; (c) Wu and Wu's method; (d) Chao's method; (e) Wang's method.

3.2 Effects of the permanent displacement in the response spectra

Baseline shifts affect mainly the low frequency component of the ground-motion record. Low component frequency is important to analyze the dynamic behavior of long-period structures, such as high-rise buildings, base isolated buildings, oil storage tanks, and suspension bridges. This issue was not important in the early stage of the accelerometer device because at that time structures with long fundamental period were scarce. However, nowadays baseline shifts correction without affecting low-frequency components that are important to evaluate long-period structures is necessary.

A standard and robust procedure to remove the baseline shifts is a low-cut filter, which change the record original spectral content. This change implies a reduction and/or removal of low-frequency components. Unfortunately, the process also affects the pulse-like waves that produce permanent ground displacement. Figure 3.6a and Figure 3.6b shows the acceleration, velocity and displacement of the East-west component of the GN5 station calculated by applying a low-cut Butterworth filter with 0.05 Hz and 0.1 Hz (see Figure 3.7) as the high-pass corner frequency. Figure 3.7 shows the magnitude spectrum of the Butterworth filter, where the cutoff frequency is defined as the point at which the gain drops to $1/\sqrt{2}$. Besides, Figure 3.6c shows the results of the same station by removing the bilinear trend observed in the uncorrected velocity record. Here, we select the time parameters that produce a displacement record that best fit the GNSS displacement. Notice that the GNSS displacement provides the opportunity of remove the low-frequency noise effects without eliminating the pulse-like wave that produce permanent ground displacement. The pulse-like wave mentioned is clearly depicted in the velocity time history of Figure 3.6c. Hence, there is a chance to evaluate the earthquake response of structures against the ground-motion record with low period components that contains pulse-like waves that produce permanent ground displacement.

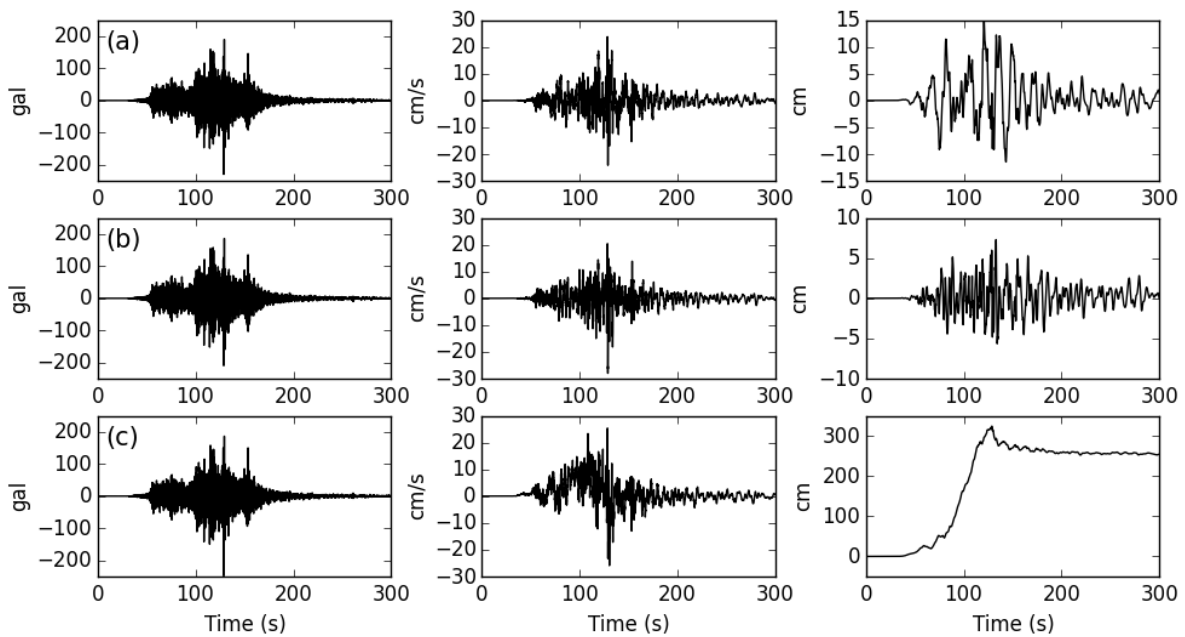


Figure 3.6 Baseline correction using (a) low-cut filter with $f_c = 0.05$ Hz, (b) low-cut filter with $f_c = 0.10$ Hz and (c) removing bilinear trend in the velocity ground motion

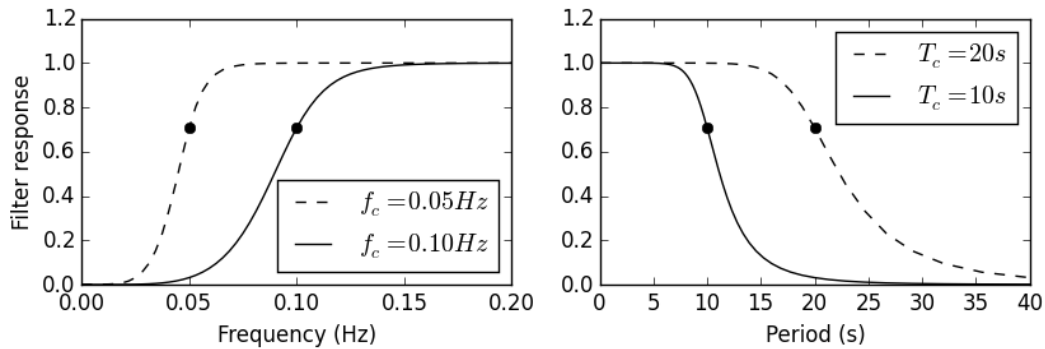


Figure 3.7 Butterworth filter frequency response (left) and period response (right)

This section discusses two issues. The effect of the baseline correction in the response spectra and the effect of the pulse-like wave that produced permanent ground displacement in long-period structures. Figure 3.8 shows the response spectra of the East-west component of the GN network, where the ground-motion was processed by three different methods: low-cut filter, remove the pre-event mean from the entire record, remove of the bilinear trend from the velocity ground-motion. For the purpose of this section, the time parameters t_1 and t_2 that define the bilinear trend are selected in order to fit the GNSS displacement record. The RS obtained from records with bilinear trend corrected are almost identical to those obtained from records with only mean removed. The only two exceptions that differs to this conclusion are the record at stations GN1 (EW component) and GS2 (EW and NS component), which show differences in RS for periods greater than about 15 seconds. A closer look of Figure 3.3 reveals that those stations show the largest distortion. It might suggest an existence of a relation between the level of distortion in the velocity ground-motion and the period at which RS will be sensitive. Besides, a good agreement is observed between the RS from record with low-cut filter and those obtained from the records with bilinear correction, obviously, in the interval that was not filtered.

The RS at Figure 3.8 also shows a local peak near to period 14 sec. This peak is depicted only in the EW and UD component, as shown in appendix A, which coincide with the directivity effect of the rupture propagation of the Tohoku earthquake, which is extended from the north end of Honshu Island to Tokyo Bay in the south with approximately 480 km (Stewart et al. 2013). However, that peak does not belong to the effect of the pulse-like wave that produced the permanent ground displacement. The evidence is that the filtered records with $f_c = 0.05 \text{ Hz}$ also detected that peak. Besides, probably such long period (about 14 seconds) has not effect on long-period structures. High-rise buildings that reported large deformation have fundamental periods in the range of 4.1 to 6.2 seconds (Takewaki 2003). However, results from RS are not conclusive and is necessary to perform time-history analysis of those long-period structures, which is out of scope of this paper.

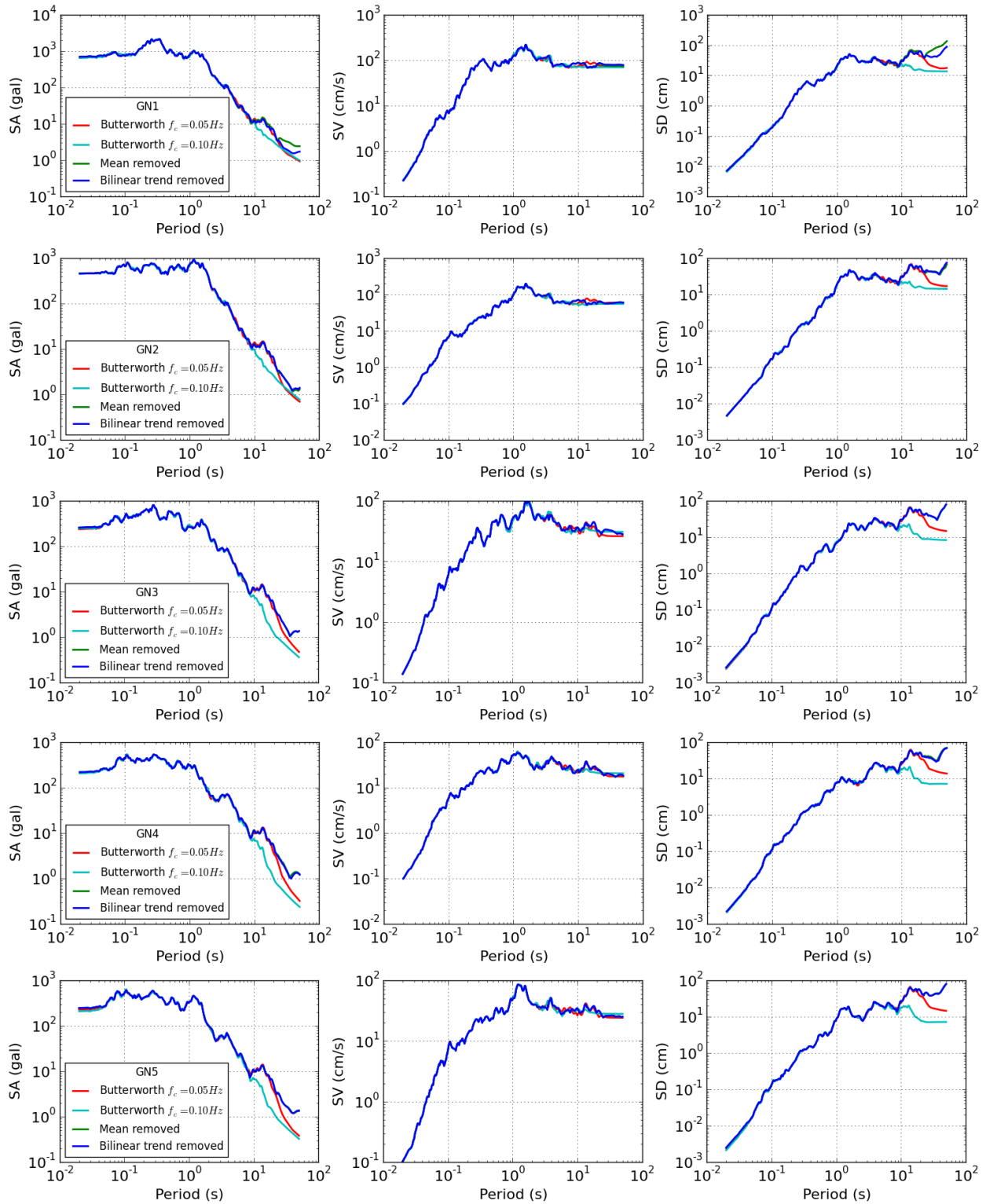


Figure 3.8 Earthquake response spectra of the East-west component of the GN network; damping ratio, $\xi=0.05$; SA: spectral acceleration; SV: spectral velocity; SD: spectral displacement.

3.3 Concluding remarks

Strong-motion records are of significant importance in the development of earthquake engineering and seismology. Ground velocity and displacement time history from a single and double integration of the acceleration recorded during the Tohoku earthquake have shown unphysical distortions produced by a shift in the baseline. This article presents and evaluate the techniques to reduce the effects of the baseline shifts in the ground velocity, ground displacement and response spectra of 10 ground-motion stations configured into two vertical arrays and located in the Fukushima Daiichi nuclear power plant. The configuration of the accelerometers provides the opportunity to assess the performance of different baseline correction schemes because the permanent ground deformation are mainly from crustal displacement rather than soil deformation. Thus, we can assume that the final displacement in all the stations should be equal. We observed a large variability in the final displacement. We also found that the pulse-like wave related to permanent ground displacement did not affect the interval of periods of the response spectra that is important in earthquake engineering. We observe also that records with high distorsions in the time history records also shows large distortion in period components of the response spectra.

Chapter 4

Comparison of coseismic displacement from GNSS and accelerometers

It is already recognized that permanent displacements estimated by the double integration of acceleration records need a suitable baseline correction. Current baseline correction methods have been validated by comparing the displacements with those from the Global Positioning System (GPS) records nearby, but GPS stations that are sufficiently close to a strong-motion station are scarce. Because the M_w 9.0 Tohoku-Oki earthquake produced permanent ground displacements in a wide area and because dense strong-motion and GPS networks are available in Japan, we interpolated the displacements calculated from GPS records to estimate the permanent ground displacements at 508 strong-motion stations. The estimated results were used to evaluate uncertainties in permanent displacements obtained using two automatic baseline correction methods, and results were found to be reliable only for KiK-net's borehole acceleration records.

4.1 Spatial distribution of coseismic displacement from GEONET

4.1.1 Kriging method

Baseline correction methods have been examined by comparing the final corrected displacement with that of the nearest GPS station (Boore, 2001; Wu and Wu, 2007; Wang et al., 2013). However, this approach cannot be widely used because only few strong-motion stations are located sufficiently close to GPS stations. Considering this fact, we apply the kriging interpolation method (Cressie, 1991) to the GEONET data for the 2011 Tohoku-Oki earthquake to estimate the crustal movement at all the K-NET and KiK-net stations. Then, the corrected displacements obtained from acceleration records after applying baseline correction are compared with the estimated GPS displacements.

Using the kriging method, the displacements recorded by the GEONET stations were interpolated to estimate the distribution of crustal movement at a specific location s_0 by the following equation:

$$\hat{Z}(s_0) = \sum_{i=1}^N \lambda_i Z(s_i) \quad (4.1)$$

where $Z(s_i)$ denotes the displacement measured by a GEONET station located at s_i , $\hat{Z}(s_0)$ is the predicted displacement at a location s_0 , λ_i is the unknown weight factor for the measured value $Z(s_i)$, and N is the number of GEONET stations used in the interpolation. The weight factors λ_i 's are determined from a mathematical model fitted from the experimental semivariogram, and their summation value is 1.0.

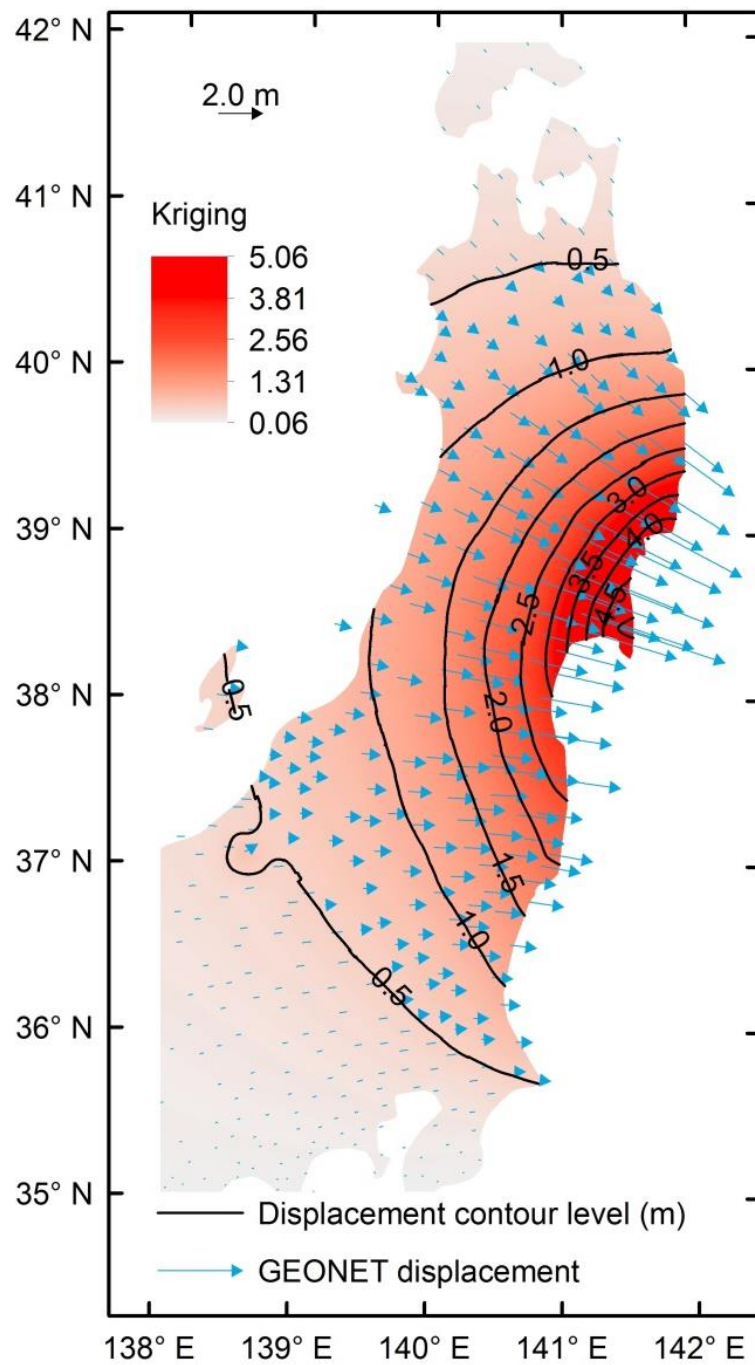


Figure 4.1a Spatial distribution of horizontal permanent displacement obtained from GEONET by using Kriging interpolation

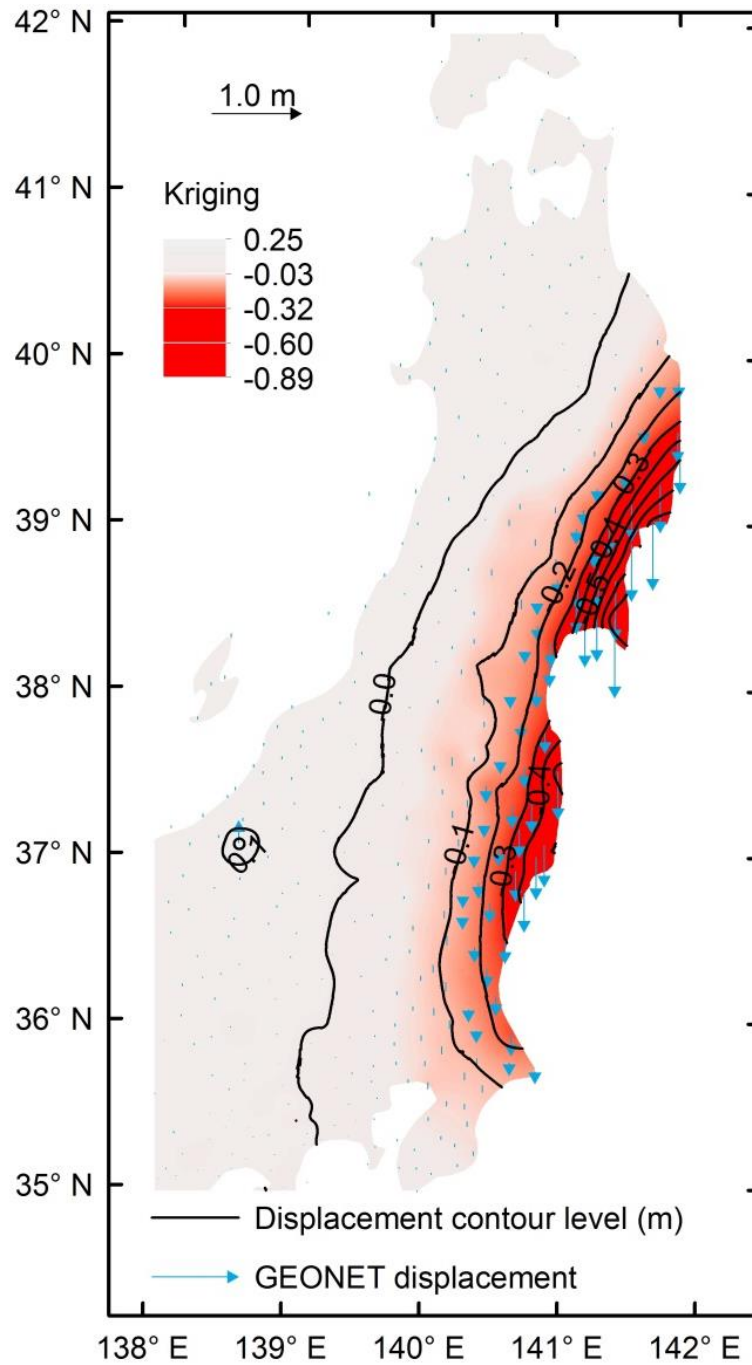


Figure 4.1b Spatial distribution of vertical permanent displacement obtained from GEONET by using Kriging interpolation

Table 4.1 Comparison between displacements obtained from GPS and kriging interpolation.

Stations	East-West component			North-South component			Up-Down component		
	GPS (m)	Kriging (m)	Error (%)	GPS (m)	Kriging (m)	Error (%)	GPS (m)	Kriging (m)	Error (%)
0546	2.97	3.01	1.6	-1.67	-1.68	0.6	-0.41	-0.44	7.3
0937	1.24	1.23	0.5	-0.10	-0.10	2.0	-0.04	-0.04	2.4

Note: The error values were calculated using four-digit numbers.

4.1.2 Coseismic displacement from GEONET

Figure 4.1 shows the results of kriging interpolation for the permanent displacement produced by the 2011 Tohoku-Oki earthquake. The displacements at the GEONET stations were calculated from the difference between the station's coordinates on March 10, 2011 and March 12, 2011; these coordinates were provided by the GSI. The arrows indicate the GEONET's data, and the shades indicate the displacement distribution by kriging interpolation. Twelve neighboring GEONET data values were used for each prediction point. The accuracy of the prediction was assessed by removing two GEONET stations (0546 and 0937) and using the remaining GEONET data to predict the values at the removed stations. The results of this examination are listed in Table 4.1. Because the crustal movement in the event extended to the wide area rather smoothly and the GEONET stations were deployed rather densely, the maximum error in the horizontal components was only 4 cm (1.6%) and that in the vertical components was 3 cm (7.3%), which is observed in the station 0546.

4.2 Coseismic displacement from strong ground motion

Baseline correction was applied to all the strong ground motion records from K-NET and KiK-net whose stations were located in the study area shown in Figure 4.2. The records from a total of 310 K-NET stations and 198 KiK-net stations were processed. Considering that KiK-net stations have two accelerometers (at the bedrock and surface) and each accelerometer provides three components, a total of 2,118 records were used. Owing to the large number of records, this study adopted the methods proposed by Chao et al. (2010) and Wang et al. (2011) because these methods were based on an automatic scheme. For the sake of brevity, the baseline correction methods of Chao et al. (2010) and Wang et al. (2011) are hereafter referred to as Chao's method and Wang's method, respectively.

Additional details related to Wang's method are provided below. Equation (3.6b) implies that t_{D0} is smaller than t_f , but some records showed the opposite result. For such cases, we only inverted the order of the equation ($t_f \leq t_2 < \max(t_{D0}, t_{PGA})$) to avoid major modifications in the procedure. Moreover, during the iterative process, the variance between the corrected displacement and its fitted step function was used to judge the best time parameters.

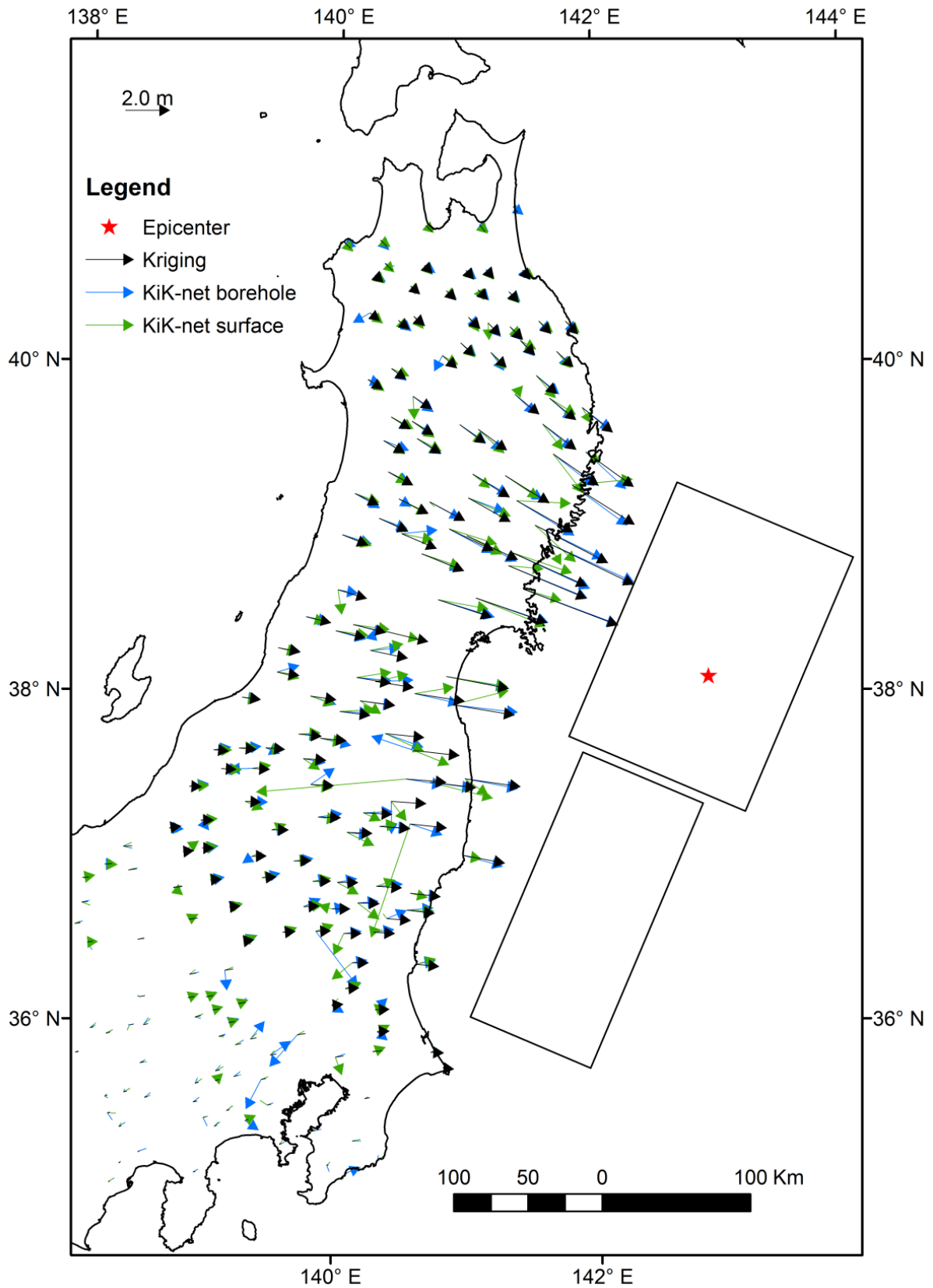


Figure 4.2a Distribution of horizontal permanent displacement after the Tohoku-Oki earthquake obtained from the interpolation of GEONET data and Wang's method.

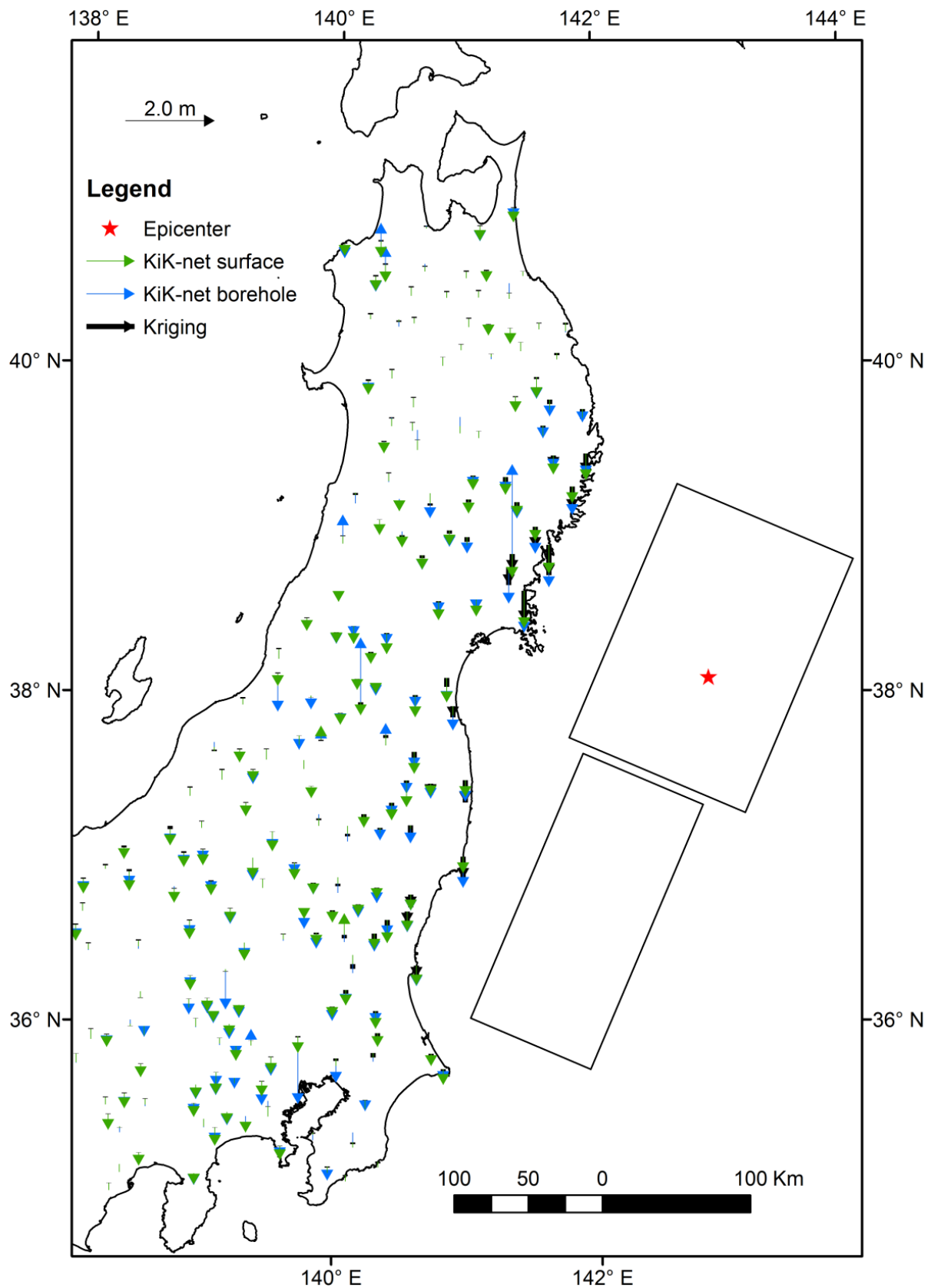


Figure 4.2b Distribution of horizontal permanent displacement after the Tohoku-Oki earthquake obtained from the interpolation of GEONET data and Wang's method.

4.2.1 Comparison of coseismic displacement from strong ground motion and GEONET

The coseismic displacements obtained from acceleration records were compared with the results obtained by kriging of the GEONET data (Figure 4.2). Because GPS displacements guarantee an accuracy of a few centimeters and the 2011 Tohoku-Oki earthquake produced displacements of a few meters, we considered the results from kriging to be the truth data. It is observed that the results for horizontal displacements from the acceleration records at the bedrock agree reasonably well with those from kriging. In contrast, horizontal displacements from the acceleration records at the surface are dispersed without a clear trend. The poor results for K-Net and KiK-net surface records were also observed by Hirai and Fukuwa (2012) and Wang et al. (2013). They attributed this uncertainty to the soil conditions of the seismic stations, where nonlinear baseline shifts were possibly produced. The vertical component of permanent displacements from acceleration records, either bedrock or surface, show large differences from that of GEONET because the displacements are small, and even the horizontal components show high dispersion at these level of amplitudes.

To quantitatively compare the results, least-squares regression lines assuming a constant standard deviation were obtained and are shown in Figure 4.3. The results from the KiK-net bedrock are focused upon because only these results show linear trends; no major difference is observed in the slope of the linear trend, which is close to one, with the exception of the vertical component results. In addition, the standard deviation obtained from Wang's method is lower than that from Chao's method for all components. The average of the standard deviation from the three components is 36.7 cm and 98.0 cm for Wang's method and Chao's method, respectively. These results suggest that Wang's method shows better accuracy.

A closer look at the results shows that better accuracy is achieved when the permanent displacement is large. This trend is clearly observed in Figure 4.4, where the vertical axes shows the ratio of the results calculated using Wang's method to the results calculated from the GPS, and the horizontal axes shows the lateral displacement from GPS. The accuracies of both the amplitude of the horizontal component (the resultant of two directions) and its direction (the angle from the north) are shown in Figure 4.4. Strong-motion stations with permanent displacements greater than 1 m show almost uniform variability with the exception of a few points. The average ratio for these stations is 0.95 ± 0.12 for the amplitude and 1.04 ± 0.31 for the azimuth. In contrast, stations with permanent displacements less than 1 m show results with high dispersion. On the other hand, it is well understood that the largest displacements are located near the source; therefore, Figure 4.4 provides insight into how the maximum distance between the station and the source can be used as a threshold to filter poor results. However, data from several events with different magnitudes are necessary for this purpose, which is outside of the scope of this research.

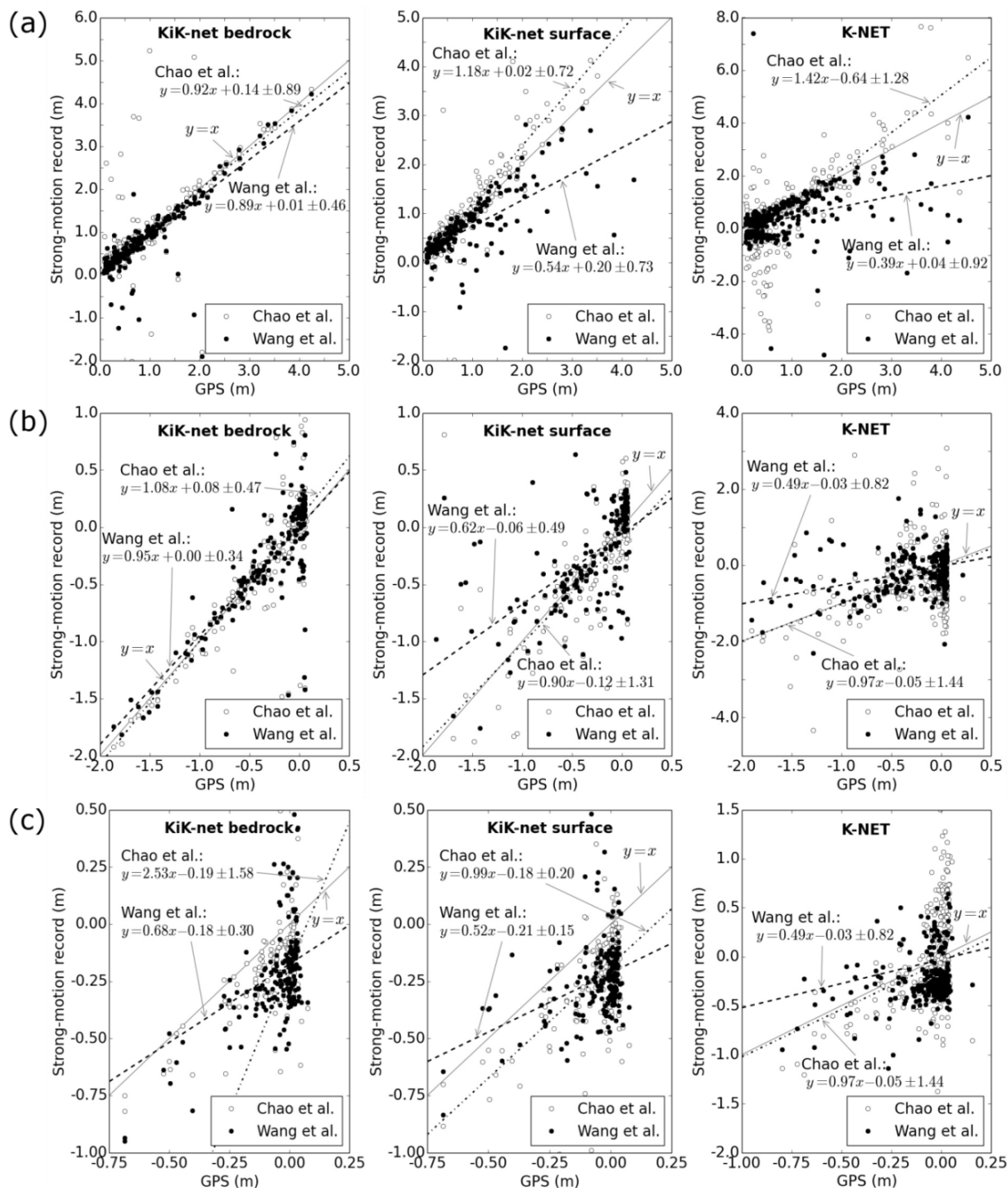


Figure 4.3 Comparison between permanent displacement obtained from kriging of GEONET data and from acceleration records for (a) EW component, (b) NS component, and (c) UD component. The symbols x and y are the abscissas and ordinates, respectively. The linear equations calculated from least-squared regression are expressed in meters.

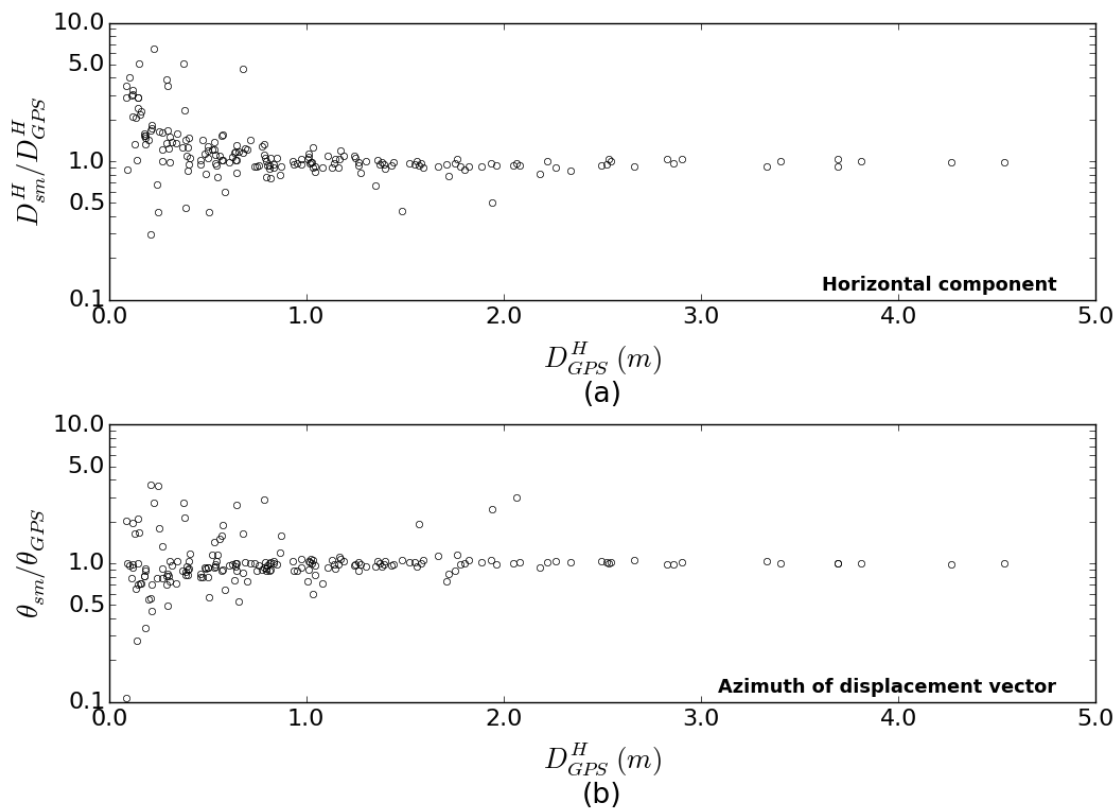


Figure 4.4 Ratio of coseismic displacements calculated from Wang et al. (2011)'s method and the one obtained from the interpolation of GPS data for the KiK-net bedrock sites. (a) Horizontal component and (b) displacement azimuth.

4.3 Concluding remarks

In this section, the effect of baseline shift in acceleration records on the estimation of permanent displacements was evaluated. For this purpose, a large amount of strong-motion data recorded by KiK-net and K-NET during the M_w 9.0 Tohoku-Oki earthquake was used. Two automatic baseline correction methods proposed by Chao et al. (2010) and Wang et al. (2011) were selected to remove the effects of baseline shift and estimate the permanent displacement. The results were compared with a more accurate displacement obtained from the kriging interpolation of GEONET data. The results showed that the current baseline correction methods could not obtain reliable permanent displacements for acceleration records at the ground surface. In contrast, reasonable results were found for acceleration records at the bedrock: Wang's method yielded the best results with a standard deviation of 46 cm, 34 cm, and 30 cm for the EW, NS, and UD components, respectively. Such a difference between the results from records at the surface and bedrock was also observed by Hirai and Fukuwa (2012) and Wang et al. (2013). This is a disadvantage because most strong-motion accelerometers are located on the ground surface. In addition, high precision in amplitude and orientation has been observed in stations that develop large permanent displacements; the accuracy decreases as the permanent displacement reduces. This observation suggests that a minimum distance between the source and the strong-motion station can be used as a threshold to filter poor results.

Chapter 5

Proposed method of baseline correction for KiK-net

A new approach to select the most suitable baseline shift for KiK-net stations is proposed. The baseline correction methods used in previous studies determine the time parameters in such a way that the corrected displacement best fits some shapes such as a ramp function (Wu and Wu, 2007; Chao et al., 2010) or a step function (Wang et al., 2011). Furthermore, the time parameters are restricted in some intervals under certain criteria (e.g., Eq. (2) and (3)).

5.1 Hypothesis

Because each KiK-net station has two accelerometers (at the bedrock and surface levels), this advantage can be used to estimate the coseismic displacement without the necessity of restraining the time parameters or fitting the results to a shape function. Considering that in a large earthquake, the residual soil deformation at the ground surface is much smaller than that of the crustal movement, the permanent displacement should be almost the same at the surface and bedrock. On the other hand, each accelerometer is affected by the baseline shift in a different manner because the factors producing the shift, such as the acceleration level and confinement condition of the sensor, have different values for each accelerometer (See Figure 5.1).

We introduce the assumption that the corrected displacements obtained from the surface and bedrock records are equal or very close to each other and use this property to estimate the time parameters for both records.

5.2 Previous definitions

First, note that although the displacements are very similar, the time parameters are not equal for both records; thus, an extra index (b for bedrock and s for surface) is required to differentiate between them. To control the similarities, we use the sum of squares of the differences between the corrected displacements at the bedrock and surface as follows:

$$S(t_1^b, t_2^b, t_1^s, t_2^s) = \sum_{j=1}^N \left(D_j^b(t_1^b, t_2^b) - D_j^s(t_1^s, t_2^s) \right)^2 \quad (5.1)$$

where j denotes the position of a control point in the record, N is the number of control points, and $D_j^i(t_1^i, t_2^i)$ is the corrected displacement obtained at the control point j using the time parameters t_1^i, t_2^i . Equation (5.1) is considered to be pseudo-variance because if the number of control points is equal to the number of data points in the record, the pseudo-variance will be equal to N times the variance. Finally, the objective of our proposal is to find a set of time parameters (t_1^b, t_2^b, t_1^s and t_2^s) that will reduce the pseudo-variance to its minimum value.

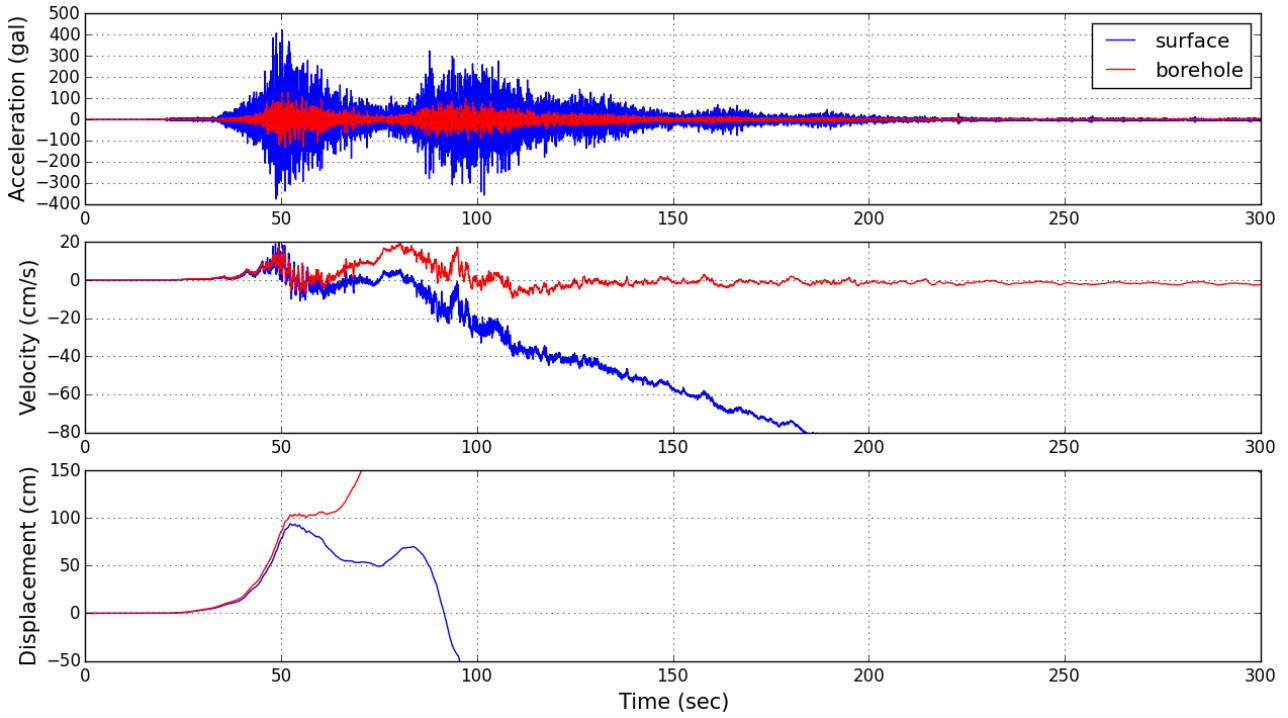


Figure 5.1 Acceleration (left), uncorrected velocity (center) and uncorrected displacement (right) from KiK-net station MYGH03 during Tohoku-Oki earthquake.

The minimum value of S can be calculated by an optimization process or a suitable grid search approach. However, these methods require repetitive operations that would involve large computational efforts because the pseudo-variance is a fourth-dimensional function. To reduce the computational efforts, it is recommended that the corrected displacement be calculated directly from its mathematical meaning and not by a numerical integration procedure. Here, the corrected displacement at a control point represents the difference between the uncorrected displacement and the integration of the linear trend observed in the velocity time history. Therefore, the corrected displacement is expressed as:

$$D_j(t_1, t_2) = \begin{cases} d_j, & t_j < t_1 \\ d_j - \int_{t_1}^{t_j} (a_m t + v_{m0}) dt, & t_1 \leq t_j < t_2 \\ d_j - \int_{t_1}^{t_2} (a_m t + v_{m0}) dt - \int_{t_2}^{t_j} (a_f t + v_{f0}) dt, & t_2 \leq t_j \end{cases} \quad (5.2)$$

where d_j is the uncorrected displacement at time t_j . If the corrected displacement, D_j , is calculated by numerical integration, a process of adding up the value of the integrand at a sequence of all abscissas before a control point will be necessary. On the other hand, equation (5.2) implies that the uncorrected displacement, d_j , needs to be computed only once using any numerical integration procedure.

5.3 Validation and analysis

Figure 5.2 shows a comparison between displacement time histories obtained from our joint parameter search method and Wang’s method. The records used belong to the KiK-net IWTH27 and SZOH33 stations. The displacement obtained by interpolation of GPS data is also shown in the figure. On the basis of our proposal, the time parameters were found using a grid search approach and the pseudo-variance was calculated using 50 control points uniformly distributed over the record (every 6 s). As pointed out previously, Wang’s method yields different values for the records recorded at the surface and bedrock, with the one at the bedrock being more accurate. On the other hand, when both records are combined on the basis of our proposal, the same level of accuracy is obtained for both records. Figure 5.3 shows the permanent displacements produced by the Tohoku-Oki earthquake, obtained from all the stations located in our study area using the joint parameter search method, Wang’s method, and the interpolation from GPS data. The figure clearly indicates that our method produces better results for the KiK-net surface records than the existing methods. This implies that removing the linear trend from the velocity record is a good practice for surface records as well. This result demonstrates that it is possible to obtain better time parameters t_1 and t_2 for KiK-net surface accelerometers than the ones obtained using previous methods.

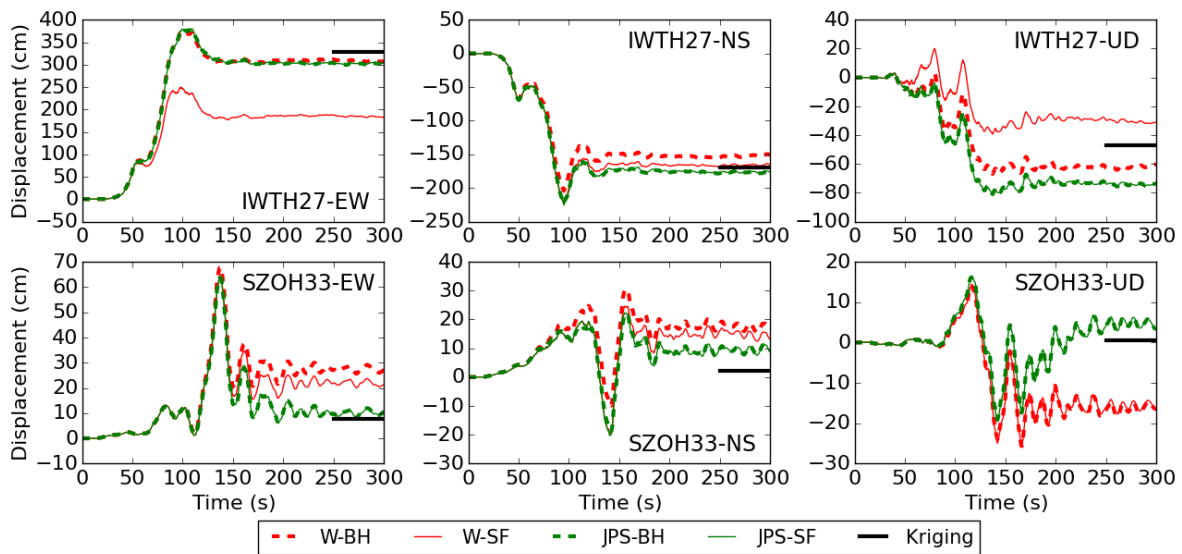


Figure 5.2 Corrected displacement record from Wang et al. (2011)’s method and joint parameter search for the KiK-net IWTH27 and SZOH33 stations (W: Wang et al. (2011); JPS: Joint parameter search; BH: borehole accelerometer; SF: surface accelerometer).

However, at some locations, the results are different between bedrock and surface, with the main reason being a non-linear trend observed in the baseline shift, which cannot be removed properly by a bi-linear correction. As an example, Figure 5.4 shows the corrected displacement obtained from three pairs of time parameters for the station FKSH18, in which t_1 is constant (100 s) and t_2 : 138 s, 139 s, and 140 s. It is

observed that an increment of 1 second in t_2 produces an increment of 2 meters in the final displacement. This high sensitivity to the time parameters makes it difficult to obtain very similar results between bedrock and surface when using our method.

Figure 5.5 shows a scatter plot comparison between permanent displacements obtained from the kriging of GEONET data and using the joint parameter search method. The least-squares regression lines obtained from the results have a slope close to one and indicate significant improvements in the standard deviation for the KiK-net surface records compared with the results shown in Figure 4.3. Hence, the results shown in Figure 5.3b are confirmed.

The corrected displacement time history was evaluated by comparing it with the 30-s GPS displacements obtained from a nearby GEONET station for 12 cases; the separation between the KiK-net and GEONET stations was within approximately 5 km. The GPS displacements were calculated by applying the KPPP technique using the RTKLIB software; final precise orbit information of every 15 min, 30-s satellite clock, and absolute antenna phase center variation (PCV) models were used. The elevation cut-off angle for the GPS satellites was 10° . Figure 5.6 compares the displacement time histories from the joint parameter search method and GEONET stations. Good agreement is found between the KiK-net and GEONET records although slight differences are observed after the permanent displacement is achieved. However, the most remarkable characteristic is that both the KiK-net surface and bedrock records show the same level of accuracy.

Significant difference is observed between the FKSH04 (KiK-net) station at the bedrock and the 0939 (GEONET) station. Direct evidence of error in the installation angle was found for FKSH04 station. Figure 5.8 shows the uncorrected velocity and displacement of the east-west and north-south component of FKSH04 and stations nearby (see Figure 5.7). Besides, the total horizontal component is shown as well. From the uncorrected velocity, it can be assumed that in the early part of the record the baseline shift has not affected significantly the record. Thus, evaluating the first 100 seconds and considering the low spatial variation of coseismic displacement during the Tohoku earthquake, it can be observed that the displacement time history of FKSH04 station is lower than the other stations in the east-west(EW) component, and greater in the north-south (NS) component. However, the total horizontal displacement ($|EW+NS|$) is very close to most of the stations. This anomaly is due to the effect of the orientation error of the three-component accelerometer about the vertical axis. However, even in this case, using our approach the final permanent displacements are very close to that from GEONET.

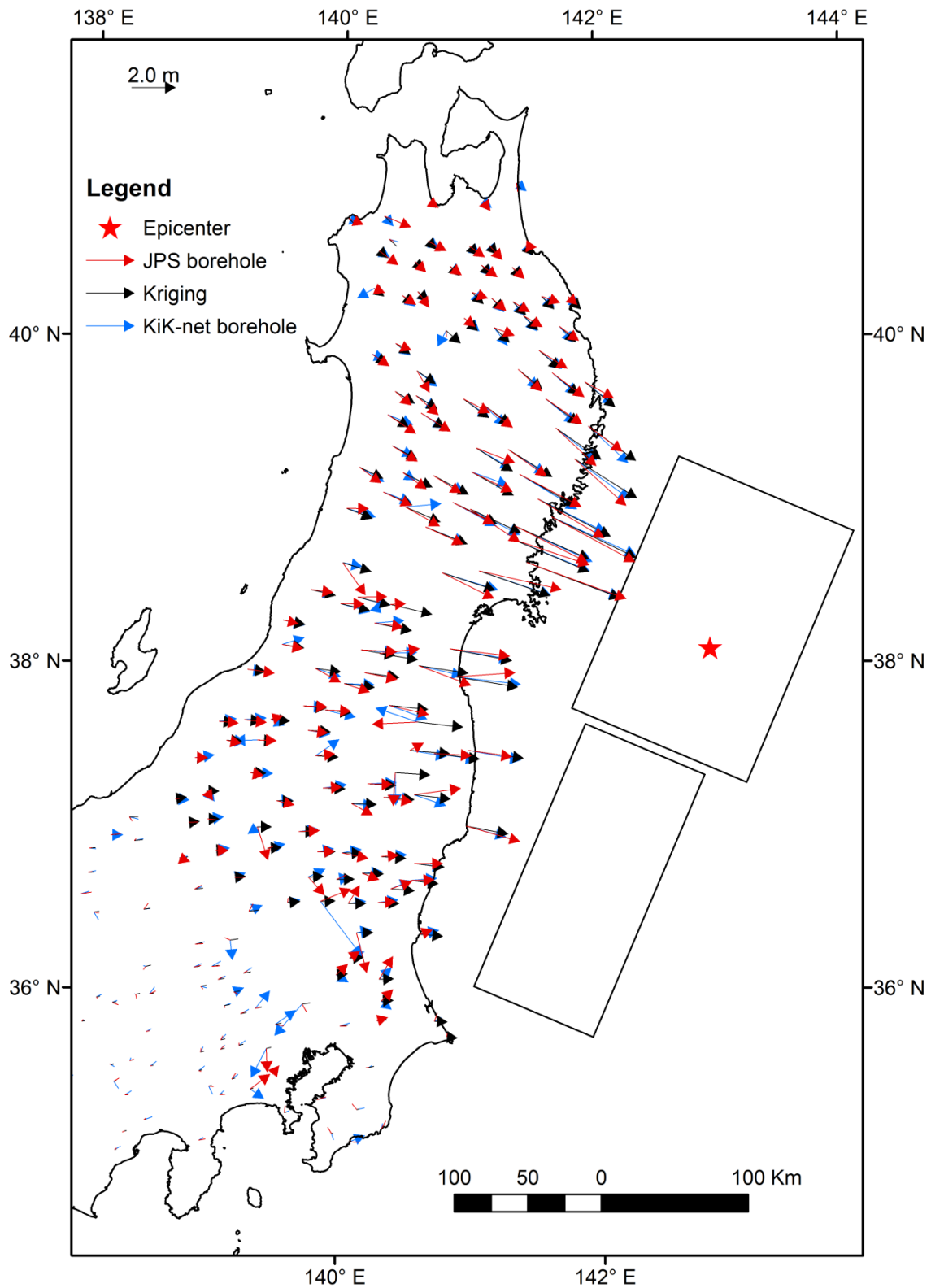


Figure 5.3a Distribution of permanent displacement after the Tohoku-Oki earthquake obtained from the interpolation of GPS data, Wang's method, and the joint parameter method for KiK-net bedrock.

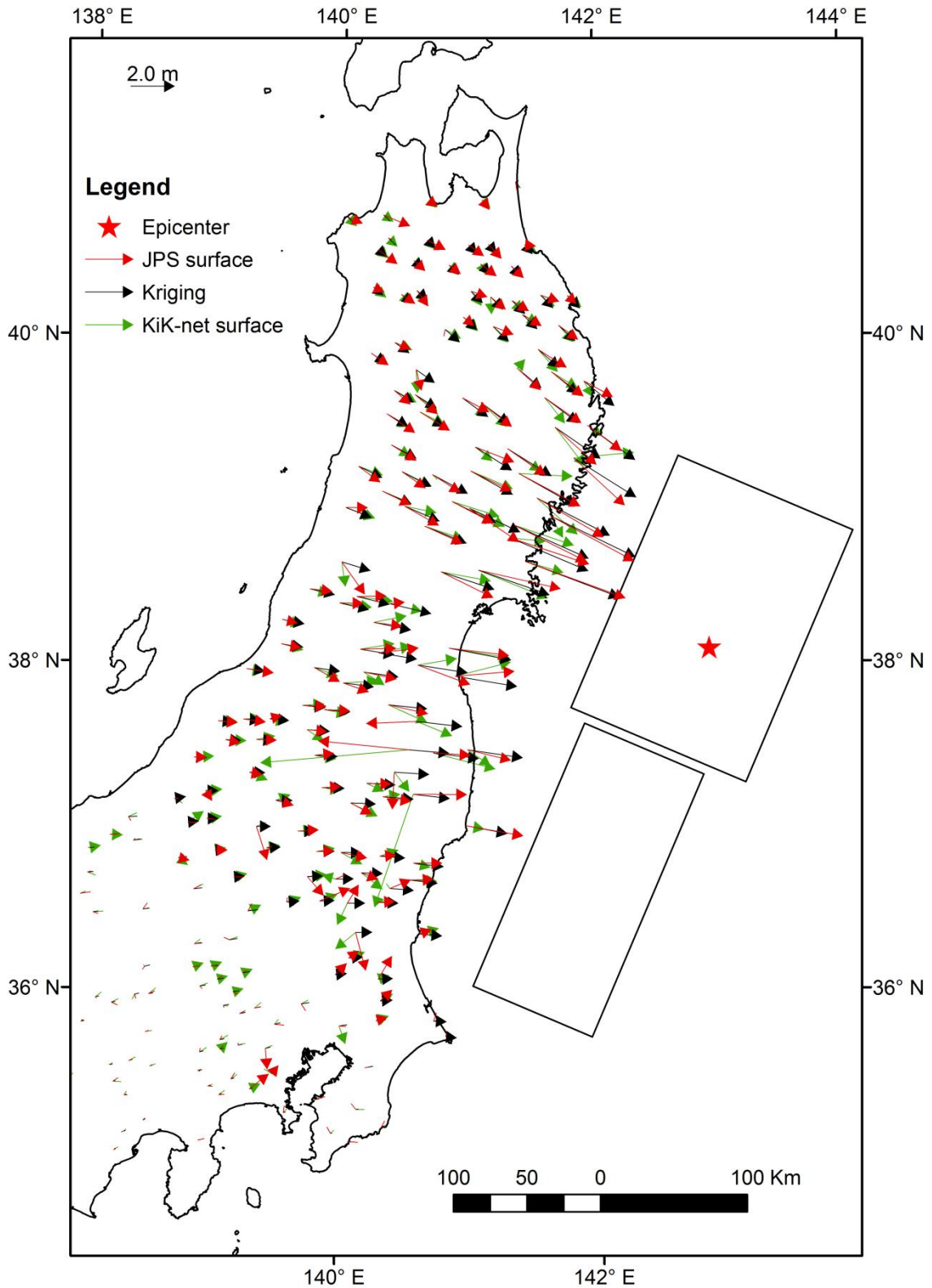


Figure 5.3b Distribution of permanent displacement after the Tohoku-Oki earthquake obtained from the interpolation of GPS data, Wang's method, and the joint parameter method for KiK-net surface.

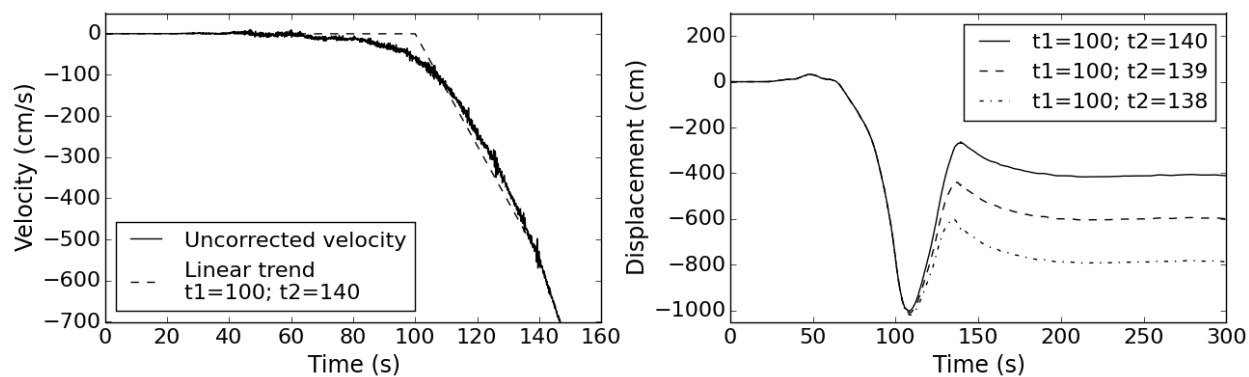


Figure 5.4 Uncorrected velocity and corrected displacement using three pairs of time parameters for the KiK-net KSH18 station.

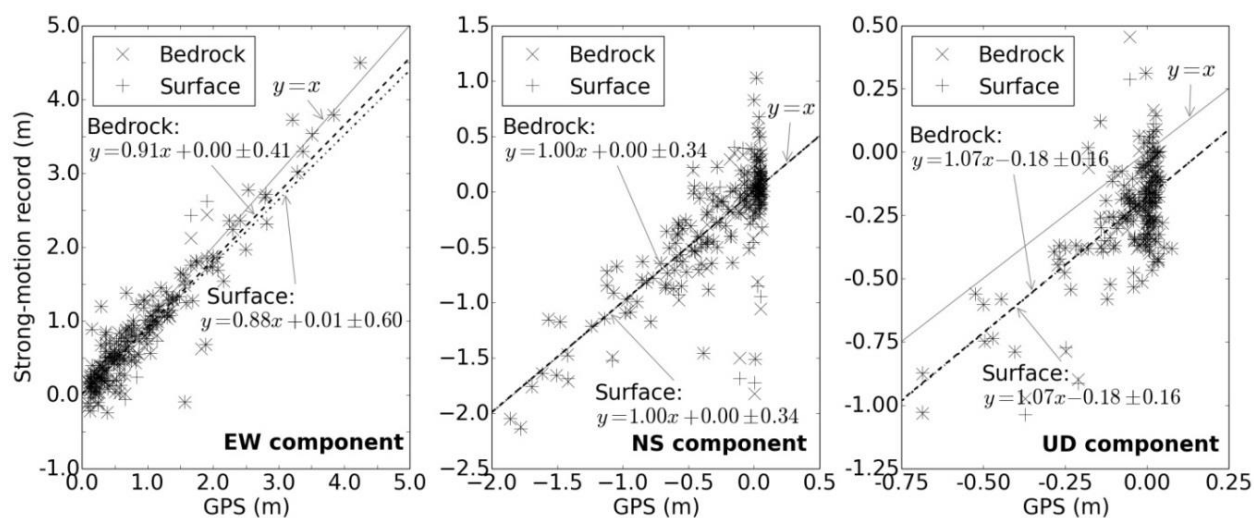


Figure 5.5 Comparison of permanent displacements obtained from the joint parameter search method and from the interpolation of GPS data. The symbols x and y are the abscissas and ordinates, respectively. The linear equations calculated from least-squared regression are expressed in meters.

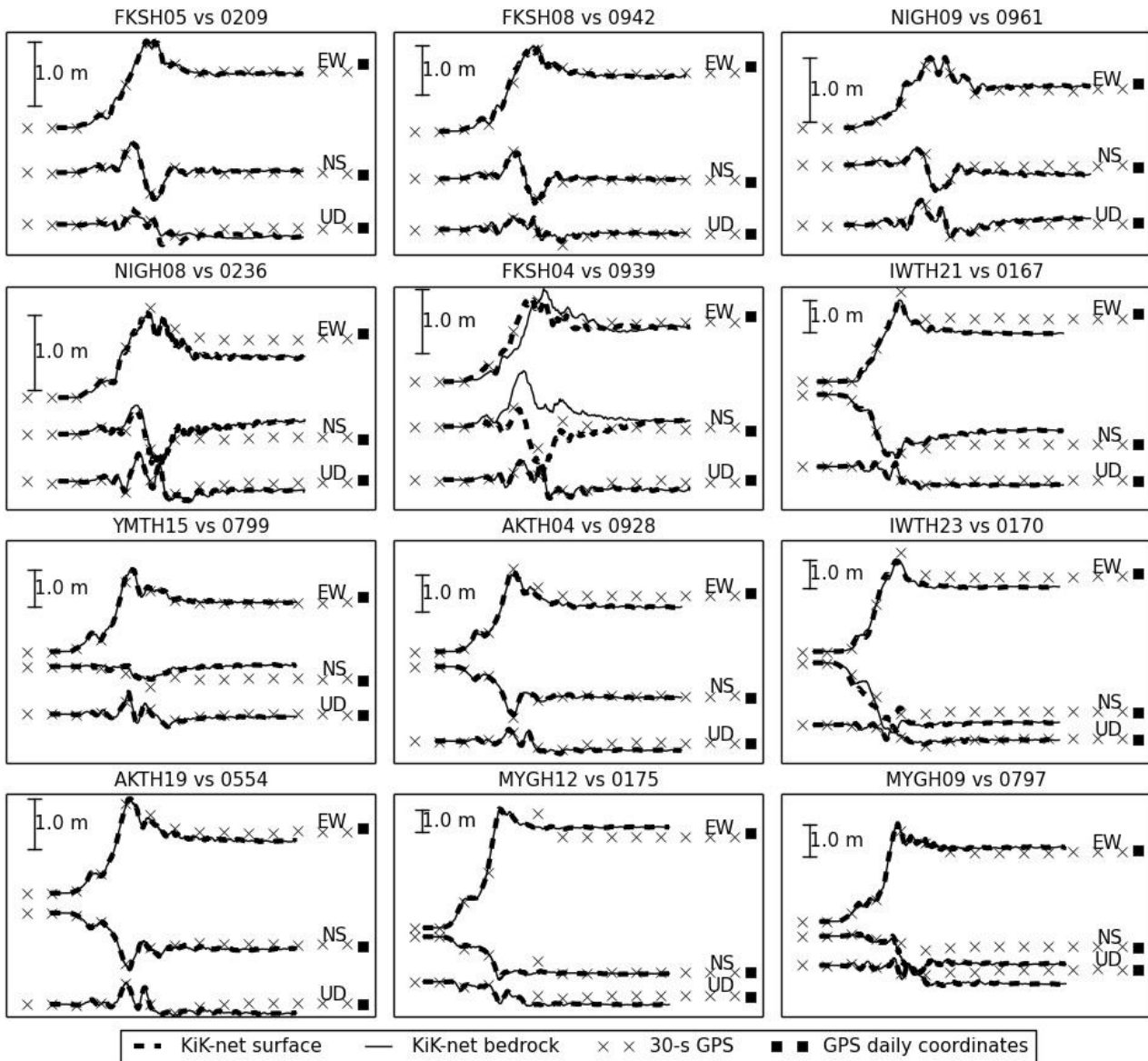


Figure 5.6 30-s GPS displacement (symbol x) and displacement time histories from the joint parameter search method at the borehole (solid line) and the surface (dashed line).

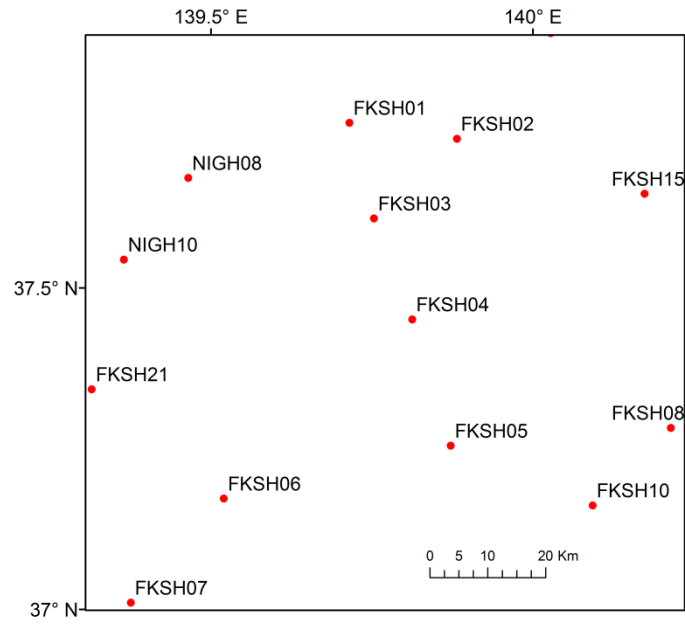


Figure 5.7 KiK-net FKSH04 station and stations nearby.

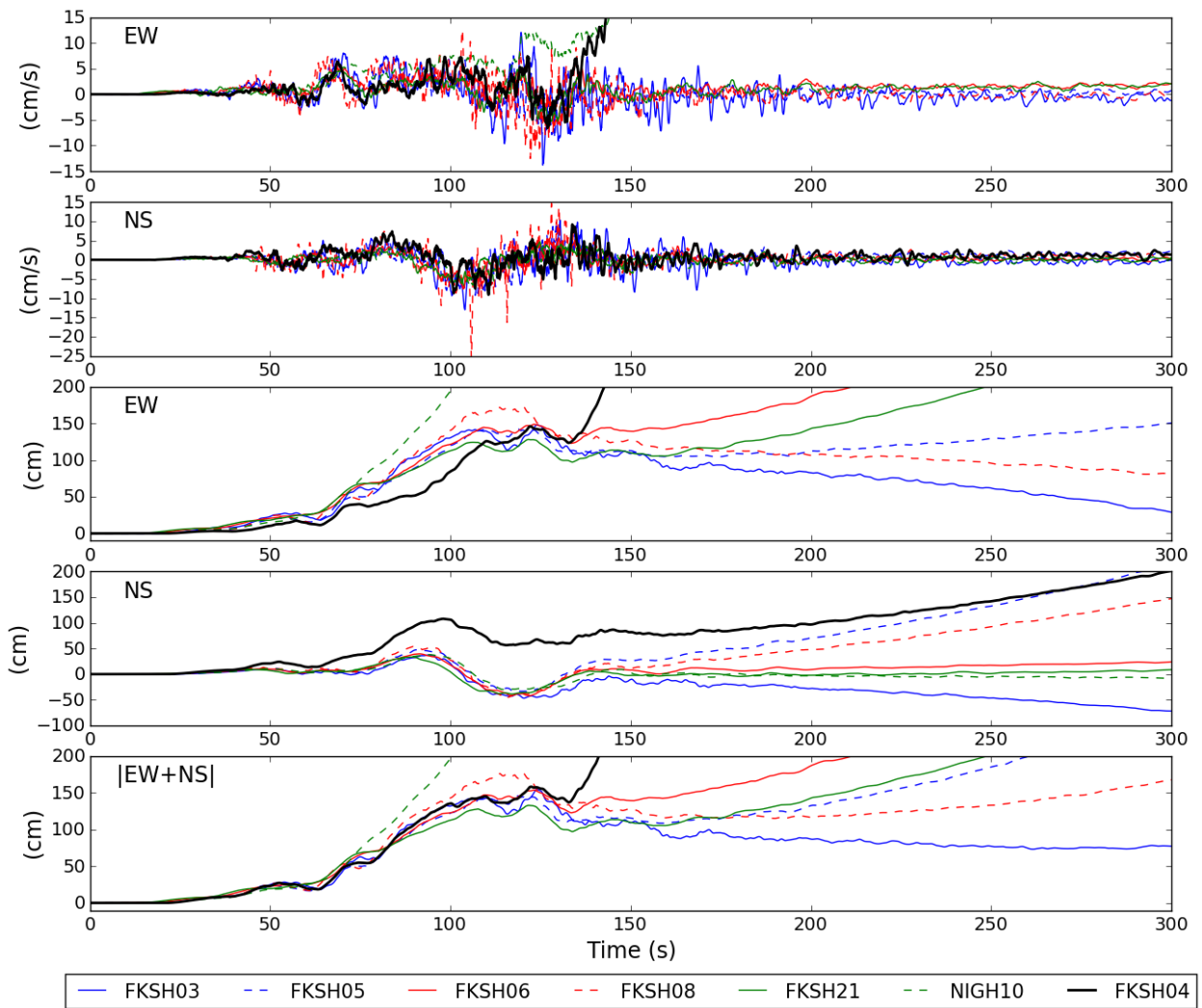


Figure 5.8 Uncorrected records of KiK-net station FKSH04 and stations nearby.

As observed in Figure 5.2, when the permanent displacement is greater than the transient wave, the results using only records at bedrock are slightly more accurate. However, in several cases when the permanent displacement is lower than the transient wave, our results are closer to that of GEONET. This tradeoff is reflected in the slope and standard deviation of the least-squares regression lines calculated from Wang's method (Figure 4.3) and our method (Figure 5.5), which are very close. Because the current methods can reproduce similar results as those using only records at the bedrock, it might seem that the proposed method does not provide any additional information related to permanent displacement distribution. However, the proposed method is useful in three aspects. First, we still estimate the baseline shift as two constant values: during the main shaking part and at the later part. This means that the only difference among the methods is the method of estimating the time parameters. Hence, we infer that a linear baseline shift is also sufficient for obtaining results using the records at the surface, and the poor results obtained by using the previous methods are not mainly because of nonlinear baseline shifts, as was suggested in the previous studies. Second, although the proposed method does not provide additional information on permanent displacement, the response time history at the surface obtained using our method can be useful in other fields (e.g. earthquake engineering). As an example, the velocity time history is required to extract multiple pulses from ground motion by using wavelet analysis (Lu and Panagiotou, 2014), which is of interest to researchers studying the structural response of tall structures. And the last but not least, we believe that, since Wang et al. (2011)'s method and our approach are of an empirical nature, having results from our method would be supportive.

5.4 Concluding remarks

A method to remove the effects of the baseline shift was developed by employing a joint parameter search for each KiK-net station with surface and borehole accelerometers. Using this method, a remarkable improvement was observed in the results for the records at the surface. However, our method has a limitation in that it requires the use of two accelerometers (at the bedrock and surface) deployed at the same site. The results of the joint parameter search method show that the time parameters obtained using previous methods can be improved and that the poor results at the surface are not mainly due to nonlinear baseline shifts.

Chapter 6

Assessment of GNSS Kinematic relative positioning for long baseline distance

6.1 Problem statement

The Global Navigation Satellite System (GNSS) has become an important technology with which to calculate the crustal deformation and displacement waves produced by earthquakes. In Japan, a dense GNSS network (GEONET) is available, with 1200 stations distributed uniformly throughout the country. Currently, relative positioning is one of the most precise GNSS positioning techniques, with a centimeter level of accuracy. However, this method requires two GNSS stations: a station where an estimation of displacement is to be determined and a station that remains stationary with a well-known position. To fulfill this requirement, the base station must be located far enough from the epicenter to assure that no displacement is produced. The performance of relative positioning depends on the distance between the receiver and the base stations, often referred to as the baseline. In this study, we evaluate this tradeoff by calculating the permanent displacement in the Geonet station 0266 during the November 22, 2014 Mw 6.2 Nagano earthquake several times with different base stations. Then, variations in the permanent displacement are evaluated in terms of the baseline. With several available GEONET stations to set as the base station, we study the relationship between the performance of displacement and the baseline.

The present investigation attempts to evaluate the feasibility of using RTK to estimate coseismic displacements in cases where the $|BL|$ ranges from 20 km to more than 1000 km. For this purpose, the November 22, 2014 inland earthquake in Nagano Prefecture, Japan is used as a case study because crustal deformation was observed in a narrow area.

6.2 Case study: Nagano earthquake

A Mw 6.7 earthquake occurred on November 22, 2014 in the northern part of Nagano Prefecture (Figure 6.1a), hereafter referred as the 2014 Nagano earthquake. The rupture process was at the NNE-WWS trending Kamashiro active fault (Hata et al., 2015). A large coseismic displacement was detected at the GEONET Hakuba (with code 0266) control station. Figure 6.1b shows the displacement calculated from the daily coordinates published by GSI. Displacements of 12.3 cm in the vertical direction and 28.4 cm in the horizontal direction (24.4 cm to the east and 14.6 cm to the south) were detected, which agree with the quick estimation published by GSI (12 cm and 29 cm for the vertical and lateral components).

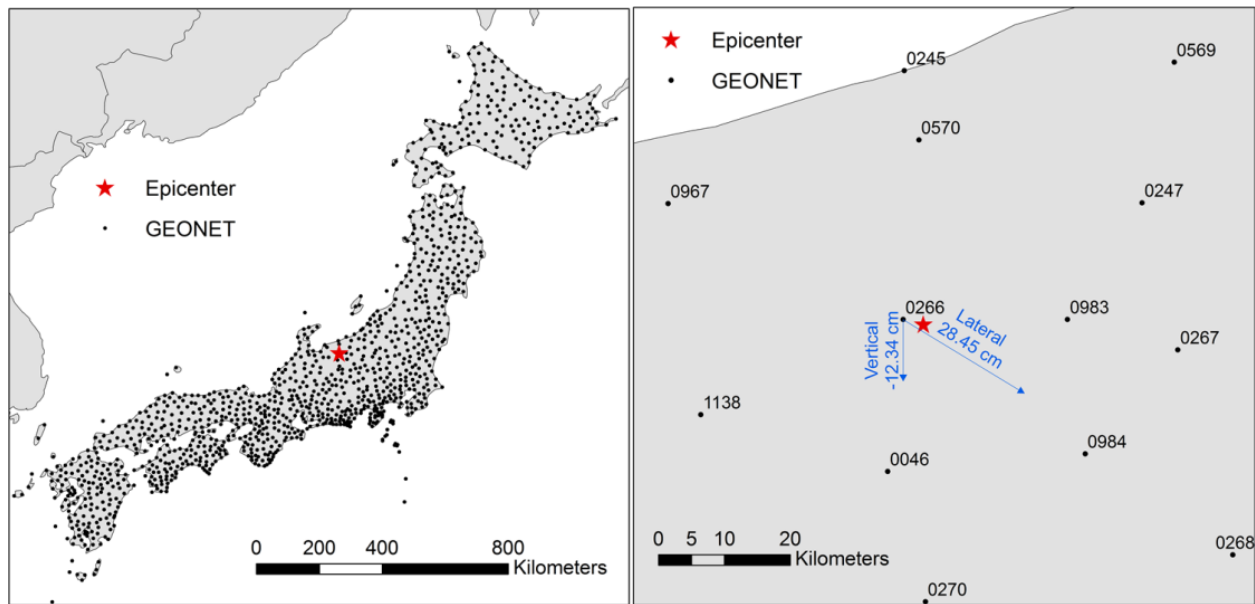


Figure 6.1 (a) Distribution of GEONET stations and epicenter of the Nagano earthquake. (b) Location of the 0266 GEONET station and the coseismic displacement during the Nagano earthquake.

Only the GEONET Hakuba (0266) station recorded a large displacement; the second largest displacement was recorded at station 0984 (see Figure 6.1b), with a lateral displacement of only 1.7 cm. The permanent displacement developed locally in the Nagano earthquake makes it suitable to evaluate the effect of the $|BL|$ in the performance of the RTK method using different pairs of GEONET control stations. For each pair, the rover station is fixed as the 0266 control station and the master station changes continuously, assuming no permanent displacement. A total of 1,220 pairs of GEONET control stations with the $|BL|$ ranging from 20 km to approximately 2,000 km was used for the evaluation.

6.3 Evaluation of accuracy of permanent ground displacement from kinematic relative positioning

Two configuration settings were chosen in this study. One is the conventional RTK (CRTK) method used for a short $|BL|$ (less than approximately 20 km), where a centimeter level of accuracy is guaranteed. Because this setting is designed for a short $|BL|$, atmospheric correction is not applied. The second configuration setting is the one currently used in the Japanese Tsunami EWS (Ohta et al., 2012), where the atmospheric correction and precise ephemerides are necessary. This second configuration is designed for long- $|BL|$ RTK (LRTK). A complete description of the method can be found in Takasu and Yasuda's paper (2010). The details of the configuration of each option are depicted in Table 3.1. In this study, the open source program package for GNSS positioning, RTKLIB (www.rtklib.com; last accessed on January 10, 2016), was used to process the data.

The RINEX data for 30 second intervals from each control station provided by the GSI server (<ftp://terras.gsi.go.jp/>; last accessed on January 19, 2016) were used in this research. The precise coordinates for the master stations were obtained from the daily coordinate product of November 21, 2014, which is one day before the Nagano earthquake. Because the method is intended to work in real-time for EWS, the ultra-

rapid product of the ephemerides, which is provided in near real-time by the IGS (<https://igsceb.jpl.nasa.gov/components/prods.html>; last accessed on January 19, 2016), is used.

Figure 6.4 shows the displacement time history obtained from RTK for the two configuration settings mentioned above. Fifteen minutes of record are depicted to show five minutes before and 10 minutes after the origin time of the earthquake, which was at UTC 13:08 according to the National Research Institute for Earth Science and Disaster Prevention (NIED) of Japan. As a reference to evaluate the results, the displacement obtained from the daily coordinate products is also depicted in Figure 6.4 (red line). The results have been separated according to the $|\text{BL}|$ magnitude into four groups: $|\text{BL}|$ less than 50 km (12 control stations), $|\text{BL}|$ between 50 km and 100 km (49 control stations), $|\text{BL}|$ between 100 km and 500 km (676 control stations), and $|\text{BL}|$ greater than 500 km (483 control stations). For each record, an average of the first 5 minutes of record was removed.

Table 3.1 Option settings for the two RTK methods

Option	Conventional	For long BL
Positioning mode	Kinematic	Kinematic
Frequencies	L1+L2	L1+L2
Receiver dynamics	OFF	OFF
Earth tides correction	OFF	ON
Elevation mask	10°	10°
Ionosphere correction	OFF	Estimate STEC
Troposphere correction	OFF	Estimate ZTD+Gradient
Satellite ephemeris	Broadcast	Precise
Ambiguity validation threshold	3.0	3.0
Min elevation to fix ambiguity	-	25
Min elevation to hold ambiguity	-	35
Code/Carrier-Phase error ratio	100	100
Carrier phase error	0.003+0.003/sin El m	0.003+0.003/sin El m
Process noise of vertical iono. delay	10 ⁻³ m/sqrt(s)	10 ⁻³ m/sqrt(s)
Process noise of ZTD	10 ⁻⁴ m/sqrt(s)	10 ⁻⁴ m/sqrt(s)
Satellite antenna model	IGS08.ATX	IGS08.ATX
Receiver antenna model	IGS08.ATX	IGS08.ATX

As expected, for the results using CRTK (Figure 6.4a), errors increase with increasing $|BL|$. Some records of the first group show a *cycle slip effect*, which means a reinitialization of the counter of the integer number of cycles of the signal that is caused by the signal lock. For a $|BL|$ less than 100 km, the displacement is easily depicted. However, the results from the 3rd and 4th groups show high distortions. However, in most of the records, these distortions show either increasing or decreasing trends in time, and with some effort, the coseismic displacement could be observed. These trends represent the systematic errors produced by the atmospheric effects. A problem arises of how to identify a coseismic displacement based on the displacement from the trend produced by the atmospheric effects. However, the shape of the coseismic displacement is a sudden action similar to a step or ramp function, whereas the effect of the atmosphere is a continuous smooth change of the coordinate in time. Moreover, if accelerometers are available, which is highly probable because accelerometers are ubiquitous in seismic prone areas in Japan, the time when the coseismic displacement started is known.

Figure 6.4b shows the displacement time histories using the LRTK method for long $|BL|$ lengths. Most of the systematic errors produced by the atmospheric effects have been significantly reduced. The cycle slip effect observed in the first group was almost eliminated. However, in the 2nd, 3rd and 4th groups, there are still some records that show high distortions. These records that show distortions without any trend depend on factors different from the atmospheric effects, such as a loss of signal. For instance, Figure 6.2 shows a case in which GEONET control station 1133 is selected as the master. There was a loss of signal of the GPS24 satellite when the initial part of the earthquake was coming. A closer look revealed that when the elevation angle of the GPS24 satellite reached 20°, the signal was blocked by a bamboo forest. Figure 6.3a and 6.3c show a contrast of the results with and without the signal of GPS24 using the CRTK method. Because the GPS24 has been removed, the coseismic displacement and the systematic error caused by the atmosphere could be observed. The loss of signal did not significantly affect the result when the LRTK method was applied (Figure 6.3b); however, an improvement was observed when the GPS24 signal was not considered in the process (Figure 6.3d).

Our main purpose is to evaluate the coseismic displacement rather than the accuracy of the coordinates calculated by the RTK. Thus, the displacement was estimated as the difference between the average of the first three records after coseismic displacement and the average of the three records before coseismic displacement. Figure 6.5 shows the coseismic displacements calculated from RTK for different the $|BL|$ lengths, shown as black dots. In the figure, the horizontal blue dashed line represents the coseismic displacement estimated from the daily coordinates. There is a clear decrease of the accuracy in the estimation of the displacement when the BL length increases in the results of CRTK (Figure 6.5a). The displacement could be estimated with a gradual increase of error until approximately 800 km, and after that, a significant increase of errors is observed. However, there is a slight increase of error when LRTK is used, even for BL greater than 1,000 km.

For a closer look at the error, the difference between the coseismic displacement from the daily coordinates and from RTK is shown in Figure 6.6 as green dots. For a clear visualization on the error trend, a window averaging 50 km length is shown as red lines. Figure 6.6 also shows the average window plus two times its standard deviation (blue lines). The peaks observed in the red and blue lines are due to spurious

results, such as the case shown in Figure 6.2. If the peaks observed in the blue lines are neglected, most of the errors are less than 10 cm for LRTK. For CRTK, as expected, the error increases with the increase in $|BL|$. For a $|BL|$ less than 500 km, the errors are less than 20 cm but increase to 1 m when the $|BL|$ is approximately 1,500 km.

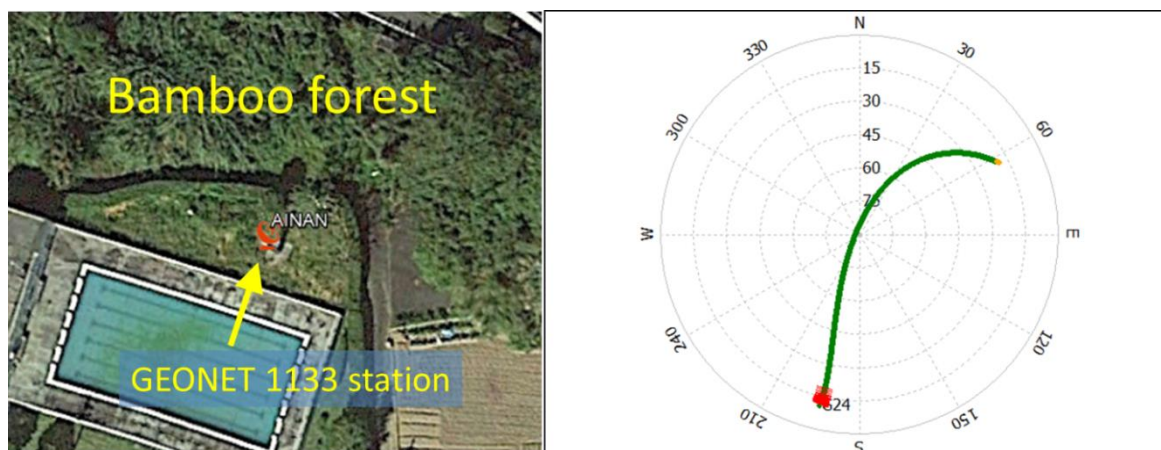


Figure 6.2 Left: Location of GEONET station 1133; Right: Skyplot of the GPS satellite 24.

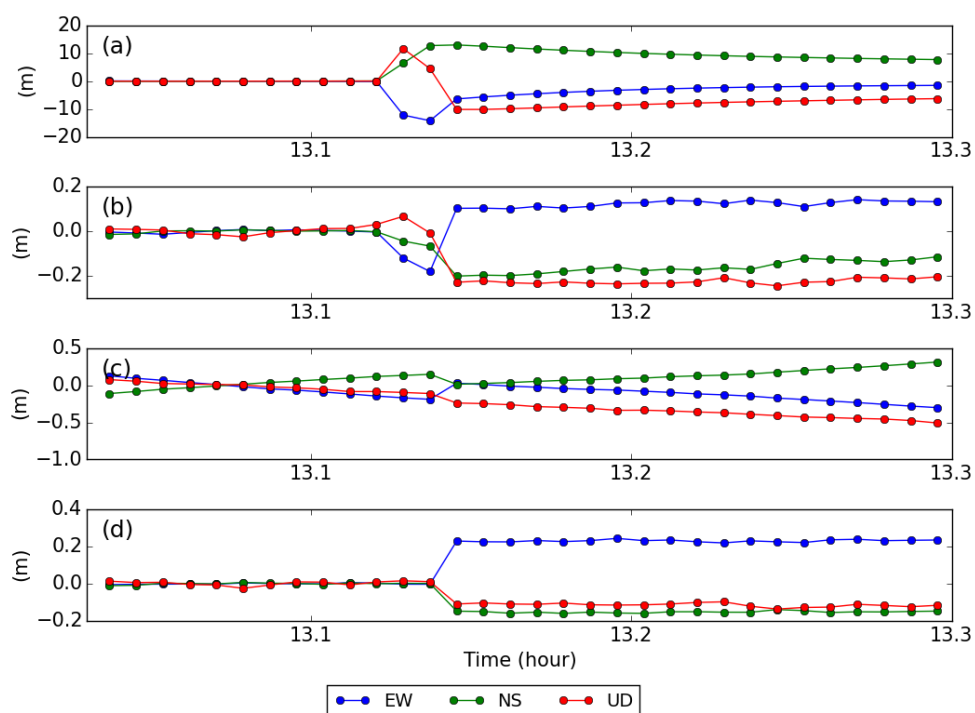


Figure 6.3 Displacement time histories at control station 0266 from the RTK method using station 1133 as the master station. (a) CRTK considering the GPS24 signal; (b) LRTK considering the GPS24 signal; (c) CRTK without the GPS24 signal; (d) LRTK without the GPS24 signal.

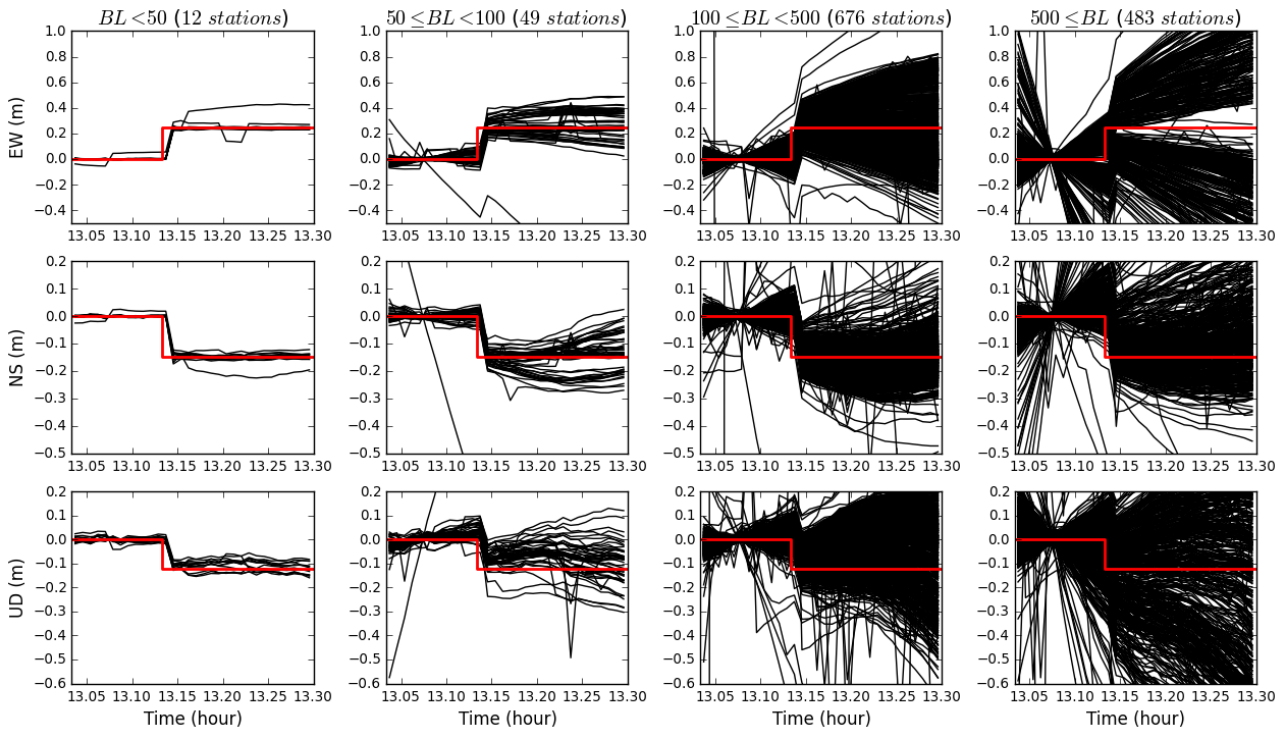


Figure 6.4a Displacement time histories obtained from CRTK

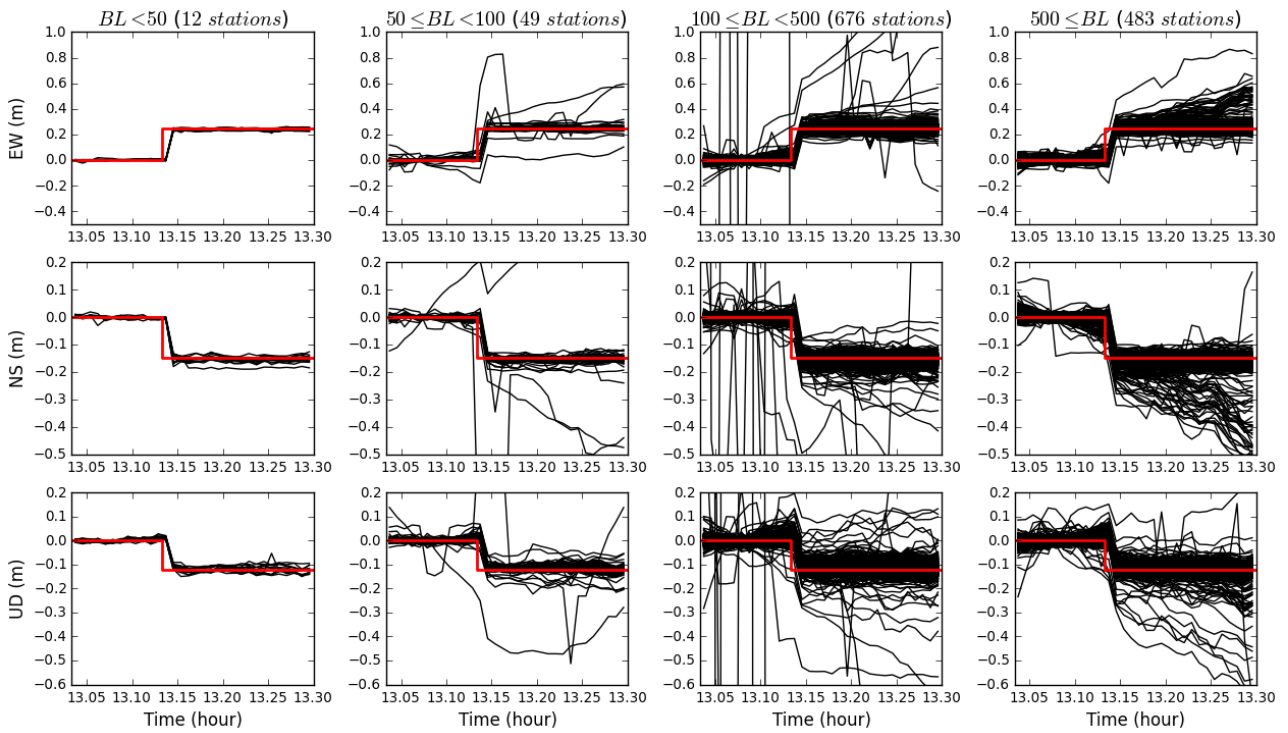


Figure 6.4b Displacement time histories obtained from LRTK

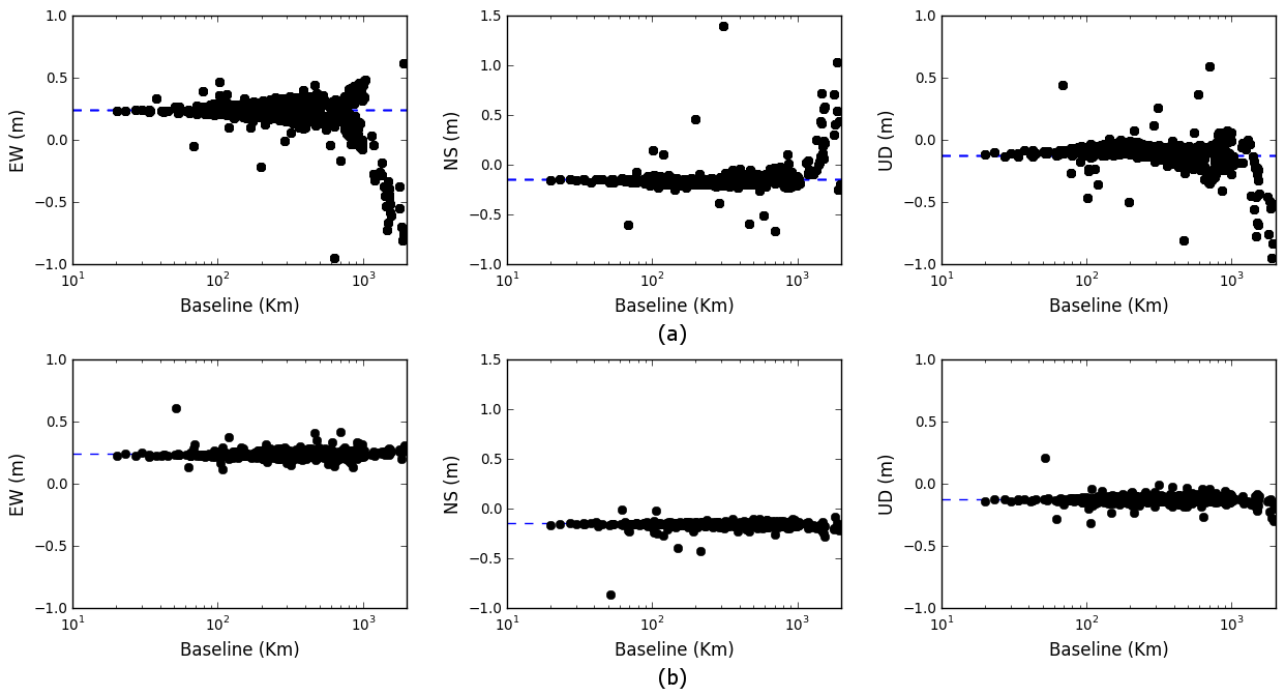


Figure 6.5 Calculated relative displacement respect to the $|BL|$ obtained by (a) CRTK and (b) LRTK.

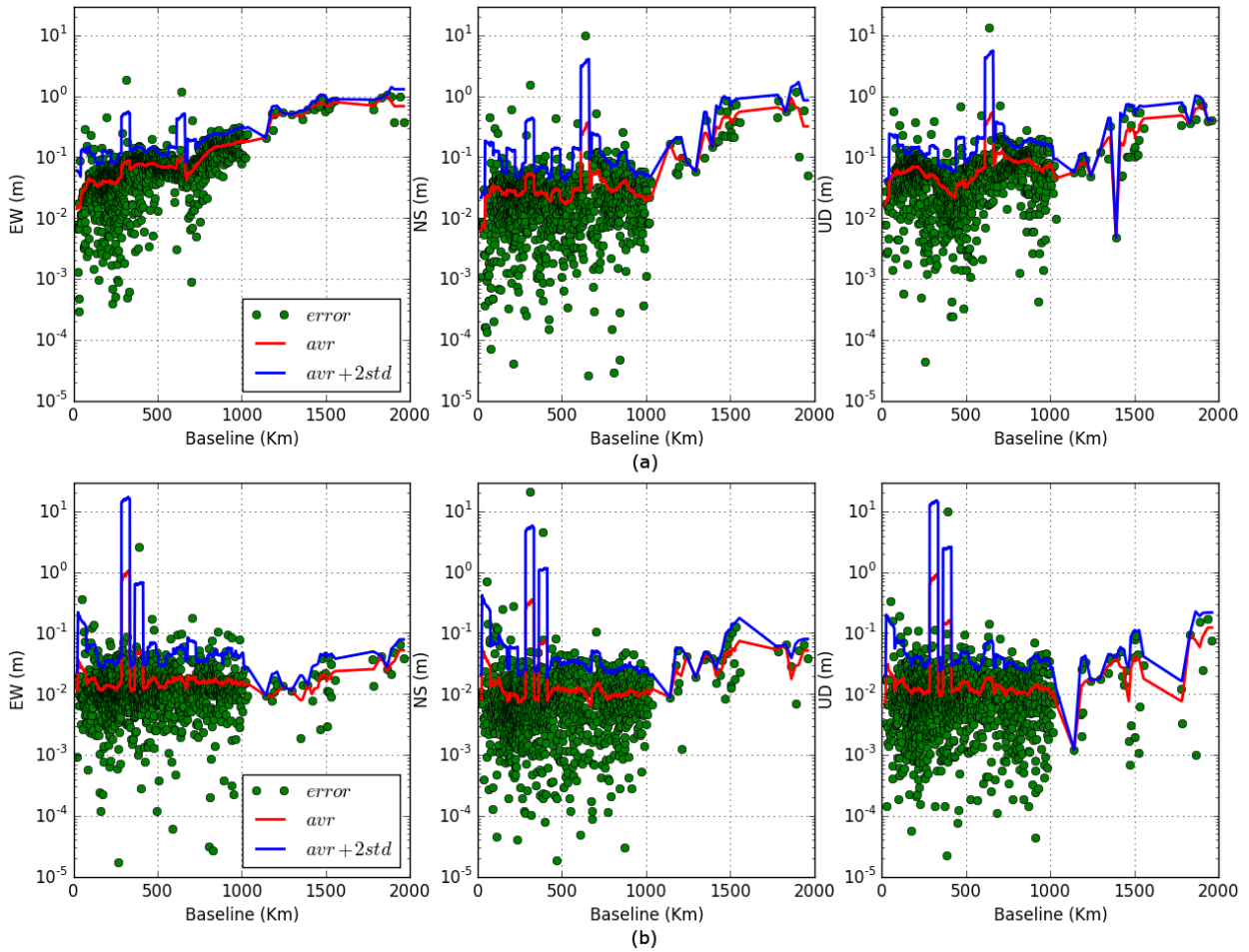


Figure 6.6 Difference between the coseismic displacement calculated from the RTK and from the daily coordinates for (a) CRTK and (b) LRTK.

6.4 Concluding remarks

In this chapter, we studied the performance of Real-Time Kinematic (RTK) positioning for different baseline distances to assess coseismic deformation. For this purpose, the coseismic displacement recorded at one GNSS station during the November 22, 2014 Nagano earthquake was used. A total of 1,220 cases with BL lengths ranging from 20 km to approximately 2,000 km were evaluated. For each case, two setting processes were applied: the conventional RTK (CRTK), which is designed to achieve centimeter-level accuracy for BL lengths less than 20 km, and an RTK method designed for long baselines (LRTK).

Systematic errors appeared in the displacement time history for CRTK, resulting in a continuous and smooth change in the coordinates. The rate of those changes increases as the baseline increases. However, because the coseismic displacement occurs suddenly, it could be still observed in most cases. The systematic errors were almost removed when LRTK was used. Moreover, records with large distortions were still observed. These errors were attributed to factors other than the atmospheric effects.

For the studied case, the Nagano earthquake, the coseismic displacement estimated by the LRTK has errors less than 10 cm. However, the results from the CRTK have increasing errors as the baseline increases. These errors are less than approximately 20 cm for baselines less than 500 km and increase to one meter when the baseline reaches approximately 1,500 km. For the records with the shortest baseline, by comparing the blue lines of Figure 6.6 (the averaging window plus two times the standard deviation), CRTK achieves better results than LRTK. One reason for the better results is that the window averaging is affected by the large error caused by factors other than the baseline length; another reason is that for short baselines, using only double differentiation, more accurate atmospheric effects can be obtained than by estimating the atmospheric effects. The atmospheric effects can then be removed because the atmospheric conditions in both control stations (rover and master) are well-correlated when the baseline is short.

Chapter 7

Coseismic displacement in the 2016 Kumamoto earthquake from LIDAR data

7.1 Introduction

On April 14, 2016 at 21:26 an M_w 6.2 earthquake occurred in Kumamoto prefecture, Japan. The epicenter (32.7°N , 130.8°E) was located at the end of the Hinagu fault. About 28 hours later (April 16, 2016 at 01:25), another earthquake of M_w 7.0 occurred in the Futagawa fault. Thus the first event was designated as the "foreshock" and the second one as the "mainshock". The both events were located in the suburban area of Kumamoto city with 735 thousand population. Therefore, extensive damage such as human loss, collapse of buildings and bridges, landslides, damage to soils and foundations, and damage of historical structures occurred.

Light detection and ranging (Lidar) has many applications in earthquake engineering, such as surface deformation (Muller and Arding, 2007; Nissen et al., 2012; Duffy et al., 2013; Oskin et al., 2012), landslide detection (Jaboyedoff et al., 2012), and extraction of building features (Vu et al., 2003; Vu et al., 2009). Airborne Lidar technology is an integrated system consisting of a Global Navigation Satellite System (GNSS), an Inertial Navigation System (INS) and a laser scanner that uses pulses of laser light towards the ground and records the return time to calculate the distance between the sensor and the ground surface (Lillesand et al., 2004).

This paper shows an estimation of the coseismic displacement due to the mainshock of the Kumamoto earthquake calculated from the Digital Surface Models (DSMs) obtained from airborne Lidar flights by the same airplane, instrument and pilot. In this case study, a pair of DSMs is available for Mashiki town including the causative Futagawa fault: one just after the foreshock (on April 15) and another after the mainshock (April 23). The obtained results will be compared with the permanent ground displacements estimated from acceleration records obtained by the KiK-net, Kumamoto prefecture's network, and a temporary observation system (Hata et al. 2016).

7.2 Study area and data description

On April 15, 2016, one day after the big foreshock, a Lidar DSM was collected by Asia Air Survey Co., Ltd., in order to record the surface rupture and building damage produced by the earthquake. The survey generated a DSM with average point-density of 1.5~2 points/m². Furthermore, due to the unexpected mainshock of M_w 7.0 occurred on April 16, a second mission to acquire Lidar data was sent on April 23, which was able to generate a DSM with average point-density of 3~4 points/m². After the rasterization of the raw point clouds, the DSMs have a data spacing of 50 cm and were registered in the Japan Plane Rectangular Coordinate System. This data set is one of the few cases in which pre- and post-event DSMs are available with the same airplane, instrument, and pilot (Air Survey Co., Ltd. 2016). For the sake of brevity, we will refer the DSM collected on April 15 and April 23 as the pre-event DSM and post-event DSM, respectively.

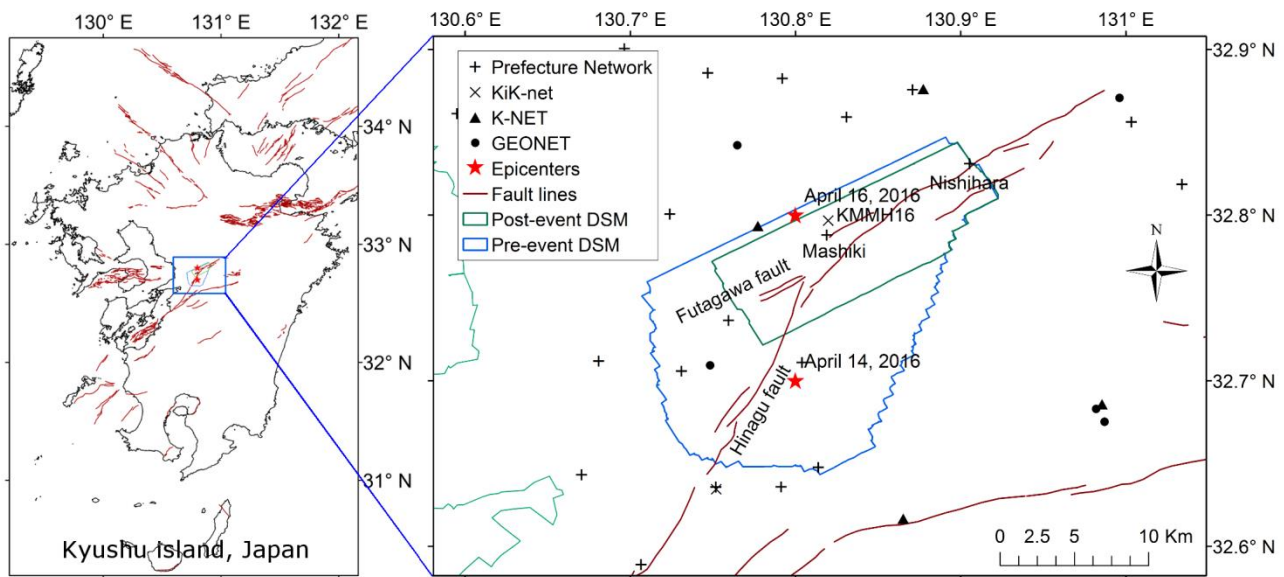


Figure 7.1 Map of the near-source area of the 2016 Kumamoto earthquake, showing the pre-event DSM (blue polygon), the post-event DSM (green polygon), the distribution of the GNSS and seismic stations, active fault lines in Japan, and epicenters (M_w 6.2 April 14, 2016; M_w 7.0 April 16, 2016).

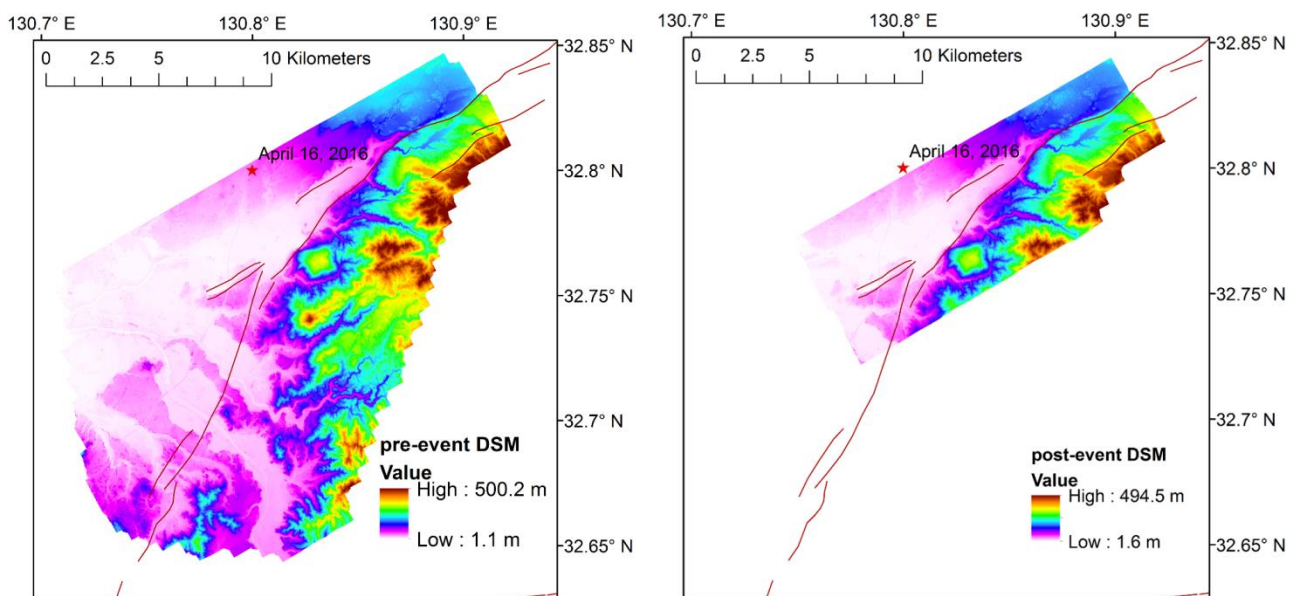


Figure 7.2 Digital surface models collected in April 15, 2016 (pre-event DSM) and April 23, 2016 (post-event DSM)

Figure 7.1 shows the extension of the pre- and post-event DSMs, where the pre-event DSM extends for a bigger area than the post-event DSM does. The common area of the both DSMs covers most parts of Mashiki town, and parts of Kashima town, Mifune town, and Nishihara village. The whole common area is composed of residential areas, agricultural fields, forests and includes a part of the Futugawa fault that caused the mainshock of the Kumamoto earthquake.

The Kumamoto earthquake occurred in a well-instrumented area, with several GNSS instruments that belong to GEONET (Sagiya 2005) and strong-motion instruments that belong to KiK-net, K-NET (Aoi

2004) and the Kumamoto prefecture's network (Figure 7.1). GEONET consists of about 1,300 GNSS control stations that cover Japan's territory with an average interval of 20 km. K-NET consists of more than 1,000 strong-motion accelerometers distributed every 20 km covering Japan as well. KiK-net consists of approximately 700 stations, each has a pair of accelerometers located on the ground surface and in a borehole at the bedrock. The Kumamoto prefecture's network consists of strong-motion accelerometers placed at public building sites.

Several evidences of coseismic displacements along the Futagawa fault line during the Kumamoto earthquake have been observed as surface ruptures, such as in agriculture fields, river channels, and roads (Figure 7.3). Those visual evidences were generated because of the opposite displacements (right-lateral strike-slips) between the both sides of the fault. A more clear evidence of coseismic displacements is a comparison of the pre-event DSM with the post-event DSM. Figure 7.4 shows an overlapping of the two DSMs where the pre- and post-event DSMs are represented by a cyan- and red-colors, respectively. The gray-colored pixels represent location with the same elevation for the both pre- and post-event DSMs, whereas red- or cyan-colored pixels represent the locations where the elevation in the post-event DSM or the pre-event DSM is higher. Based on this approach, the colors around the sides of houses depicted in Figure 7.4 show that a coseismic displacement occurred to the northeast direction.



Figure 7.3 Examples of coseismic displacement produced by the 2016 Kumamoto earthquake. Puddy field (a), river channel (b), and road crossing (c) in Kamijin and Shimojin districts of Mashiki town observed on April 17, 2016; crop field (d) in Dozono district of Mashiki town observed on June 7, 2016.

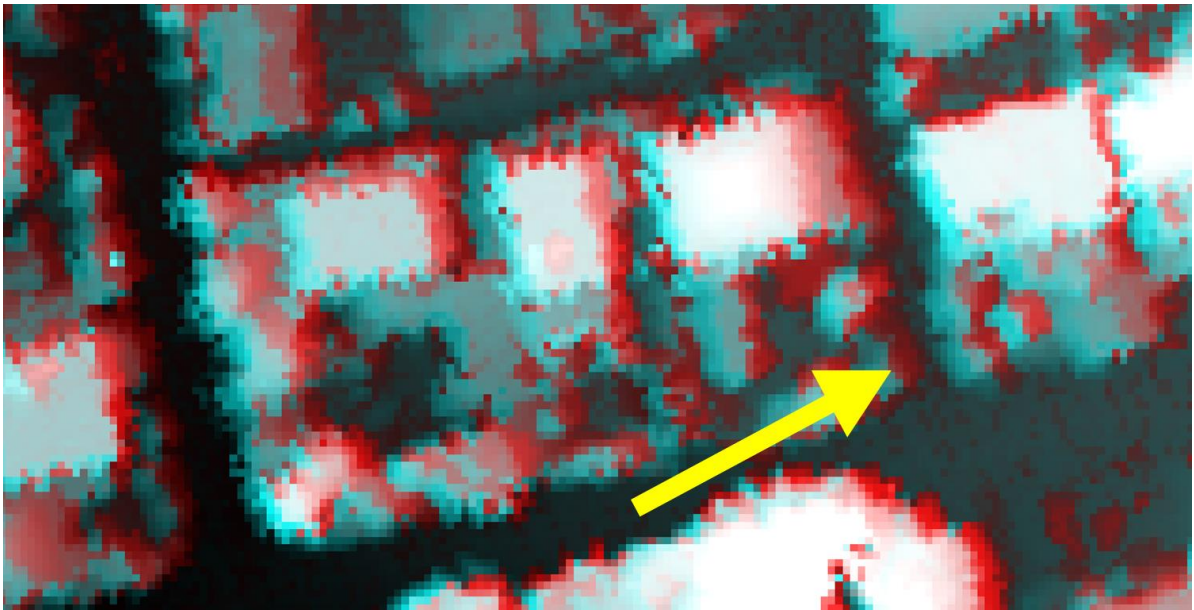


Figure 7.4 Color composite of the post-event DSM (red) and the pre-event DSM (cyan) for an urban block near Mashiki town office (Prefecture network), showing an evidence of coseismic displacement. The yellow arrow depicts the direction of the coseismic displacement.

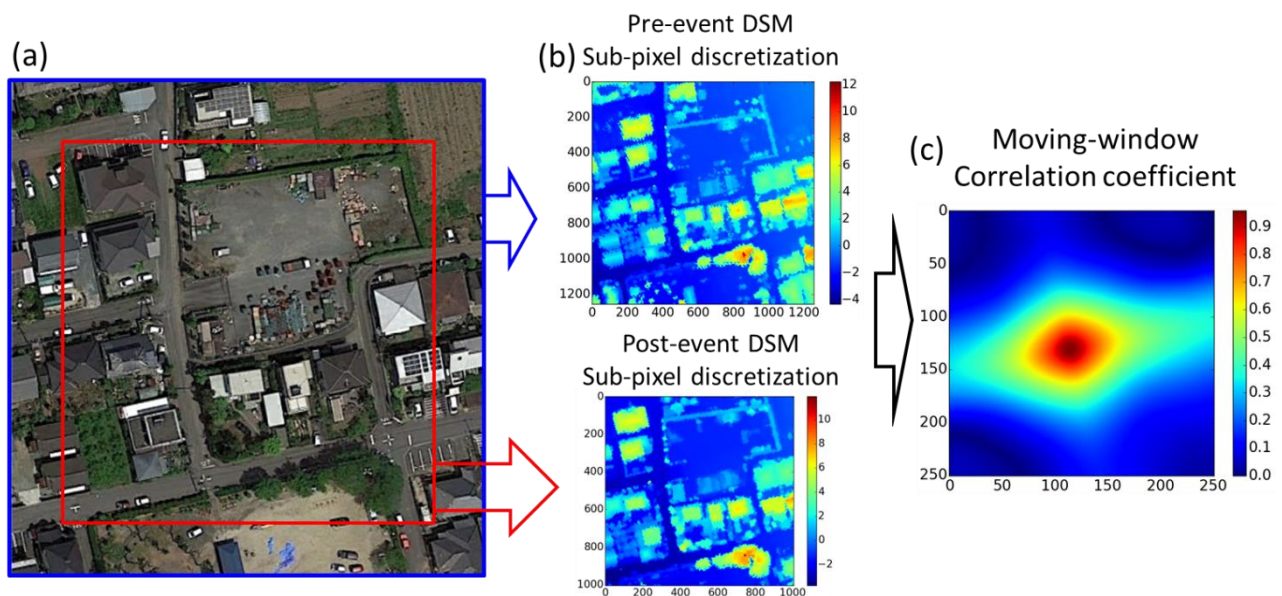


Figure 7.5 Flowchart of the maximum correlation search algorithm. Selection of the pre-event DSM (blue) and post-event DSM (red) windows (a), sub-pixel discretization of the DSMs (b), and calculation of correlation coefficient by moving the post-event DSM's window over the pre-event one (c).

7.3 Methodology

To calculate the horizontal component of the coseismic displacement distribution in space, a maximum correlation search algorithm was introduced using a moving window of the post-event DSM within the surrounded area of the pre-event DSM. The method is based on the fact that the both pre- and post-event DSM covers the same objects, such as houses, which make possible to use the spatial cross-correlation

between the both DSMs. The pixel shift necessary to match the pre-event DSM with the post-event one is assumed to be the coseismic displacement. However, the coseismic displacement is variable in space and have to be calculated using sub-areas, which we term ‘windows’. Figure 7.5 shows a scheme of the approach. First, we take a square sub-area of the post-event DSM and a bigger sub-area of the pre-event DSM with both having the same coordinate of the pixel located at the center (Figure 7.5a). Afterwards, we reduce the pixel size using a cubic interpolation method (Figure 7.5b) and the post-event window is moved across the pre-event window and the cross-correlation coefficient is calculated at a time (Figure 7.5c). Then, from the calculation result, the location of the pixel at the largest correlation value is considered as the coseismic displacement. The similar cross-correlation approach was employed for optical satellite images in matching vehicle locations (Liu et al., 2011) and for SAR intensity data in matching building locations (Liu et al., 2013). Then, the horizontal component of the coseismic displacement was applied to the post-event DSM to cancel it and then the vertical displacement between the two DSMs was calculated. It is worth to mention that the cross-correlation was chosen among other candidates, such as a least-squared difference or convolution, mainly because the peak value was located in a narrower area.

It is not necessary to calculate the correlation for all the locations because it requires unnecessary computational efforts. A better procedure is to move the post-event window to the direction in which the cross-correlation is increasing faster until the peak is reached. This approach, well known as the steepest method, is applied to calculate the coseismic displacement for all the study area. Thus, the approach requires to define only the post-event window size and the rest is done automatically. However, the selection of the post-event window size is crucial because it should be large enough to include several objects. For instance, if a post-event window of $1.5 \times 1.5 \text{ m}^2$ (3×3 pixels) is chosen, there will not be a peak value in the cross correlation when the window is located in the middle of a flat building roof or a big bare land. Therefore, it is recommendable to define a window size that can include some buildings or different topography; however, keep in mind that the bigger the window size, the lower the resolution of the coseismic displacement’s spatial variation.

The code of the implementation was written in Python, an open-source language programming, in order to use the large collection of scientific open-source modules included. Numpy, the numerical array-programming module was used to calculate the cross-correlation. Open-CV (Open Source Computer Vision Library) was used to reduce the pixel resolution using the cubic interpolation method. GDAL (Geospatial Data Abstraction Library) was used to georeferenciate all the input and outputs

7.4 Results

Using the methodology explained above, the coseismic displacements in all the common area of the pre- and post-event DSMs, which is approximately 80 km^2 , were estimated. After testing several window sizes, the window of $100 \times 100 \text{ m}^2$ was selected because it was the smallest size that showed less level of noise. The pixel resolution of 50 cm was reduced to 10 cm using a cubic interpolation. Figure 7.6a shows the east-west component of the coseismic displacement, which shows a certain level of noise due to mainly the fact that some object are not exactly similar after the earthquake. Several buildings collapsed by the main shock and landslide also occurred. Besides, the post-event DSM contains objects that were not presented in the pre-event DSM, such as the shelters with vehicles and tents. However, the general trend of spatial variation of

the coseismic displacement could be depicted well. Therefore, a median filter with a window-size of 5 x 5 was introduced to remove the pixels that do not match the general trend.

The results for the final coseismic displacement are displayed in Figure 7.7. The black arrows indicate the horizontal component and the color shading indicates the vertical displacement. Although the output provided coseismic displacements in a 100-m grid, the black arrows show only displacement every 500 m in order to visualize better the orientation of the coseismic displacement. The change of direction of the coseismic displacement, in both the horizontal and vertical components, delineates the Futugawa fault line which is consistent with the surveyed active faults in Japan (Geological Survey Institute of Japan, 2016). The observed coseismic displacement shows eastward movements of up to 2.0 m in the northern area and 1.2 m in the southern area of the fault line. The legend of the vertical displacement shows a vertical displacement of up to -3 m; however, this value represent a narrow area where a landslide occurred.

A closer look of the general trend shows that a subsidence of up to 2 m occurred in the northern area and an uplift of up to 0.7 m in the southern area. Our results are consistent with the coseismic displacement estimated from SAR interferometry using ALOS-2 PALSAR-2 imagery (Geospatial Information Authority of Japan, 2016). Figure 7.8 shows the coseismic displacement profile along eight dashed lines placed uniformly along the Futugawa fault (Figure 7.7). The change of direction in all the components is located almost in the same location of the surveyed Futugawa fault line. However, the change of sign occurs gradually because the applied window contained the points from the both sides of the fault line and consequently produced small coseismic displacements. Although the main deformation was produced by the slip of the main Futugawa fault line, the profiles GH and IJ show smaller slips produced by the secondary Futugawa fault line.

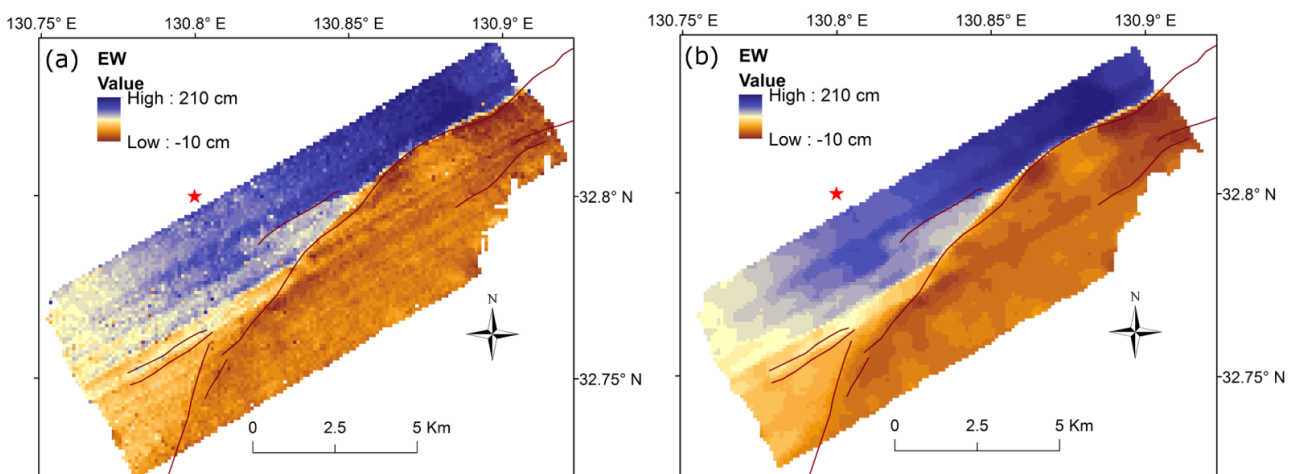


Figure 7.6 East-west horizontal displacement obtained from the cross-correlation matching search (a) and those generated after applying the median filter of 5 x 5 (b).

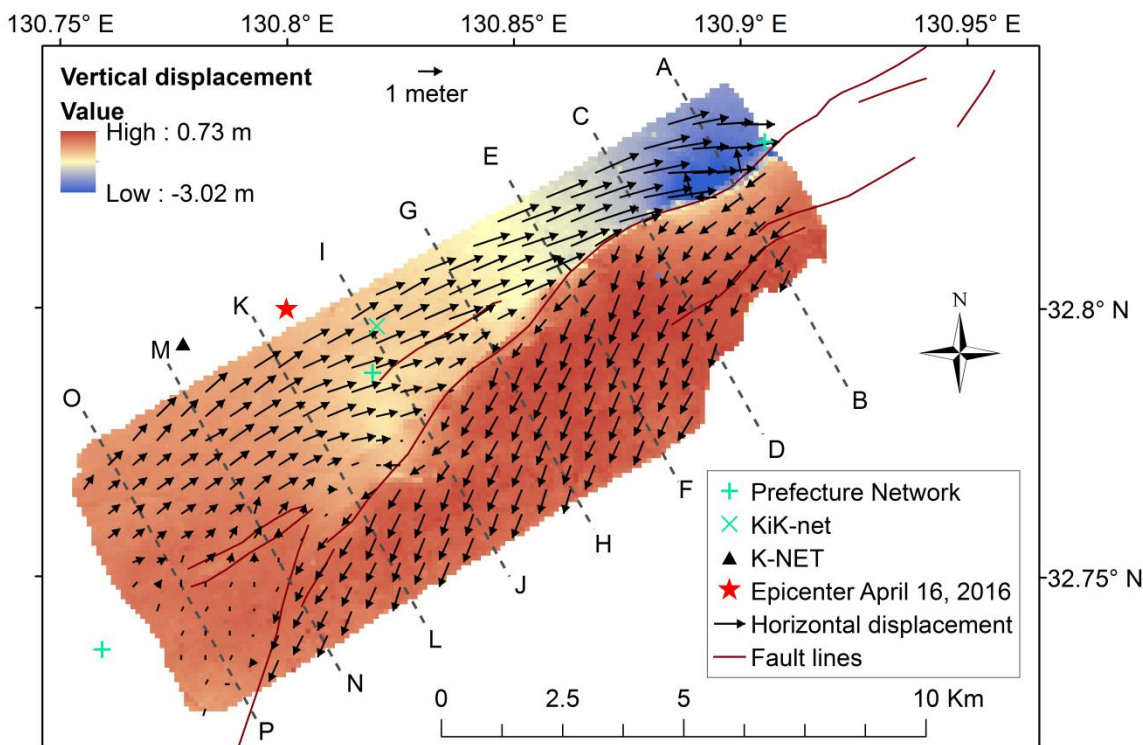


Figure 7.7 Estimated three-dimensional coseismic displacement produced by the mainshock of the 2016 Kumamoto earthquake. The three components were smoothed by the 5 x 5 median filter. The arrows show the amplitude and direction of the horizontal displacements at 500 m grid points.

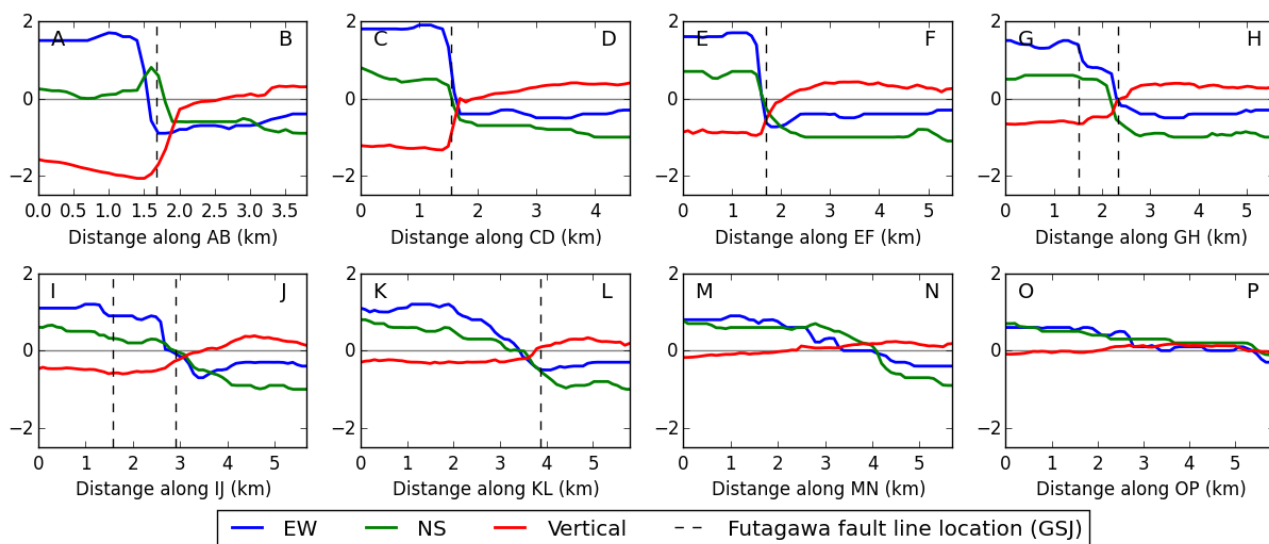


Figure 7.8 The estimated three-dimensional coseismic displacements along the eight profile lines in Figure 7.7. Vertical break lines show the location of the known main Futagawa fault line by the Geological Survey Institute of Japan.

7.5 Validation of results

This section tries to contrast our result with the coseismic displacements calculated from other sources of information. Currently, GNSS technology is used to monitor crustal deformation within a centimeter level of accuracy. Unfortunately, there are no GEONET stations within the study area. However, there are three strong-motion instrument that can be used to compare our results: two strong-motion station in the Mashiki town, one belongs to KiK-net and the other to the Kumamoto prefecture network, and the third strong-motion station of the prefecture network is located in the Nishihara village. Furthermore, K-NET Kumamoto station is located 1 km from the closest point of the study area. Digital acceleration records obtained from these four stations could be used to estimate the coseismic displacement caused by the mainshock.

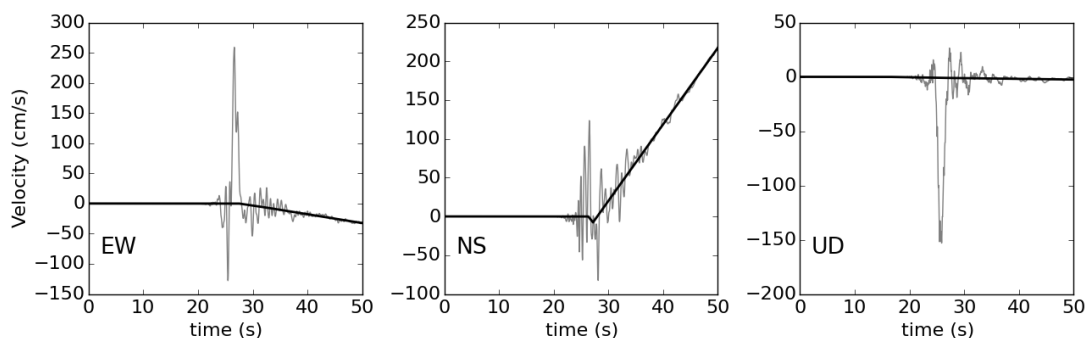


Figure 7.9 Example of baseline correction procedure applied to the Nishihara seismic station. The trend of the original velocity records was modelled by two straight lines in the Wang et al.'s method.

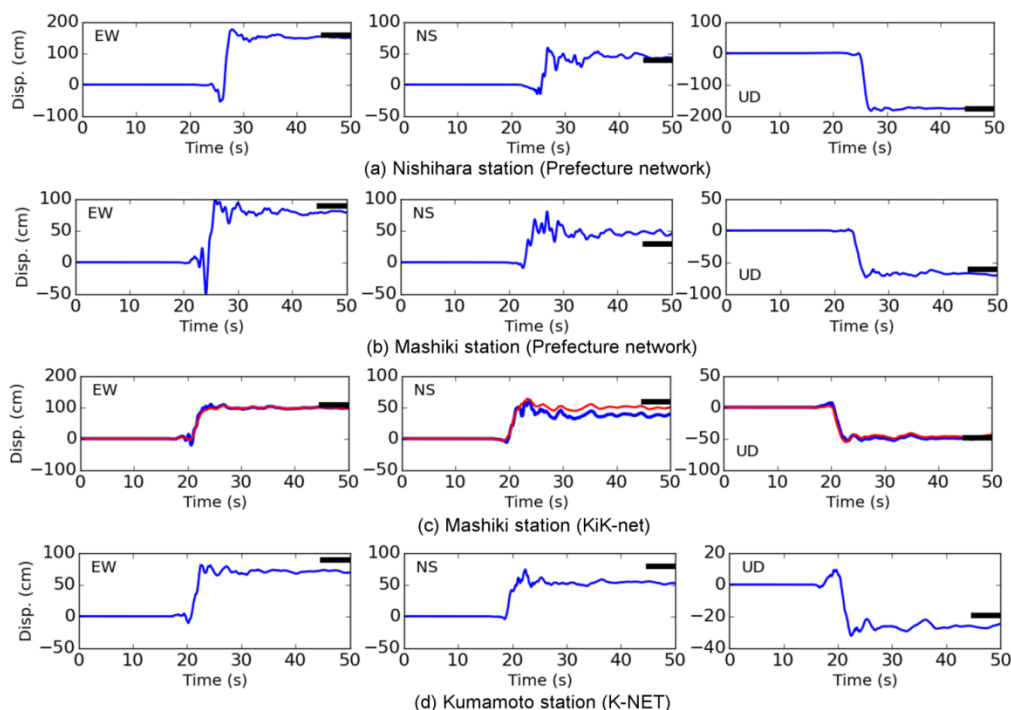


Figure 7.10 Comparison of three-dimensional coseismic displacements obtained from the Lidar DSMs (thick black line) with those obtained from the acceleration records at Nishihara prefecture-network station (a), Mashiki prefecture-network station (b), Mashiki KiK-net station (c), and Kumamoto K-NET station (d). Red lines in Mashiki KiK-net station show displacements at the bedrock (GL -252 m). Kumamoto K-NET station is located in 2 km from the nearest Lidar DSM point.

Displacement time history could be calculated precisely if the six components, three translational and three rotational, are recorded (Graizer, 2010). However, this is often estimated by a double integration in time of the translational components only. In most cases, it is necessary to perform a baseline correction before estimating the correct displacement time history because the baseline is shifted due to several factors such as ground rotation and rocking movements of the instrument. Since the source of errors and the rotation components cannot be quantified so far, empirical methods have been made in the past to reduce the effect of the baseline shift and retrieve a reliable displacement time history (Wu and Wu, 2007, Wang et al., 2011, Moya et al., 2016).

The method proposed by Wang et al. (2011) were applied on the acceleration records from the four strong-motion stations mentioned above. The baseline correction procedure estimates two linear segments from the uncorrected velocity time history. For instance, Figure 7.9 shows the baseline correction estimated from the uncorrected velocity of the Nishihara station. The two linear segments are calculated from an iterative procedure so that the corrected displacement time history takes the shape of a step function. Figure 7.10 shows the coseismic displacements obtained from the strong-motion records, compared with the results calculated from the DSMs. From the comparison, we can observe that the coseismic displacement derived from the DSMs are consistent with that obtained from the strong-motion records. For the case of the K-NET Kumamoto station, the results are compared with the closest result obtained from the DSM, which is approximately 1 km. There were two accelerometers at the KiK-net Mashiki station, one on the ground surface and another in the borehole (-255 m below the surface). Although the permanent displacements were calculated independently, the both results were very similar with the results from the Lidar data. This fact supports the validity of the Wang et al.'s method and the accuracy of the Lidar DSMs' result.

7.6 Conclusions

The coseismic displacement produced during the mainshock of the 2016 M_w 7.1 Kumamoto earthquake using two DSMs collected by Lidar flights before and after the 16 April mainshock. The common area of the DSMs covers about 80 km² including the Mashiki town section of the known Futagawa fault line. The maximum cross-correlation was used with a window matching technique between the two DSMs to calculate the coseismic displacement. A coseismic displacement of up to 2 m and a subsidence of up to 2 m were observed in the study area. These values are the largest coseismic displacements produced in the Kumamoto earthquake, which were not able to record at any GEONET stations. The results showed good agreement with the permanent displacement calculated from strong-motion records and with the Futagawa fault line published by the Geological Survey Institute of Japan.

7.7 Data and Resources

The DSMs were provided by the Asia Air Survey Co. Ltd. (<http://www.ajiko.co.jp/en/blog/y2016/id572751JWX/>, last accessed August 2016). Strong motion data collected from KiK-net and K-NET can be accessed at <http://www.kyoshin.bosai.go.jp/> (last accessed August 2016) and strong-motion data from the Kumamoto prefecture's network at http://www.data.jma.go.jp/svd/eqev/data/kyoshin/jishin/1604160125_kumamoto/index2.html (last accessed August 2016). The Numpy library can be accessed at <http://www.numpy.org/#> (last accessed August 2016), the OpenCV library can be accessed at <http://opencv.org/> (last accessed 2016) and the GDAL library can be accessed at <http://www.gdal.org/index.html> (last accessed August 2016).

Chapter 8

General conclusions

This research aimed to evaluate the accuracy of the ground displacement obtained either from accelerometer or GNSS stations. In order to achieve this objective, the high dense nationwide networks of Japan: K-NET, KiK-net and GEONET, and the Fukushima nuclear power plant's strong motion network were used. The important findings are presented as follows:

In chapter 3, It was observed that the ground velocity and displacement time history from a single and double integration of the acceleration recorded during the Tohoku earthquake have shown unphysical distortions produced by a shift in the baseline. We evaluate the techniques to reduce the effects of the baseline shifts in the ground velocity, ground displacement and response spectra of 10 ground-motion stations configured into two vertical arrays and located in the Fukushima Dainichi nuclear power plant. We observed a large variability in the final displacement. We also found that the pulse-like wave related to permanent ground displacement did not affect the interval of periods of the response spectra that is important in earthquake engineering. We observe also that records with high distortion in the time history records also show large distortion longer period components of the response spectra.

In chapter 4, the effect of baseline shift in acceleration records on the estimation of permanent displacements was evaluated. For this purpose, a large amount of strong-motion data recorded by KiK-net and K-NET during the M_w 9.0 Tohoku-Oki earthquake was used. Two automatic baseline correction methods proposed by Chao et al. (2010) and Wang et al. (2011) were selected to remove the effects of baseline shift and estimate the permanent displacement. The results were compared with a more accurate displacement obtained from the kriging interpolation of GEONET data. The results showed that the current baseline correction methods could not obtain reliable permanent displacements for acceleration records at the ground surface. In contrast, reasonable results were found for acceleration records at the bedrock: Wang's method yielded the best results with a standard deviation of 46 cm, 34 cm, and 30 cm for the EW, NS, and UD components, respectively. Such a difference between the results from records at the surface and bedrock was also observed by Hirai and Fukuwa (2012) and Wang et al. (2013). This is a disadvantage because most strong-motion accelerometers are located on the ground surface. In addition, high precision in amplitude and orientation has been observed in stations that develop large permanent displacements; the accuracy decreases as the permanent displacement reduces. This observation suggests that a minimum distance between the source and the strong-motion station can be used as a threshold to filter poor results.

In chapter 5, a method to remove the effects of the baseline shift was developed by employing a joint parameter search for each KiK-net station with surface and borehole accelerometers. Using this method, a remarkable improvement was observed in the results for the records at the surface. However, our method has a limitation in that it requires the use of two accelerometers (at the bedrock and surface) deployed at the same site. The results of the joint parameter search method show that the time parameters obtained using

previous methods can be improved and that the poor results at the surface are not mainly due to nonlinear baseline shifts.

In chapter 6, we studied the performance of Real-Time Kinematic (RTK) positioning for different baseline distances to assess coseismic deformation. For this purpose, the coseismic displacement recorded at one GNSS station during the November 22, 2014 Nagano earthquake was used. A total of 1,220 cases with BL lengths ranging from 20 km to approximately 2,000 km were evaluated. For each case, two setting processes were applied: the conventional RTK (CRTK), which is designed to achieve centimeter-level accuracy for BL lengths less than 20 km, and an RTK method designed for long baselines (LRTK).

Systematic errors appeared in the displacement time history for CRTK, resulting in a continuous and smooth change in the coordinates. The rate of those changes increases as the baseline increases. However, because the coseismic displacement occurs suddenly, it could be still observed in most cases. The systematic errors were almost removed when LRTK was used. Moreover, records with large distortions were still observed. These errors were attributed to factors other than the atmospheric effects.

For the studied case, the Nagano earthquake, the coseismic displacement estimated by the LRTK has errors less than 10 cm. However, the results from the CRTK have increasing errors as the baseline increases. These errors are less than approximately 20 cm for baselines less than 500 km and increase to one meter when the baseline reaches approximately 1,500 km. For the records with the shortest baseline, by comparing the blue lines of Figure 6.6 (the averaging window plus two times the standard deviation), CRTK achieves better results than LRTK. One reason for the better results is that the window averaging is affected by the large error caused by factors other than the baseline length; another reason is that for short baselines, using only double differentiation, more accurate atmospheric effects can be obtained than by estimating the atmospheric effects. The atmospheric effects can then be removed because the atmospheric conditions in both control stations (rover and master) are well-correlated when the baseline is short.

In chapter 7, The coseismic displacement produced during the mainshock of the 2016 M_w 7.1 Kumamoto earthquake using two DSMs collected by Lidar flights before and after the 16 April mainshock. The common area of the DSMs covers about 80 km² including the Mashiki town section of the known Futagawa fault line. The maximum cross-correlation was used with a window matching technique between the two DSMs to calculate the coseismic displacement. A coseismic displacement of up to 2 m and a subsidence of up to 2 m were observed in the study area. These values are the largest coseismic displacements produced in the Kumamoto earthquake, which were not able to record at any GEONET stations. The results showed good agreement with the permanent displacement calculated from strong-motion records and with the Futagawa fault line published by the Geological Survey Institute of Japan.

References

- Aoi, S., Kunugi, T., and Fujiwara, H. (2004). Strong-motion seismograph network operated by NIED: K-NET and KiK-net, *J. Japan Assoc. Earthq. Eng.* 4(3), 65-74.
- Bendat, J. S., and Piersol, A. G. (1986). Random data - analysis and measurement procedures, Second Edition, *John Wiley and Sons*, New York.
- Berg, G. V., and Housner, G. W. (1961). Integrated velocity and displacement of strong earthquake ground motion, *Bulleting of the Seismological Society of America* 51, No.2, 175-189.
- Boore D (2001). Effect of baseline corrections on displacement and response spectra for several recordings of the 1999 Chi-Chi, Taiwan, Earthquake, *Bulleting of the Seismological Society of America* 91, 1199-1211.
- Borre K, Stran G (2012). Algorithms for global positioning, *Wellesley-Cambridge*, USA.
- Branzanti, M., Colosimo, G., Crespi, M., and Mazzoni, A. (2013). GPS near-real time coseismic displacement for the Great Tohoku-oki earthquake, *IEEE Geoscience and Remote Sensing Letters* 10, 372-376.
- Chao W, Wu Y, Zhao L (2010). An automatic scheme for baseline correction of strong-motion records in coseismic deformation determination, *Journal of Seismology* 14, 495-504.
- Colosimo, G., Crespi, M., and Mazzoni, A. (2011). Real-time GPS seismology with a stand-alone receiver: A preliminar feasibility demonstration, *Journal of Geophysical Research* 116, B11302, 1-14.
- Duffy, B., Quigley, M., Barrel, D. J. A., Dissen, R. V., Stahl, T., Leprince, S., McInnes, C., and Bilderback, E. (2013). Fault kinematics and surface deformation across a releasing bend during the 2010 Mw 7.1 Darfield, New Zealand, earthquake revealed by differential LiDAR and cadastral surveying, *Geological Society of America Bulletin*, Vol 125, No. 3/4, 420-431.
- Furuma, T., Takemura, S., Noguchi, S., Takemoto, T., Maeda, T., Iwai, K., and Padhy, S. (2011). Strong ground motions from the 2011 off-the Pacific-Coast-of-tohoku, Japan (Mw=9.0) earthquake obtained from a dense nationwide seismic network, *Landslides* 8, 333-338.
- Ghofrani, H., and Atkinson, G. M. (2015). Duration of the 2011 Tohoku earthquake ground motions, *Journal of Seismology*, 19, 9-25.
- Graizer, V. M. (1979). Determination of the True Ground Displacement by Using Strong Motion Records, *Izv. USSR Acad. Sci., Physics Soild Earth* 15(12), 875-885.
- Graizer, V. M. (2005). Effect of tilt on strong motion data processing, *Soil Dynamics and Earthquake Engineering* 25, 197-204.

- Graizer, V. (2010). Strong motion Recordings and residual displacements: What are we actually recording in strong motion seismology?. *Seismological Research Letters* 81, No 4, 635-639.
- Hall, J. F., Heaton, T. H., Halling, M. W., and Wald, D. J. (1995). Near-source ground motion and its effects on flexible buildings, *Earthquake Spectra* 11, No. 4, 569-605.
- Hashimoto, M. (2013). Crustal deformation associated with the 2011 Tohoku-Oki earthquake: An overview, *Earthquake Spectra* 29, S81-S98.
- Hata Y, Murata A, Miyajima M (2015). Preliminary report on strong motion estimation at damage and non-damaged clusters in Kamashiro district, Hakuba Village during large earthquake ($M_{JMA}=6.7$) in northern Nagano Prefecture, centra Japan, *JSCE journal of Disaster FactSheets* FS2015-E-0001, 9 p.
- Hofmann-Wellenhof B, Lichtenegger H, Collins J (2001). GPS Theory and practice, *Springer-Verlag Wien, USA*, 5th edition.
- Housner, G. W., Trifunac, M. D. (1967). Analysis of accelerograms – Parkfield earthquake, *Bulleting of the Seismological Society of America* 57, No 6, 1193-1220.
- Imakiire T, Kobayashi T (2011). The crustal deformation and fault model of the 2011 off the Pacific Coast of Tohoku earthquake, *Bulleting of the Geospatial Information Authority of Japan* 59,21-33.
- Iwan W. D., Moser, M. A., and Peng, C. (1985). Some observations in strong-motion earthquake measurement using a digital accelerograph. *Bulleting of the Seismological Society of America* Vol 75, No 5, 1225-1246.
- Jaboyedoff, M., Oppikofer, T., Abellan, A., Derron, M., Loye, A., Metzger, R., and Pedrazzini, A. (2012). Use of LIDAR in landslide investigations: a review, *Nat. Hazards* 61: 5-28.
- Liao, W., Loh, C., and Lee, B. (2004). Comparison of dynamic response of isolated and non-isolated continuous girder bridges subjected to near-fault ground motions, *Engineering Structures* 26, 2173-2183.
- Lillesand, T. M., Kiefer, R. W., and Chipman J. W. (2014). *Remote sensing and image interpretation*, 5th ed. John Wiley and Sons, Inc.: United States.
- Liu W, Moya L, Yamazaki F (2015). Extraction of coseismic displacement in the November 22, 2014 Nagano, Japan earthquake from ALOS-2 images, *The 5th Asia-Pacific conference on synthetic aperture radar*, 845-848.
- Liu, W., Yamazaki, F., and Vu, T. T. (2011). Automated vehicle extraction and speed determination from QuickBir satellite images, *Journal of Selected Topics in Applied Earth Observations and Remote Sensing*, IEEE, Vol 4, No. 1, 75-82.
- Liu, W., Yamazaki, F., Gokon, H., and Koshimura, S. (2013a). Extraction of tsunami-flooded areas and damaged buildings in the 2011 Tohoku-Oki earthquake from Terra SAR-X intensity images, *Earthquake Spectra* 29, S183-S200.

- Liu W, Yamazaki F (2013b). Detection of crustal movement from TerraSAR-X intensity images for the 2011 Tohoku, Japan earthquake, *IEEE Geoscience and Remote Sensing Letters* 10 (1), 199-203.
- Liu W, Yamazaki F, Matsuoka T, Nonaka T, Sasagawa T (2015). Estimation of three-dimensional crustal movements in the 2011 Tohoku-Oki, Japan, earthquake from TerraSAR-X intensity images, *Natural Hazards and Earth System Sciences* 15, 637-645.
- Liu, Z., Owen, S., and Moore, A. (2014). Rapid estimated and modelling of permanent coseismic displacement for large earthquakes using high-rate global positioning system data, *Seismological Research Letters* 85, No. 2, 284-294.
- Mavroeidis, G. P., Dong, G., and Papageorgiou, A. S. (2004). Near-fault ground motions, and the response of elastic and inelastic single-degree-of-freedom (SDOF) systems, *Earthquake Engineering and Structural Dynamics* 33, 1023-1049.
- Melgar D, Bock Y (2013). Near-field models with rapid earthquake source inversions from land- and ocean-based observations: The potential for forecast and warning, *Journal of Geophysical Research: Solid Earth* 118, 1-17.
- Melgar, D., Crowell, B. W., Bock, Y., and Haase, J. S. (2013). Rapid modelling of the 2011 Mw 9.0 Tohoku-oki earthquake with seismogeodesy, *Geophysical Research Letters* 40, 1-6.
- Melgar D, Bock Y (2015). Kinematic earthquake source inversion and tsunami runup prediction with regional geophysical data, *Journal of Geophysical Research: Solid Earth* 120, 1-26.
- Moya L, Yamazaki F, Liu W (2016). Comparison of coseismic displacement obtained from GEONET and seismic networks, *Journal of Earthquake and Tsunami* 10, No.2, 18p.
- Muller, J. R., and Harding, D. J. (2007). Using LIDAR surface deformation mapping to constrain earthquake magnitudes on the Seattle fault in Washington state, USA, *Urban Remote Sensing Joint Event, IEEE*, 7 pages.
- Nissen, E., Krishnan, A. K., Arrowsmith, J. R., and Saripalli, S. (2012). Three-dimensional surface displacement and rotations from differencing pre- and post-earthquake LiDAR point clouds, *Geophysical Research Letters*, Vol 39, L12301, 6 pages.
- Niu, J., and Xu, C. (2014). Real-time assessment of the broadband coseismic deformation of the 2011 Tohoku-Oki earthquake using an adaptive Kalman filter, *Seismological Research Letters* 85, No. 4, 836-843.
- Ohta Y, Kobayashi T, Tsushima H, Miura S, Hino R, Takasu T, Fujimoto H, Iinuma T, Tachibana K, Demachi T, Sato T, Ohzono M, Umino N (2012). Quasi real-time fault model estimation for near-field tsunami forecasting based on RTK-GPS analysis: Application to the 2011 Tohoku-Oki earthquake (Mw 9.0), *Journal of Geophysical Research* 117, B02311, 16p.

- Oskin, M. E., Arrowsmith, J. R., Corona, A. H., Elliot, A. J., Fletcher, J. M., Fielding, E. J., Gold, P. O., Garcia, J. G., Hudnut, K. W., Liu-Zeng, J., and Teran, O. J. (2012). Near-field deformation from the El Mayor-Cucapah earthquake revealed by differential LIDAR. *Science*, Vol. 335 (6069), 702-705.
- Ozawa S, Nishimura T, Suito H, Kobayashi T, Tobita M, Imakiire T (2011). Coseismic and postseismic slip of the 2011 magnitude-9 Tohoku-Oki earthquake, *Nature* 475 (7356), 373-377.
- Ozbulut, O. E., and Hurlbauss, S. (2012). A comparative study on the seismic performance of superelastic-friction base isolators against near-field earthquakes, *Earthquake Spectra* 28, No. 3, 1147-1163.
- Sagiya T (2004). A decade of GEONET: 1994-2003 The continuous GPS observation in Japan and its impact on earthquake studies, *Earth Planets Space* 56, xxix-xli.
- Skarlatoudis, A. A., and Papazachos, C. B. (2012). Preliminary study of the strong ground motion of the Tohoku, Japan, earthquake of 11 March 2011: Assessing the influence of anelastic attenuation and rupture directivity. *Seismological Research Letters* 83, 119-129.
- Stewart, J. P., Midorikawa, S., Graves, R. W., Khodaverdi, K., Kishida, T., Miura, H., Bozorgnia, Y., Campbell, K. (2013). Implications of the Mw 9.0 Tohoku-Oki Earthquake for ground motion scaling with source, path, and site parameters, *Earthquake Spectra* 29, No. S1, S1-S21.
- Takasu T, Yasuda A (2010). Kalman-filter-based integer ambiguity resolution strategy for long-baseline RTK with ionospheric and tropospheric estimation, *23rd International Technical Meeting of the Satellite Division*, Inst. of Nav., Oreg., 21-24 Sept.
- Takewaki, I., Fujita K., and Yoshitomi, S. (2013). Uncertainties in long-period motion and its impact on building structural design: Case study of the 2011 Tohoku (Japan) earthquake. *Engineering Structures* 49, 119-134.
- Vu, T. T., Tokunaga, M., and Yamazaki, F. (2003). Wavelet-based extraction of building features from airborne laser scanner data, *Can. J. Remote Sensing*, Vol. 29, No 6, pp. 783-791.
- Vu, T. T., Yamazaki, F., and Matsuoka, M. (2009). Multi-scale solution for building extraction from LIDAR and image data, *International Journal of Applied Earth Observation and Geoinformation*, 11, 281-289.
- Wang R, Schurr B, Milkereit C, Shao Z, Jin (2011). An improved automatic scheme for empirical baseline correction of digital strong-motion records, *Bulleting of the Seismological Society of America* 101, 2029-2044.
- Wu Y, Wu C (2007). Approximate recovery of coseismic deformation from Taiwan strong-motion records, *Journal of Seismology* 11, 159-170.
- Yamagiwa A, Hatanaka Y, Yutsudo T, Miyahara B (2006). Real-time capability of GEONET system and its application to crust monitoring, *Bulleting of the Geographical Survey Institute* 53, 27-33.

APPENDICES

APPENDIX A

Response Spectra of Fukushima Daiichi Nuclear Power Plant's strong motion network

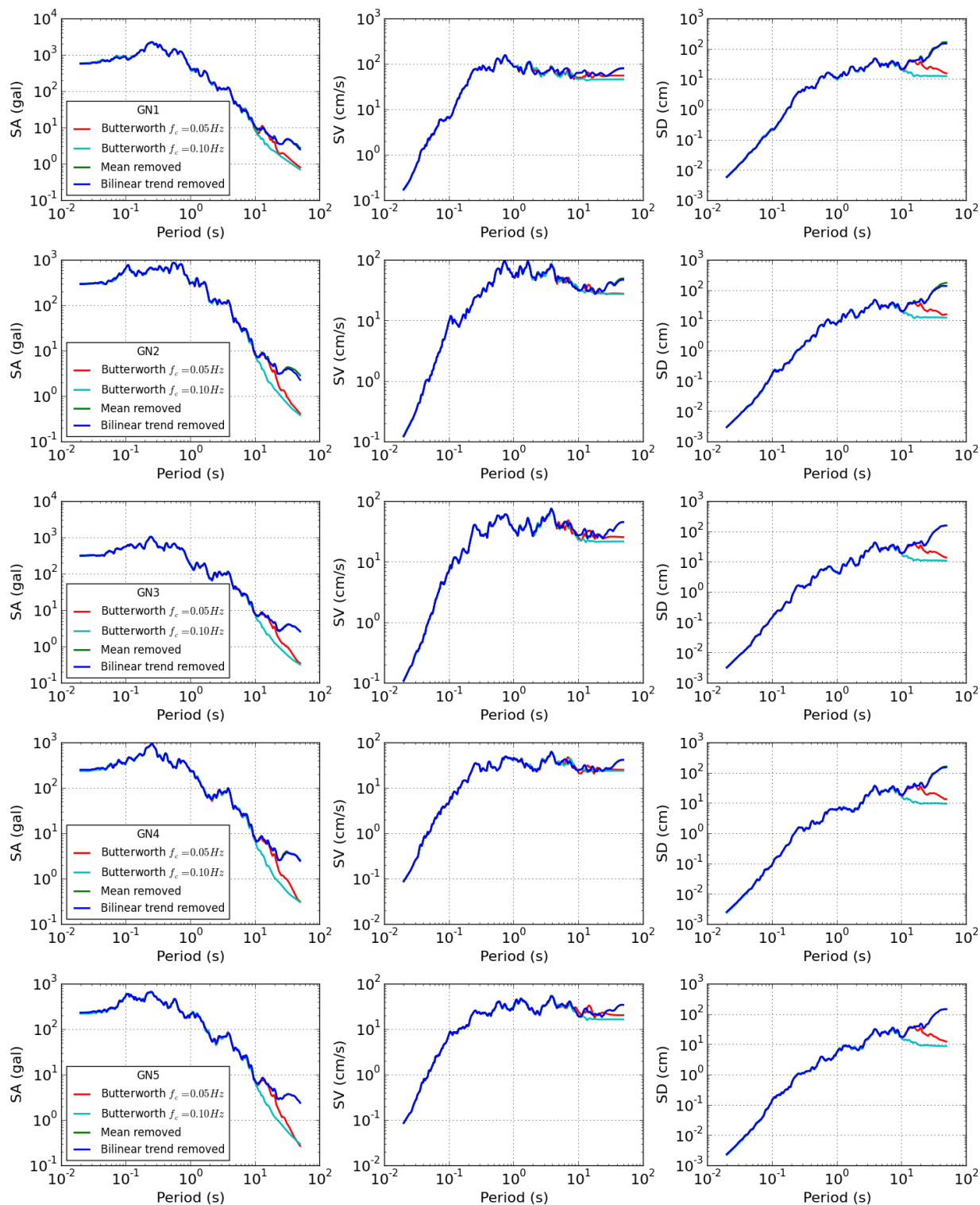


Figure A.1 Earthquake response spectra of the north-south component of the GN network; damping ratio, $\xi=0.05$; SA: spectral acceleration; SV: spectral velocity; SD: spectral displacement.

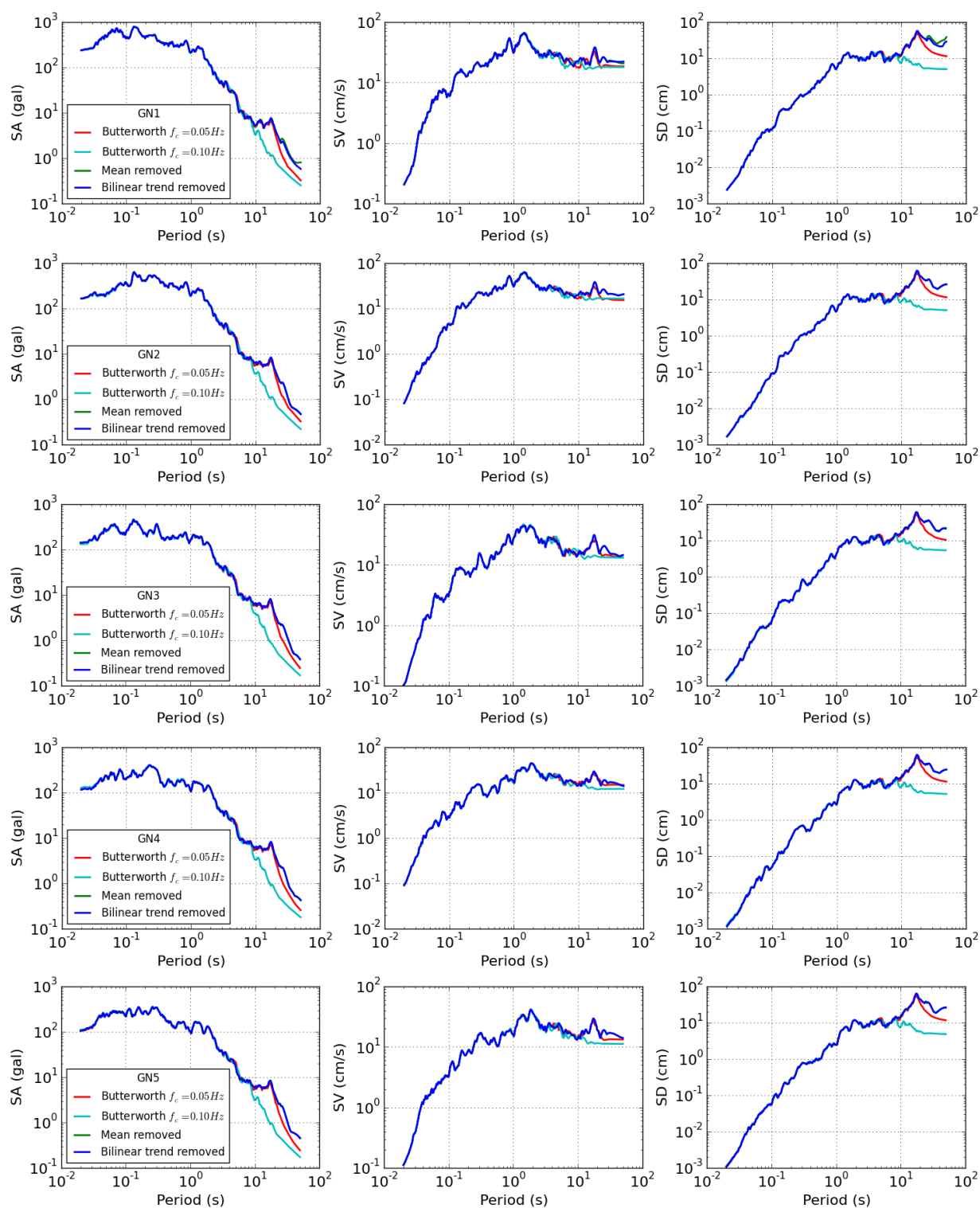


Figure A.2 Earthquake response spectra of the up-down component of the GN network; damping ratio, $\xi=0.05$; SA: spectral acceleration; SV: spectral velocity; SD: spectral displacement.

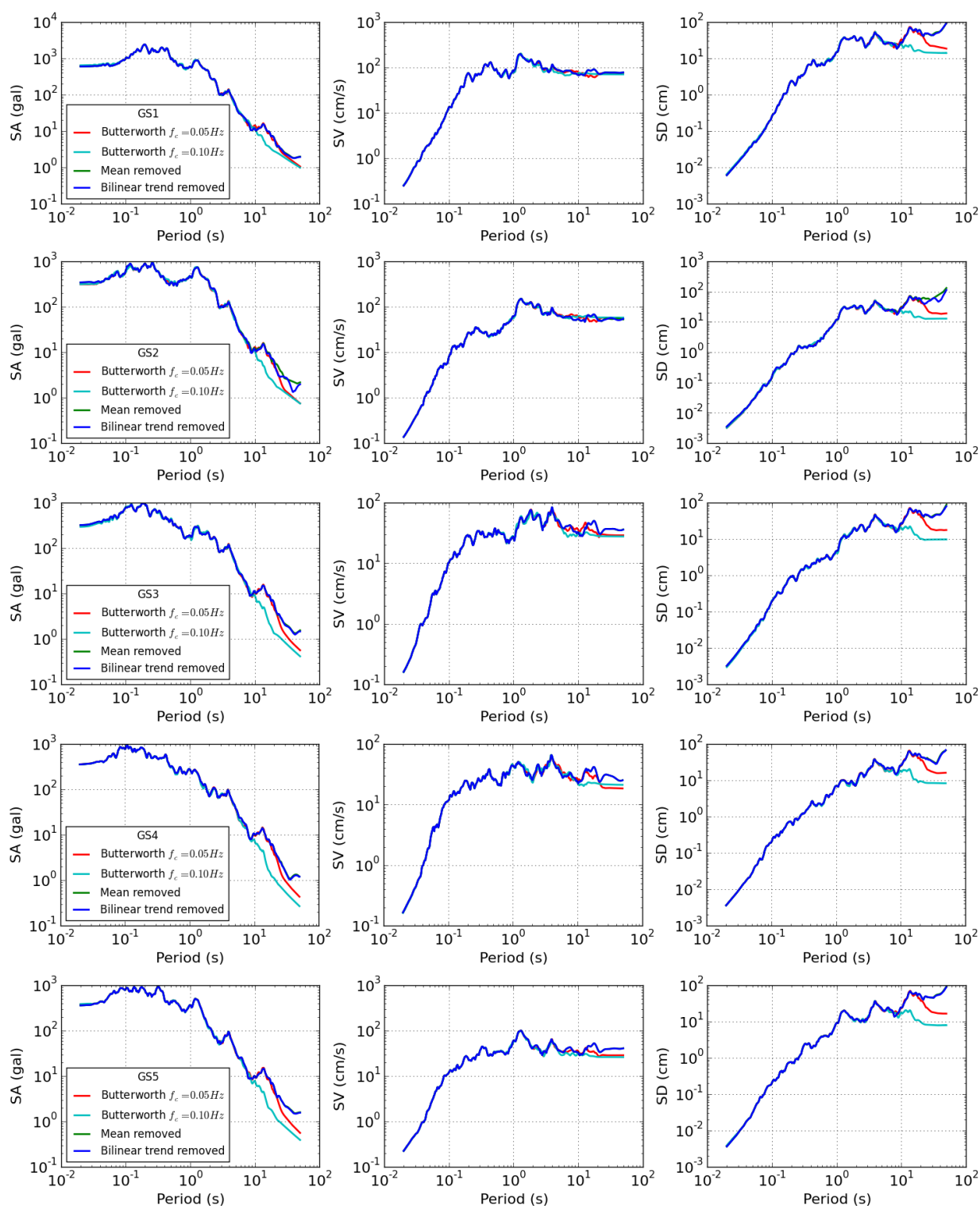


Figure A.3 Earthquake response spectra of the east-west component of the GS network; damping ratio, $\xi=0.05$; SA: spectral acceleration; SV: spectral velocity; SD: spectral displacement.

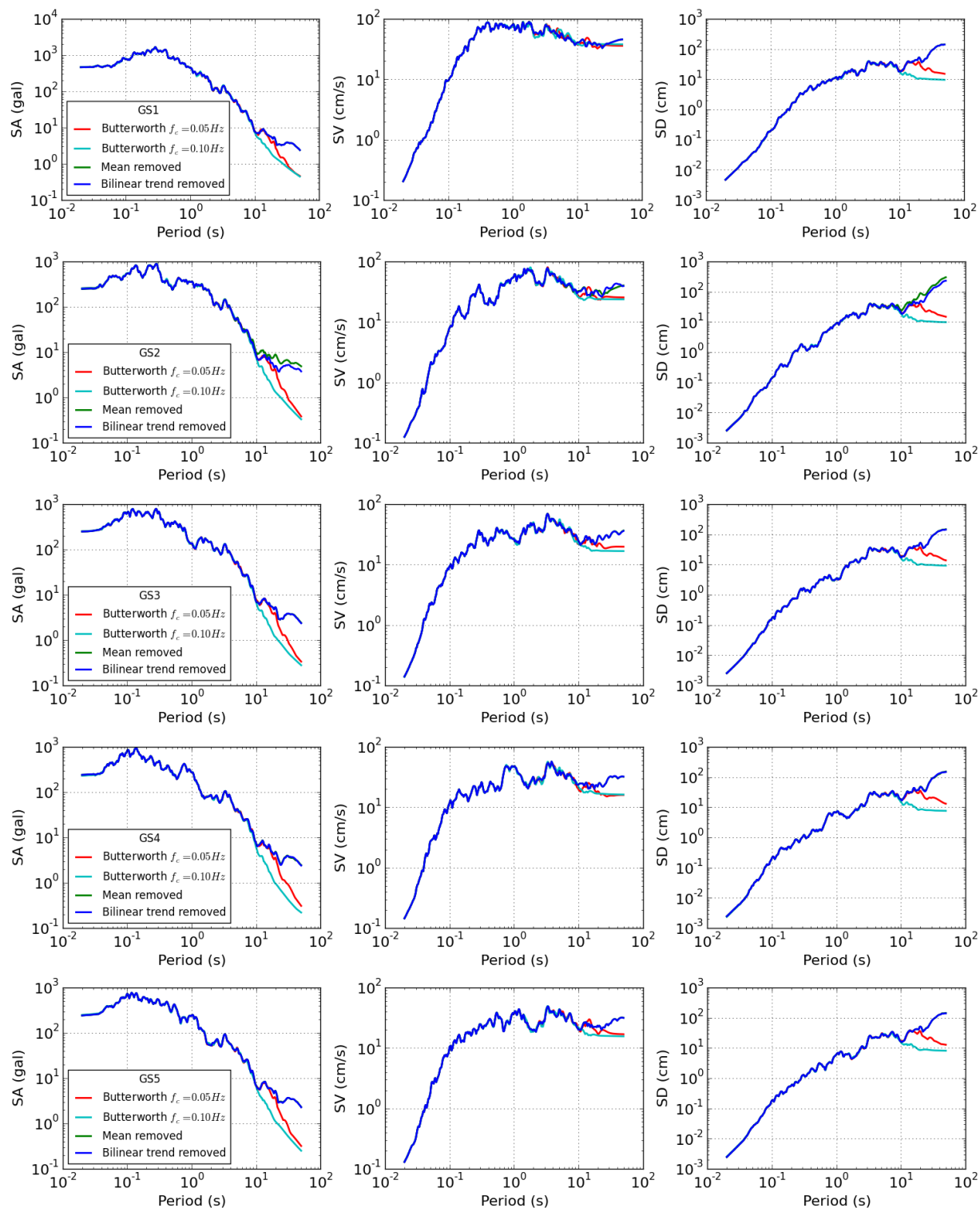


Figure A.4 Earthquake response spectra of the north-south component of the GS network; damping ratio, $\xi=0.05$; SA: spectral acceleration; SV: spectral velocity; SD: spectral displacement.

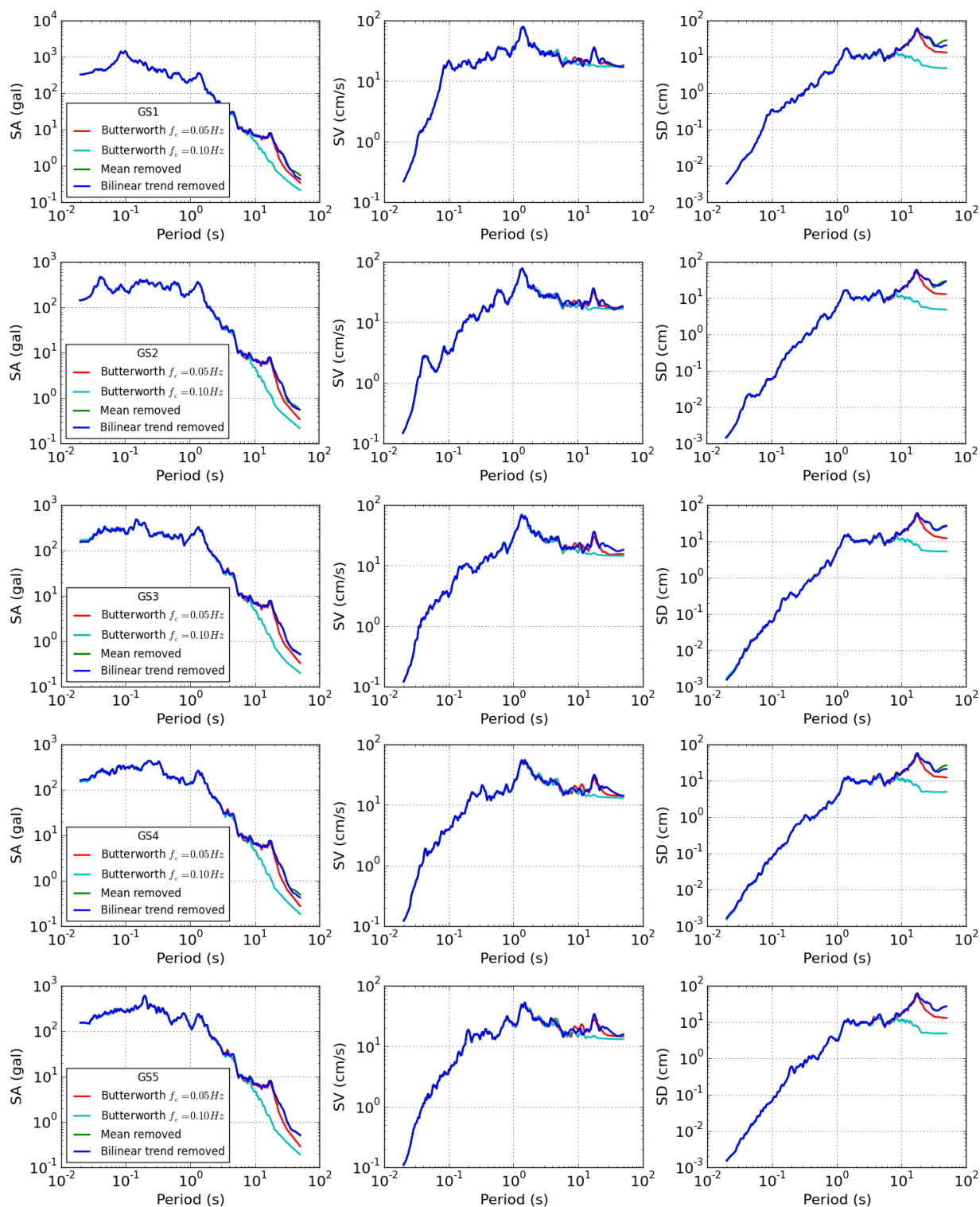


Figure A.5 Earthquake response spectra of the up-down component of the GS network; damping ratio, $\xi=0.05$; SA: spectral acceleration; SV: spectral velocity; SD: spectral displacement.

APPENDIX B

This section shows the python codes used to process acceleration records from KiK-net and K-NET

B.1 Python codes to process acceleration records

B.1.1 ReadingKiknetKnet

```
[1] def ReadingKiknetKnet(NameFile, time_aver = 10):
[2]     """ This function extract the acceleration record from file.
[3]     Namefile: name of the file that contain the record
[4]     time_aver: time interval of pre-event used to calculate the
[5]     average that will be removed from the acceleration record
[6]     """
[7]     infile1 = open(NameFile, 'r')
[8]     for i in range(10):
[9]         line = infile1.readline()
[10]        freq = infile1.readline().split()[2][:-2]
[11]        freq = float(freq)
[12]        for i in range(3):
[13]            line = infile1.readline()
[14]            temp = line.split()
[15]            NumScalFact1 = float(temp[2].split('(gal)')[0])
[16]            DenScalFact1 = float(temp[2].split('(gal)')[1])
[17]            for i in range(3):
[18]                line = infile1.readline()
[19]            Accel = []
[20]            while True:
[21]                line = infile1.readline()
[22]                if not line:
[23]                    break
[24]                line = line.split()
[25]                for n in range(len(line)):
[26]                    Accel.append(NumScalFact1*float(line[n])/DenScalFact1)
[27]            infile1.close()
[28]            Accel = np.asarray(Accel)
[29]            average = np.mean(Accel[:int(time_aver*freq)])
[30]            Accel = Accel - average*np.ones(len(Accel))
[31]            time = (1/freq) * np.arange(len(Accel))
[32]            return time, Accel, freq
```

B.1.2 FitLine

```
[1] def FitLine(x,y):
[2]     """ This function fits a line from the
[3]     record using the least squared method
```

```

[4] """
[5] A1 = np.dot(x,x)
[6] A2 = np.sum(x)
[7] A3 = len(x)
[8] B1 = np.dot(x,y)
[9] B2 = np.sum(y)
[10] a1 = (B1*A3 - B2*A2)/(A1*A3 - A2*A2)
[11] a2 = (A1*B2 - A2*B1)/(A1*A3 - A2*A2)
[12] x0 = -a2/a1
[13] return x0, a1, a2

```

B.1.3 Integration

```

[1] def Integration(Accel1, SampFreq1):
[2]     """ This function integrates twice to obtain the velocity and the displacement
[3]     INPUT
[4]     Accel1: acceleration record
[5]     SampFreq1: sampling frequency of the record
[6]     OUTPUT
[7]     Veloc1: velocity record
[8]     Displ1: displacement record
[9]     """
[10]    delta1 = 1 / SampFreq1
[11]    Veloc1 = np.zeros(len(Accel1))
[12]    Displ1 = np.zeros(len(Accel1))
[13]    for i in range(len(Accel1)-1):
[14]        Veloc1[i+1] = Veloc1[i] + 0.5*(Accel1[i] + Accel1[i+1])*delta1
[15]        Displ1[i+1] = Displ1[i] + Veloc1[i]*delta1 + (2*Accel1[i] + Accel1[i+1])*delta1**2 / 6
[16]    return Veloc1, Displ1

```

B.1.4 Displacement

```

[1] def Displacement(Accel1, Veloc1, SampFreq1):
[2]     """ This function calculates only the displacement. The reason is that some usually will be necessary to
[3]     correct the velocity and then recalculate the displacement
[4]     INPUT:
[5]     Accel1: acceleration record
[6]     Veloc1: velocity record
[7]     SampFreq1: sampling frequency
[8]     OUTPUT:
[9]     Displ1: displacement record
[10]    """
[11]    delta1 = 1 / SampFreq1
[12]    Displ1 = np.zeros(len(Accel1))
[13]    for i in range(len(Accel1)-1):

```

```
[14]     Displ1[i+1] = Displ1[i] + Veloc1[i]*delta1 + (2*Accel1[i] + Accel1[i+1])*delta1**2 / 6
[15]     return Displ1
```

B.1.5. Bilinear

```
[1] def Bilinear(Accel, Veloc1, time1, t1, t2, freq, portion = 100):
[2]     """ This function calculates the baseline correction using two
[3]     straight lines.
[4]     INPUT:
[5]     Accel: acceleration record
[6]     Veloc1: velocity record
[7]     time1: time record
[8]     t1, t2: time parameters
[9]     freq: sampling frequency
[10]    portion: last time interval used to fit a linear trend
[11]    OUTPUT:
[12]    accC: corrected acceleration
[13]    VelCorrected1: corrected velocity
[14]    disC: corrected displacement
[15]    baseLine1: baseline estimation of the velocity record
[16]    """
[17]    t02, a2, b2 = FitLine(time1[len(time1)-freq*portion :], Veloc1[len(time1)-freq*portion :])
[18]    y2 = a2*t2 + b2
[19]    a1 = y2/(t2 - t1)
[20]    b1 = -a1*t1
[21]    baseLine1 = np.zeros(len(Veloc1))
[22]    for n in range(int(t1*freq), len(Veloc1)):
[23]        if t1 < time1[n] <= t2:
[24]            baseLine1[n] = a1*time1[n] + b1
[25]        elif t2 < time1[n]:
[26]            baseLine1[n] = a2*time1[n] + b2
[27]    VelCorrected1 = Veloc1 - baseLine1
[28]    accC = np.zeros(len(Accel))
[29]    accC[: int(t1*freq)] = Accel[: int(t1*freq)]
[30]    accC[int(t1*freq): int(t2*freq)] = Accel[int(t1*freq): int(t2*freq)] - a1*np.ones(len(Accel[int(t1*freq): int(t2*freq)]))
[31]    accC[int(t2*freq) :] = Accel[int(t2*freq) :] - a2*np.ones(len(Accel[int(t2*freq) :]))
[32]    disC = Displacement(accC, VelCorrected1, freq)
[33]    return accC, VelCorrected1, disC, baseLine1
```

B.1.6 FlatnessIndicator

```
[1] def FlatnessIndicator(x,y):
[2]     """This function calculates the flatness parameter
[3]     used to define t2
[4]     INPUT:
[5]     x: last time interval used to calculate flatness
```

```

[6] y: last displacement interval used to calculate flatness
[7]
[8] """
[9] meanX = np.mean(x)
[10] meanY = np.mean(y)
[11] varianceX = np.var(x)
[12] varianceY = np.var(y)
[13] stdX = np.std(x)
[14] stdY = np.std(y)
[15] correlation = 0
[16] for n in range(len(x)):
[17]     correlation += ((x[n]-meanX)/stdX)*((y[n]-meanY)/stdY)
[18] correlation = correlation/len(x)
[19] x0, b, a2 = FitLine(x,y)
[20] flatness = np.absolute(correlation)/(np.absolute(b)*varianceY)
[21] return flatness

```

B.1.7 Wu_OriginalMethod

```

[1] def Wu_OriginalMethod(filePath, t1, t3, FunctAccel, ifPlot=False, details=False, outputPath="", sizeFontPlot = 25, cut=False):
[2]     """
[3]     This function calculates the baseline correction method proposed by Wu and wu (2007).
[4]     INPUT:
[5]     filePath: file location where the record is stored
[6]     t1, t3: time parameters used in Wu and Wu's method
[7]     FunctAccel: function used to extract acceleration from filePath
[8]     ifPlot: Optional; if ifPlot is True , then a plot of the result is created
[9]     details: Optional; if details is True, then a file with details of the method is created
[10]    outputPath: the path where the results are saved
[11]    sizeFontPlot: size of the font of the figure plot
[12]    cut: time location where the record is cutted
[13]    OUTPUT:
[14]    time: time array of the result
[15]    velC_b: corrected velocity
[16]    disC_b: corrected displacement
[17]    bl_b: baseline estimated of the velocity record
[18]    t1, t2_b: final time parameters
[19]    """
[20]    time, accel, freq = FunctAccel(filePath)
[21]    t1_50 = time[np.where(accel >= 50)[0][0]]
[22]    t1 = max(t1, t1_50)
[23]    if cut != False:

```

```

[24]     time = time[:int(freq*cut)]
[25]     accel = accel[:int(freq*cut)]
[26]     vel, disp = Integration(accel, freq)
[27]     accC_b, velC_b, disC_b, bl_b = Trilinear(accel, vel, time, t1, t3, freq, portion = 100)
[28]     flatness_b = FlatnessIndicator(time[t3*freq :], disC_b[t3*freq :])
[29]     t2_b = t3
[30]     for nt2 in range(int(freq*t3), len(time), int(0.5*freq)):
[31]         accC, velC, disC, bl = Trilinear(accel, vel, time, t1, time[nt2], freq, portion = 100)
[32]         flatness = FlatnessIndicator(time[t3*freq :], disC[t3*freq :])
[33]         if flatness > flatness_b:
[34]             accC_b = accC; velC_b = velC; disC_b = disC; bl_b = bl
[35]             flatness_b = flatness; t2_b = time[nt2]
[36]         print 't1 = %.2f; t2 = %.2f; final displacement = %.2f; flatness = %.4f' % (t1, time[nt2], disC[-1], flatness)
[37]     nameFile = os.path.split(filePath)[1]
[38]     if ifPlot:
[39]         ioff()
[40]         fig = figure(num=nameFile, figsize=(9,8))
[41]         subplot(2,1,1)
[42]         plot(time, velC_b)
[43]         ylabel('velocity (cm/s)', fontsize = sizeFontPlot)
[44]         xticks([]); rc('ytick', labelsz=sizeFontPlot)
[45]         title(nameFile+'\n', fontsize = sizeFontPlot)
[46]         subplot(2,1,2)
[47]         plot(time, disC_b)
[48]         ylabel('displacement (cm)', fontsize = sizeFontPlot)
[49]         xlabel('time (sec)', fontsize = sizeFontPlot)
[50]         rc('xtick', labelsz=sizeFontPlot); rc('ytick', labelsz=sizeFontPlot)
[51]         outputFig = os.path.join(outputPath, nameFile + '_WuOriginalMethod.jpg')
[52]         savefig(outputFig, bbox_inches='tight')
[53]         close(fig)
[54]     if details:
[55]         outputDetails = os.path.join(outputPath, nameFile + '_WuOriginalMethod.txt')
[56]         outfile1 = open(outputDetails, 'w')
[57]         outfile1.write('Record :,%s \n' % nameFile)
[58]         outfile1.write('-Final time parameters: t1= %.2f; t2= %.2f & t3= %.2f \n' % (t1,t2_b,t3))
[59]         outfile1.write('-Flatness indicator: f= %.5f \n' % flatness_b)
[60]         outfile1.write('-Final displacement: %f' % disC_b[-1])
[61]         outfile1.close()
[62]     # Printing results:
[63]     print '*****'
[64]     print 'Process finished:'

```

```

[65] print 'Record :,%s ' % nameFile
[66] print '-Final time parameters: t1= %.2f; t2= %.2f & t3= %.2f' % (t1,t2_b,t3)
[67] print '-Flatness indicator: f= %.5f' % flatness_b
[68] print '-Final displacement: %f' % disC_b[-1]
[69] print '*****'
[70] return time, velC_b, disC_b, bl_b, t1, t2_b

```

B.1.8 indexT1T3

```

[1] def indexT1T3(X):
[2]     """This function calculates the time parameters t1 and t3
[3]     based on the Chao's method.
[4]     INPUT:
[5]     X: acceleration record used to estimate the time parameters t1 and t3
[6]     OUTPUT:
[7]     n25: index where t1 is located
[8]     n65: index where t3 is located
[9]     """
[10]    energy = np.sum(np.square(X))
[11]    n65 = len(X)-1
[12]    energy25 = 0
[13]    energy65 = 0
[14]    while True:
[15]        energy65 += X[n65]**2
[16]        if energy65 > 0.35*energy:
[17]            break
[18]        else:
[19]            n65 -= 1
[20]    n25 = 0
[21]    while True:
[22]        energy25 += X[n25]**2
[23]        if energy25 > 0.25*energy:
[24]            break
[25]        else:
[26]            n25 += 1
[27]    return n25, n65

```

B.1.9 Wu_ChaoMethod

```

[1] def Wu_ChaoMethod(filePath, FunctAccel, ifPlot=False, details=False, outputPath="", sizeFontPlot = 25, cut=False):
[2]     """This function calculates the baseline correction method proposed by Chao et al (2010)
[3]     INPUT:
[4]     filePath: file location where the record is stored

```

```

[5]  FunctAccel: function used to extract acceleration from filePath
[6]  ifPlot: Optional; if ifPlot is True , then a plot of the result is created
[7]  details: Optional; if details is True, then a file with details of the method is created
[8]  outputPath: the path where the results are saved
[9]  sizeFontPlot: size of the font of the figure plot
[10] cut: time location where the record is cutted
[11] OUTPUT:
[12] time: time array of the result
[13] velC_b: corrected velocity
[14] disC_b: corrected displacement
[15] bl_b: baseline estimated of the velocity record
[16] t1, t2_b: final time parameters
[17] """"
[18] time, accel, freq = FunctAccel(filePath)
[19] if cut != False:
[20]     time = time[:int(freq*cut)]
[21]     accel = accel[:int(freq*cut)]
[22]     vel, disp = Integration(accel, freq)
[23]     nt1, nt3 = indexT1T3(accel)
[24]     t1 = time[nt1]; t3 = time[nt3]
[25]     accC_b, velC_b, disC_b, bl_b = Trilinear(accel, vel, time, t1, t3, freq, portion = 100)
[26]     flatness_b = FlatnessIndicator(time[t3*freq :], disC_b[t3*freq :])
[27]     t2_b = t3
[28]     for nt2 in range(nt3, len(time), int(0.5*freq)):
[29]         accC, velC, disC, bl = Trilinear(accel, vel, time, t1, time[nt2], freq, portion = 100)
[30]         flatness = FlatnessIndicator(time[t3*freq :], disC[t3*freq :])
[31]         if flatness > flatness_b:
[32]             accC_b = accC; velC_b = velC; disC_b = disC; bl_b = bl
[33]             flatness_b = flatness; t2_b = time[nt2]
[34]         print 't1 = %.2f; t2 = %.2f; final displacement = %.2f; flatness = %.4f' % (t1, time[nt2], disC[-1], flatness)
[35]     nameFile = os.path.split(filePath)[1]
[36]     if ifPlot:
[37]         ioff()
[38]         fig = figure(num=nameFile, figsize=(9,8))
[39]         subplot(2,1,1)
[40]         plot(time, velC_b)
[41]         ylabel('velocity (cm/sec)', fontsize = sizeFontPlot)
[42]         xticks([]); rc('ytick', labelsz=sizeFontPlot)
[43]         title(nameFile+'\n', fontsize = sizeFontPlot)
[44]         subplot(2,1,2)
[45]         plot(time, disC_b)
[46]         ylabel('displacement (cm)', fontsize = sizeFontPlot)
[47]         xlabel('time (sec)', fontsize = sizeFontPlot)
[48]         rc('xtick', labelsz=sizeFontPlot); rc('ytick', labelsz=sizeFontPlot)

```

```

[49]     outputFig = os.path.join(outputPath, nameFile + '_WuChaoMethod.jpg')
[50]     savefig(outputFig, bbox_inches='tight')
[51]     close(fig)
[52] if details:
[53]     outputDetails = os.path.join(outputPath, nameFile + '_WuChaoMethod.txt')
[54]     outfile1 = open(outputDetails, 'w')
[55]     outfile1.write('Record :,%s \n' % nameFile)
[56]     outfile1.write('-Final time parameters: t1= %.2f; t2= %.2f & t3= %.2f \n' % (t1,t2_b,t3))
[57]     outfile1.write('-Flatness indicator: f= %.5f \n' % flatness_b)
[58]     outfile1.write('-Final displacement: %f % disC_b[-1])
[59]     outfile1.close()
[60] # Printing results:
[61] print '*****'
[62] print 'Process finished:'
[63] print 'Record :,%s ' % nameFile
[64] print '-Final time parameters: t1= %.2f; t2= %.2f & t3= %.2f % (t1,t2_b,t3)
[65] print '-Flatness indicator: f= %.5f % flatness_b
[66] print '-Final displacement: %f % disC_b[-1]
[67] print '*****'
[68] return time, velC_b, disC_b, bl_b, t1, t2_b

```

B.1.10 Fitstep

```

[1] def FitStep(Displ):
[2]     """this function fits a step function to the displacement time history.
[3]     INPUT:
[4]     Displ: displacement record
[5]     OUTPUT:
[6]     n_min: location index of the step
[7]     Var_min: variance between the setp function and the displacement record
[8]     df: the magnitude of the step function
[9]     """
[10]    D_copy = Displ
[11]    var1 = np.square(D_copy)
[12]    var2 = np.square(D_copy - D_copy[-1] * np.ones(len(D_copy)))
[13]    Var = Var_min = np.sum(var2)
[14]    n_min = 0; df = D_copy[-1]
[15]    for n in range(len(D_copy)):
[16]        Var = Var - var2[n] + var1[n]
[17]        if Var < Var_min:
[18]            n_min = n
[19]            Var_min = Var
[20]    while True:
[21]        df = np.average(D_copy[n_min:])

```

```

[22] var2 = np.square(D_copy - df*np.ones(len(D_copy)))
[23] Var = Var_min2 = np.sum(var2)
[24] n_min2 = 0
[25] for n in range(len(D_copy)):
[26]     Var = Var - var2[n] + var1[n]
[27]     if Var < Var_min2:
[28]         n_min2 = n
[29]         Var_min2 = Var
[30] if absolute((Var_min-Var_min2)/Var_min) < 0.05:
[31]     return n_min, Var_min, df
[32] else:
[33]     Var_min = Var_min2
[34]     n_min = n_min2

```

B.1.11 Signalenergy

```

[1] def SignalEnergy(X):
[2]     """This function calculates the index location where the acceleration
[3]     energy reaches 90%.
[4]     INPUT:
[5]     X: acceleration record
[6]     OUTPUT:
[7]     n: location index of the 90% of acceleration energy
[8]     """
[9]     energy = np.sum(np.square(X))
[10]    n = len(X)-1
[11]    energy10 = 0
[12]    while True:
[13]        energy10 += X[n]**2
[14]        if energy10 > 0.10*energy:
[15]            break
[16]    else:
[17]        n -= 1
[18]    return n

```

B.1.12 FitQuadratic

```

[1] def FitQuadratic(x,y):
[2]     """This function fits a 2nd degree to the record using the least squared method.
[3]     INPUT:
[4]     x: time record used for the fitting
[5]     y: uncorrected velocity used for the fitting
[6]     OUTPUT:
[7]     coef[0], coef[1], coef[2]: coefficients of the 2nd degree polynomial
[8]     """

```

```

[9]  x0 = len(x)
[10] x1 = 0
[11] x2 = 0
[12] x3 = 0
[13] x4 = 0
[14] x2y1 = 0
[15] x1y1 = 0
[16] y1 = 0
[17] for n in range(len(x)):
[18]     x1 += x[n]
[19]     x2 += x[n]**2
[20]     x3 += x[n]**3
[21]     x4 += x[n]**4
[22]     x2y1 += x[n]**2*y[n]
[23]     x1y1 += x[n]*y[n]
[24]     y1 += y[n]
[25] X = np.array([[x4,x3,x2],[x3,x2,x1],[x2,x1,x0]])
[26] Y = np.array([x2y1, x1y1, y1])
[27] coef = np.linalg.solve(X, Y)
[28] return coef[0], coef[1], coef[2]

```

B.1.13 WangMethodFromArray

```

[1] def WangMethodFromArray(time, acce, freq):
[2]     '''
[3]     This function is an improved version of the function WangMethod (below this one). I decided tu use other
        functions created in the library 'JoiningMethodLibrary'.
[4]     Those functions are mostly base on numpy arrays. So, it will improve the velocity.
[5]     This function calculates the baseline correction method proposed by Wang (2011).
[6]     INPUT:
[7]     time: time record
[8]     acce: acceleration record
[9]     freq: sampling frequency
[10]    OUTPUT:
[11]    time: time record
[12]    disC_min: corrected displacement
[13]    velC_min: corrected velocity
[14]    bl_min: baseline shift of the uncorrected velocity
[15]    t1_min, t2_min: time parameters
[16]    '''
[17]    velo, disp = Integration(acce, freq)
[18]    Nois = max(np.absolute(acce[:int(10*freq)])) #Max level of noise before ground motion
[19]    note = ''
[20]    if max(np.absolute(acce)) < 5*Nois:
[21]        note = 'Max acceleration less than 5 x noise record'

```

```

[22]     return [],[],[],[],[],[]
[23] indTp = np.where(np.absolute(acce) > 5*Nois)[0][0]
[24] indPGA = np.where(np.absolute(acce) == max(np.absolute(acce)))[0][0]
[25] index90 = SignalEnergy(acce)
[26] if time[-1] > 4*time[index90] - 3*time[indTp]:
[27]     note = 'record cutted '
[28]     indCut = 4*index90 - 3*indTp
[29]     acce = acce[:indCut]
[30]     time = time[:indCut]
[31]     velo = velo[:indCut]
[32]     disp = disp[:indCut]
[33]     index90 = SignalEnergy(acce)
[34] indD0 = len(disp)-1
[35] while True:
[36]     if disp[indD0]*disp[indD0-1] < 0:
[37]         indD0 -= 1
[38]         break
[39]     elif indD0 == 1:
[40]         indD0 = 100
[41]         break
[42]     indD0 -= 1
[43] indPGD = np.where(np.absolute(disp) == max(np.absolute(disp[:indD0])))[0][0]
[44] half_ap, bp, c = FitQuadratic(time[index90:],disp[index90:])
[45] t2_min = time[max(indPGA,indD0)]; t1_min = time[indPGD]
[46]
[47] am = (2*half_ap*t2_min + bp)/(t2_min - t1_min)
[48] bm = -am*t1_min
[49] disC_min = jps.corDis(disp, time, t1_min, t2_min, am, bm, 2*half_ap, bp)
[50] nSF_min, Var_min, df_min = FitStep(disC_min)
[51] t2a = max(indPGA,indD0); t2b = index90+1
[52] if t2a > t2b:
[53]     t2a, t2b = t2b, t2a
[54] for it2 in range(t2a, t2b, int(1.0*freq)):
[55]     t2 = time[it2]
[56]     print t2
[57] for it1 in range(indPGD, it2, int(1.0*freq)):
[58]     t1 = time[it1]
[59]     am = (2*half_ap*t2 + bp)/(t2 - t1)
[60]     bm = -am*t1
[61]     disC = jps.corDis(disp, time, t1, t2, am, bm, 2*half_ap, bp)
[62]     n_SF, Var, df = FitStep(disC)
[63]     if Var < Var_min:
[64]         t2_min, t1_min = t2, t1
[65]         disC_min = disC

```

```
[66]     Var_min = Var
[67] t1Temp = t1_min; t2Temp = t2_min
[68] print 'refining windowing'
[69] for it2 in xrange(int((t2Temp-1)*freq), int((t2Temp+1)*freq), int(0.5*freq)):
[70]     print t2
[71]     if it2 >= len(time):
[72]         break
[73]     t2 = time[it2]
[74]     for it1 in xrange(int((t1Temp-4)*freq),int((t1Temp+4)*freq), int(0.5*freq)):
[75]         if it1 >= it2:
[76]             break
[77]         if it1 >= len(time):
[78]             break
[79]         t1 = time[it1]
[80]         am = (2*half_ap*t2 + bp)/(t2 - t1)
[81]         bm = -am*t1
[82]         disC = jps.corDis(disp, time, t1, t2, am, bm, 2*half_ap, bp)
[83]         n_SF, Var, df = FitStep(disC)
[84]         if Var < Var_min:
[85]             t2_min, t1_min = t2, t1
[86]             disC_min = disC
[87]             Var_min = Var
[88] velC_min, bl_min, a1 = Baseline_Wang(velo, time, freq, t1_min, t2_min, 2*half_ap, bp)
[89] return time, disC_min, velC_min, bl_min, t1_min, t2_min
```